Lung epithelial specific depletion of Numb and Numblike impairs epithelial polarity and integrity

Inaugural-Dissertation

zur Erlangung des akademischen Grades

doctor rerum naturalium

- Dr. rer. nat. -

Vom Fachbereich für Biologie (FB10) der

Technischen Universität Darmstadt genehmigte Dissertation

TECHNISCHE
UNIVERSITÄT
DARMSTADT

eingereicht von

Michael Hofmann (Dipl.-Biol.)

aus

Ludwigshafen am Rhein

Darmstadt, 2017

D17

Die vorliegende Arbeit wurde am
Max-Planck-Institut für Herz- und Lungenforschung (W. G. Kerckhoff Institut)
in Bad Nauheim angefertigt

Dekanin:	Prof. Dr. Beatrix Süß Fachbereich für Biologie (FB10) Technische Universität Darmstadt (TUD) Schnittspahnstraße 10 64287 Darmstadt
1. Referent (intern):	Prof. Dr. Ralf Galuske Fachbereich für Biologie (FB10) Technische Universität Darmstadt (TUD) Schnittspahnstraße 10 64287 Darmstadt
2. Referent (intern):	Prof. Dr. Paul G. Layer Fachbereich für Biologie (FB10) Technische Universität Darmstadt (TUD) Schnittspahnstraße 10 64287 Darmstadt
3. Referent (extern):	Prof. Dr. Thomas Braun Abteilung für Entwicklung und Umbau des Herzens Max-Planck-Institut für Herz- und Lungenforschung Ludwigstrasse 43 61231 Bad Nauheim
Tag der Einreichung:	11.05.2017
Tag der mündlichen Prüfung:	12.07.2017

Ehrenwörtliche Erklärung:

Ich erkläre hiermit ehrenwörtlich, dass ich die vorliegende Arbeit entsprechend den Regeln guter wissenschaftlicher Praxis selbstständig und ohne unzulässige Hilfe Dritter angefertigt habe.

Sämtliche aus fremden Quellen direkt oder indirekt übernommenen Gedanken sowie sämtliche von Anderen direkt oder indirekt übernommenen Daten, Techniken und Materialien sind als solche kenntlich gemacht. Die Arbeit wurde bisher bei keiner anderen Hochschule zu Prüfungszwecken eingereicht.

Darmstadt, den …… 11.05.2017

.....

Michael Hofmann

I. TABLE OF CONTENTS

II. ABBREVIATIONS

α	-	alpha
α–	-	anti-
aa	-	amino acids
AJ	-	adherens junction
ATI	-	Alveolar type I cell
ATII	-	Alveolar type II cell
BAL	-	bronchio-alveo-lavage
bleo	-	bleomycin
Co-IP	-	co-immunoprecipitation
Ctrl	-	control
dKD	-	*Numb*/*Numblike* double knock down
dKO	-	double knockout
DNA	-	deoxyribonucleic acid
Dox	-	doxycycline
e.g.	-	*exempli gratia*
EMT	-	epithelial to mesenchymal transition
FACS	-	fluorescence-activated cell sorting
FC	-	fold change
Fig	-	figure
GFP	-	green fluorescent protein
GFP	-	green fluorescent protein
hpf	-	high power field
i.e.	-	*id est*
IF	-	Immunofluorescence
IHC	-	Immunohistochemistry
IP	-	immunoprecipitation
MDCKII	-	Mardin-Darby canine kidney II cells
MLE12	-	mouse lung epithelial cell line
MS	-	Mass spectrometry
Nb	-	Numb
NbL	-	Numblike
NSCLC	-	non-small-cell lung carcinoma
PRR	-	proline-rich region
PTB	-	phospho-tyrosine-binding domain
RNA	-	ribonucleic acid
RT	-	room temperature
rtTA	-	reverse tetracycline-dependent transactivator
shRNA	-	small hairpin RNA
ß	-	beta
STAGE	-	Stop and go extraction
Tet	-	tetracycline

TJ	-	tight junction
TRE	-	transcriptional response element
VP16	-	virion protein 16
vs.	-	*versus*
WB	-	Western Blot
WT	-	will type
WtCtrl	-	wild type control
YFP	-	yellow fluorescent protein

III. ZUSAMMENFASSUNG

Numb ist ein membrangebundenes Adapterprotein, welches Ähnlichkeiten zu seinem cytoplasmatischen Homolog Numblike aufweist. Beide Gene spielen beispielsweise eine große Rolle in Gehirn- oder auch Herzentwicklung. Auf molekularer Ebene ist Numb in verschiedenste Prozessen involviert, wie z.B. bei Endocytose, Proteasom regulierter Proteindegradierung oder auch der Inhibition des Notch Signalwegs. Des weiteren spielt Numb auch eine wichtige Rolle bei der Etablierung von Zell-Zell Kontakten, sowie epithelialer Polarität. In dieser Studie sollte untersucht werden, ob ein Fehlen von Numb und Numlike im Lungenepithel dessen Integrität oder auch dessen Regenerationsfähigkeit beeinflusst. Hierzu wurde *Numb* konditionell und lungenepithelspezifisch in Mäusen mit Numblike ablatiertem Hintergrund genetisch inaktiviert. Dabei wurde ein durch Doxycyclin induzierbares Inaktivierungssystem (SPCrtTA-tet-O-Cre) benutzt, welches die funktionelle Charakterisierung von Numb und Numblike im Lungenepithel ermöglicht. Tiere, die einen Verlust der Genaktivität von Numb und Numblike im Epithel zeigen, sind lebensfähig und offenbaren lediglich schwache morphologische Veränderungen epithelialer Zellen. Diese Zellen weisen eine veränderte Lokalisation der Adhärenzkontaktproteine E-Cadherin und ß-Catenin in der Zellmembran auf. Zudem ist in den Doppelmutanten eine deutliche Reduktion von Alveolaren Zellen des Typs II zu verzeichnen. Diese Veränderungen deuten auf eine wichtige Funktionen von Numb und Numblike in der Erhaltung von epithelialer Integrität sowie Polarität hin. Erstaunlicherweise zeigen doppelmutante Tiere eine merklich schwächer ausgeprägte Fibrose nach Behandlung mit Bleomycin. Die Tiere weisen eine höhere Überlebensrate auf und zeigen auch sonst verbesserte Werte auf molekularer und histologischer Ebene. Besonders auffällig hierbei sind Veränderungen des Wnt/ß-Catenin Signalwegs als möglicher Effekt der *Numb*/*Numblike* Inaktivierung. Der Fibroseverlauf könnte hierdurch maßgeblich beeinflusst und abschwächt sein. Durch die Inaktivierung von Numb und Numblike in der lungenepithelailen Zelllinie MLE12 erlangte ich einen tieferen Einblick in veränderte molekulare Prozesse und konnte ebenso bereits *in vivo* ermittelte Ergebisse, wie E-Cadherin/ß-Catenin Lokalisierung sowie beeinträchtigte Expression von Wnt-Zielgenen reproduzieren und validieren. Expression von ß-Catenin, ebenso wie die seiner Zielgene, konnte hier mittels GSK-3ß Inhibition verbessert werden, was weiterhin eine Beeinträchtigung von Wnt/ß-Catenin Signalen in *Numb*/*Numblike*

defizienten Epithelzellen unterstreicht. Schließlich konnten mit Hilfe von massenspektrometrischer Analyse die Kinase CK2 sowie Cortactin, ein F-Aktin bindendes Protein, als neue Interaktionspartner von Numb und Numblike identifiziert werden. Diese könnten das Mitwirken von Numb in der Ausbildung von Zell-Zell Kontakten, sowie deren Stabilisierung, unterstützt durch cytoplasmatisches Numblike, erklären.

IV. ABSTRACT

Previously it was shown that the membrane associated adaptor protein Numb and its cytosolic mammalian homolog Numblike (Numbl) exert redundant functions during neurogenesis and heart development [1-3]. Numb is involved in multiple processes such as endosomal trafficking, proteosomal degradation as well as the inhibition of Notch signaling [4-9]. Furthermore, Numb is reported to mediate epithelial polarity as well as cell-cell adhesion [10]. In this work I want to examine if loss of *Numb* and *Numblike* has an impact on lung epithelial integrity and its regenerative capacities upon lung damage. Therefore, I have generated conditional knockout animals for *Numb* on a *Numblike* deficient background using the doxycycline inducible *SPCrtTA-tet-O-Cre* system, which enables to analyze functions of Numb during pulmonary development and regenerative processes after damage of the distal lung epithelium. While $SPCrtTA^{pos}$//$tetO\text{-}Cre^{pos}$//$Numb^{fl/fl}$//$Numblike^{-/-}$ mutants (dKO) are viable they exhibit a complete loss of *Numb* in proximal and distal lung epithelium. Concomitant lung epithelial ablation of *Numb and Numblike* causes only mild morphological changes of epithelial cells accompanied by a basal-to-apicolateral translocation of E-Cadherin as well as a mislocalization of ß-Catenin. In addition, adult dKOs show a significant decrease in SPC^{+} Alveolar Type II cell numbers compared to littermate control animals (Ctrl). These changes suggest a potential function of Numb/Numblike in mediating lung epithelial polarity and integrity. Interestingly, in experimental pulmonary fibrosis *Numb/Numblike* deficient mice show better survival and a significant milder fibrotic damage on molecular and histological levels. I revealed impaired WNT signaling as a potential secondary effect of *Numb/Numblike* depletion, which might ameliorate disease progression. To further investigate the underlying molecular processes, I took advantage of *shNumb/shNumblike* MLE12 knockdown cells, which show mislocalization of E-Cadherin, decreased ß-Catenin levels and reduced Wnt target gene expression similar to the *in vivo* state. *In vitro* rescue of ß-Catenin protein levels and relative expression of Wnt targets by GSK-3ß inhibition support an involvement of WNT/ß-Catenin signaling. Moreover, I identified Cortactin and CK2 as a novel interaction partners of Numb and Numblike mediating cell junctional stability in epithelial cells.

1 INTRODUCTION

1.1 The respiratory system

The mammalian respiratory system mainly consists of the trachea, the lung and the vasculature system that pervades throughout the entire lung. It is a highly important organ system that serves as a gateway to the oxygen-enriched atmosphere. Hence, the main function of this complex and specialized respiratory unit lies in the maintenance of a proper gas exchange of oxygen and carbon dioxide between the atmosphere and the blood circulation system, which is a fundamental requirement for survival in a terrestrial environment. The blood circulation system takes over an important role within this process of gas exchange that basically takes place at the boundary of respiratory surface and the thin-walled capillary vessels of the lung. It supplies all organs and tissues in the body with oxygen that gets absorbed at this boundary where it simultaneously releases the carbon dioxide produced by these tissues. Although the basic function of this ventilation system works out the same way in all mammals, there are slight differences between the structural setup of human and rodent lungs. Macroscopically, the human lung is subdivided into two left and three right lobes, while the mouse lung is organized in one left and 4 smaller right lobes, the cranial, medial, caudal and the accessory lobe. Furthermore, there are also slight differences in the composition of the different cell types that sit along the proximo-distal axis of the respiratory epithelium, which will be highlighted more detailed in section 1.1.2 (also see Table 1). In general both respiratory systems can be functionally grouped into conducting and respiratory tract. The conducting tract, which anatomically comprises nose, nasal cavity, pharynx, larynx, trachea, bronchi and bronchioles, serves as a tube system that permits entry and release of gas, removes intruding particles as well as pathogens and also warms and humidifies the inhaled air. Further, while in humans the branching pattern of the conducting airways proceeds symmetrically (dichotomous), mice in contrast exhibit an asymmetrical (monopodial) branching of the conducting tract. The respiratory tract is significantly involved in gas exchange and anatomically represented by alveolar sacs at the most distal areas in mouse lung. The respiratory compartment of human lungs is comprised by the acinus, which consists of alveolar sacs that are supplied via alveolar ducts by the respiratory bronchioles. Respiratory bronchioles are almost not found or very rare in mice as their

terminal bronchioles directly branch into respiratory units given by the alveoli [11]. The table below compares prominent structural differences of both murine and human respiratory systems.

	Feature	Mouse	Human
Gross	Lung lobes	4 right, 1 left	3 right, 2 left
	Airway generations	13 – 17	17 – 21
	Airway branching pattern	Monopodial	Dichotomous
	Diameter, main bronchus (mm)	1	10 – 15
Tissue	Diameter, terminal bronchiole (mm)	0.01	0.6
	Respiratory bronchioles	None or one	Yes
	Lung parenchyma/ total lung volume (%)	18	12
	Alveoli (µm)	39 – 80	200 – 400
	Blood-gas barrier thickness (µm)	0.32	0.62
Airway epithelial cells	Tracheal epithelium		
	- Epithelial thickness (µm)	11 – 14	50 – 100
	- Ciliated cells (%)	39	49
	- Clara cells (%)	49	-
	- Mucous goblet cells (%)	<1	9
	- Serous cells (%)	<1	<1
	- Basal cells (%)	10	33
	- Other (%)	1	-
	Proximal intrapulmonary epithelium		
	- Epithelial thickness (µm)	8 – 17	40 – 50
	- Ciliated cells (%)	28 – 36	37
	- Clara cells (%)	59 – 61	-
	- Mucous goblet cells (%)	<1	10
	- Serous cells (%)	<1	3
	- Basal cells (%)	<1	32
	- Other (%)	2 – 14	18
	Terminal bronchioles		
	- Epithelial thickness (µm)	7 – 8	Not determined
	- Ciliated cells (%)	20 – 40	52
	- Clara cells (%)	60 – 80	-
	- Mucous goblet cells (%)	0	-
	- Serous cells (%)	0	35
	- Basal cells (%)	<1	<1
	- Other (%)	0	13

Table 1: Murine and human respiratory systems in comparison.
Source: Adapted and modified from Treuting, P. M., et al. (2012) [11] as well as Fox (2007) and Plopper and Hyde (2008).

1.1.1 Murine lung development

The morphogenesis of mouse lung proceeds in 5 different stages (Figure 1A), which are very similar to those in humans. Solely the time courses of these developmental stages differ, as they are more extended in human lung organogenesis. Murine lung development starts with the budding of a primitive lung tube derived from the anterior foregut endoderm at embryonic day E9.0. The whole developmental process is characterized and driven by the onset of a spatial and temporal expression cascade

involving different transcription factors and signaling molecules (also depicted in Figure 1).

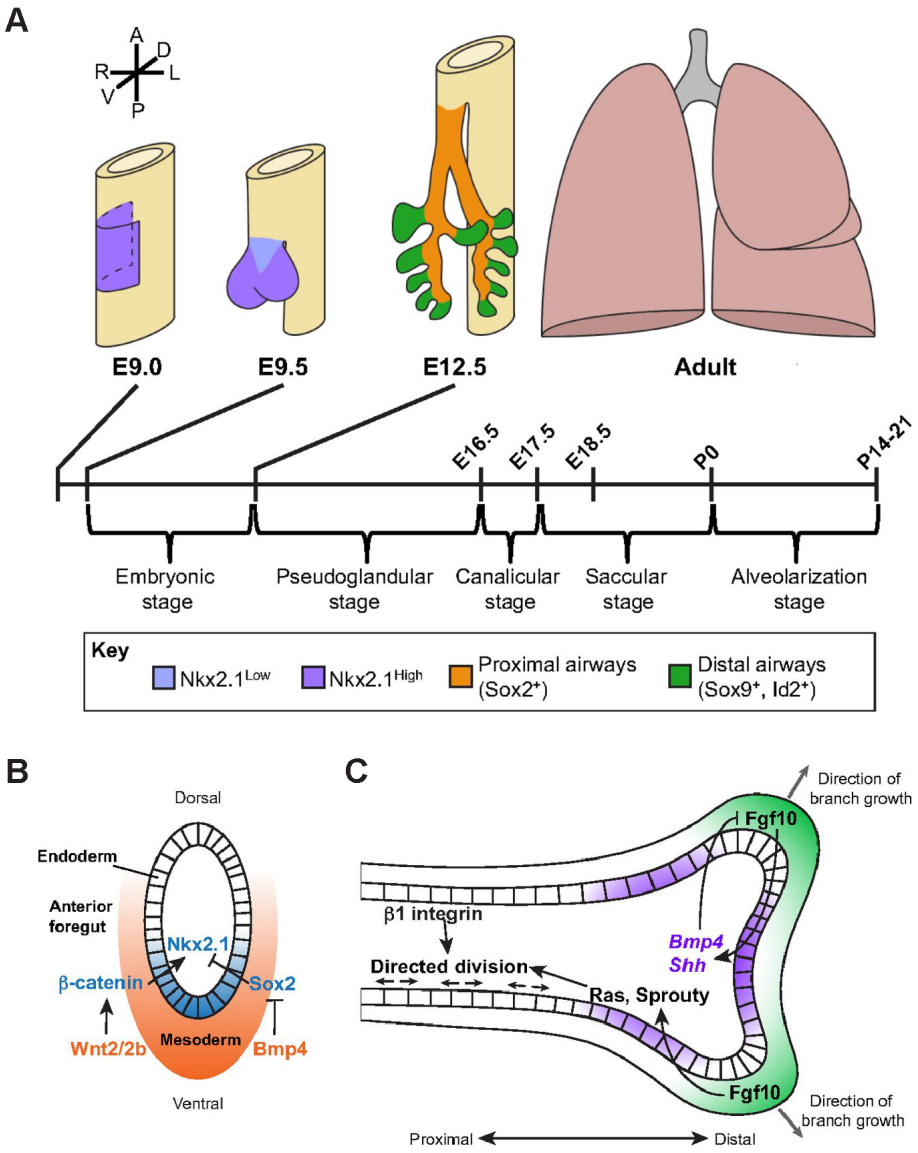

Figure 1: Murine lung development.
A: Schematic overview of the 5 stages of murine lung development including spatial expression of the prominently involved signaling molecules like Nkx2.1 (blue, purple), Sox2 (orange), Sox9 and Id2 (green), see also legend. B: Signaling interactions of ventral anterior mesoderm and anterior foregut entoderm. Nkx2.1 expression in epithelial progenitor cells arising from anterior forgut endoderm (blue) regulated by Wnt/ß-Catenin and Bmp4 signaling from the mesoderm (orange). Wnt2/2b and ß-Catenin signaling positively influence Nkx2.1 expression while Bmp4 signaling represses Nkx2.1 inhibition by Sox2. C: Regulation of proximal to distal branching morphogenesis by gradients of distal mesenchymal Fgf10 expression (green) which gets restricted by epithelial Shh and Bmp4 signals (purple). Outgrowth direction of branching points is further determined by regulation of epithelial Ras/Sprouty expression (purple) via Fgf10. Together with epithelial ß1-Integrin expression, which promotes epithelial cell polarity, Ras/Sprouty direct the orientation of epithelial cell divisions at the branching points. Figures adapted and modified from Herriges, M. and Morrisey, E. E. (2014) [12].

Nkx2.1 is one of the first transcription factors that are expressed in the early lung bud at day E9.0. Wnt/ß-Catenin signaling promoted by *Wnt2/2b* expression derived from the anterior foregut endoderm surrounding ventral anterior mesoderm positively influences *Nkx2.1* expression in the resident epithelial progenitors together with *Bmp4* signaling, which represses the *Sox2* mediated *Nkx2.1* inhibition [13, 14] (Figure 1B). During this first stage of lung development, the embryonic stage (E9.5 – E12.5), these *Nkx2.1* expressing epithelial progenitor cells evaginate ventraly from the foregut endoderm, to form a tube, which will later give rise to the trachea. At the distal end of this primordial tube the epithelial progenitor cells form two lung buds. Lung epithelial specification continues from these buds during the pseudoglandular stage (E12.5 – E16.5), which is characterized by complex branching morphogenesis. During this branching process both lung buds sprout and expand in a proximo-distal manner into the surrounding mesenchyme, forming a tree-like structure with terminal branches. Hence, this branching is essential for the later specification of proximal conducting airways and the distal respiratory tract. Another transcription factor that plays an important role in defining the specific branching points of the outgrowing terminal branches is *Fgf10* [15]. *Fgf10* is expressed by mesenchymal lung tissue that surrounds the distal tips of the developing airways. It has been suggested that this expression is regulated and restricted by epithelial endoderm derived Bmp4 and Shh signaling [16-18]. Furthermore, epithelial *Ras/Sprouty* expression, which is regulated by Fgf10 at branching points, directs the orientation of epithelial cell divisions at these sites [19]. This is supported by epithelial ß1-Integrin expression, which mediates epithelial cell polarity and prevents a multilayered development of the epithelium [20]. These signaling interactions between the primitive lung epithelium and the mesenchyme are necessary for a further directed branching proceeding during the canalicular stage (E16.5 – E17.5) and the following saccular stage (E17.5 – P0). These stages are mainly characterized by further specification of the proximal airway tube system, prolongation and narrowing of the terminal branches, the arrangement of the distal respiratory compartments in epithelial sacs and also vascularization in the lung mesenchyme. Finally, lung development ends with the specification of the distal epithelial sacs during the stage of alveolarization (P0 – P21). Here, secondary septation occurs to further specialize the alveolar structures and the capillary system is already closely surrounding the distal respiratory airways to provide a fully functional gas exchange together with the maturing alveoli [12, 21].

1.1.2 Specification of the murine lung epithelium

The proper specification of epithelial progenitor cells to a mature and functional lung epithelium with its distinct cell types sitting along the proximal-distal axis is first of all strongly dependent on the expression of transcription and growth factors in the developing endoderm, including *Nkx2.1* and *Fgf10*. As described in the previous section, cooperative and reciprocal signaling interactions between mesoderm and endoderm initiate and dictate the formation and branching of primitive lung epithelial buds. However, it is necessary to direct the emerging branching morphogenesis in a specific proximal to distal fashion, which guarantees a proper specification of the developing lung epithelium. Therefore, not only signals coming from the distal mesoderm, like *Fgf10*, are sufficient. Also signal gradients within the developing endoderm play an important role here. Accordingly, a high *Sox2* expression level in proximal endodermal progenitor lineages (see also Figure 1A) regulates their differentiation to cell types that are characteristic for tracheal and bronchial epithelium [22]. In contrast, the branching of distal progenitor lineages is marked by co-expression of the transcriptional regulators *Sox9* and *Id2* (Figure 1A) [23, 24]. Lineage tracing experiments have revealed that these *Sox9/Id2* double positive distal epithelial tip progenitor cells exhibit multipotent capacities promoting differentiation to all lung epithelial cell fates up to embryonic stage E13.5 [25]. At later stages their fate commitment gets restricted to distal lineages. Moreover, regulatory factors like the zinc finger protein Gata6 or proteins of the forkhead box (Fox) family, such as Foxa1 and Foxa2, are not only markedly involved in early branching morphogenesis but play also important roles in later epithelial specification as well as regeneration processes after injury. Though, it has been shown that *Gata6* is important for proper differentiation of bronchioalveolar stem cells (BASCs) during postnatal stages as well as for regeneration by regulating Wnt/ß-Catenin signaling [26]. During early lung development *Gata6* exhibits a synergistic action together with *Nkx2.1* in promoting epithelial differentiation [27]. *Foxa2*, which is expressed at high levels also in the primitive foregut endoderm, exhibits strong expression in the proximal epithelium during branching morphogenesis. Hence, it inhibits further branching of proximal regions and thereby directing the branching progression towards distal parts [28, 29]. Furthermore, *Foxa1* and *Foxa2* jointly promote transcription of genes that are crucial for the determination of different epithelial cell lineages in the maturing lung

epithelium such as the distal alveolar epithelial type 1 and type 2 cells (ATI and ATII), and also the more proximal resident secretory (Clara) cells as well as Ciliated cells for example. In general, a more distinct specification of the developing lung epithelium starts as previously mentioned with the saccular stage from E17.5 on followed by further postnatal maturation and secondary septation of the distal formed primitive sacculi during alveolarization progress. Once this last stage of maturation is completed, lung epithelium eventually comprises many different specific cell types that are distributed in a characteristic pattern along the proximodistal axis. By this pattern the mature respiratory epithelium can be subdivided from proximal to distal roughly into three sections, the tracheobronchial, intrapulmonary bronchiole and the bronchioalveolar region (Figure 2). The bronchioalveolar regions are mainly lined with long flat-shaped type 1 cells (ATI) and cuboidal type 2 (ATII) cells. While ATI cells are closely attached to the respiratory capillaries and therefore significantly facilitate gas exchange, ATII cells are characterized by their surfactant production (Sftpc or SP-C), which decreases the alveolar surface tension. Moreover ATII cells have been shown to contribute to alveolar homeostasis promoting absorption as well as secretion of fluid [30]. Another important feature of ATII cells is their potential to proliferate and to self-renew in the steady state and after injury, while ATI cells lack this ability [31]. ATI cells are derived from ATII cells during development and also after injury and are marked by *Aqp5* (Aquaporin 5) and *Pdpn* (Podoplanin) expression [32, 33]. Another source that is claimed to give rise to both proximal bronchiolar and distal alveolar cell types are the BASCs that are localized as sparse populations at the bronchioalveolar duct junctions and co-express *Sftpc* and *Scgb1a1* [34]. Clara Cells belong to the group of secretory cells and are marked by *Scgb1a1* (also CC10) expression. They line up in higher numbers along the more proximal bronchiolar region and represent as well another stem cell population. Clara cells have been shown to self-renew over time and they have the potential to give rise to ciliated cells, which express *Foxj1* as a characteristic marker. Ciliated cells are resident in rather proximal regions of the intrapulmonary bronchioles as well as in higher numbers along the tracheobronchial region [35]. These and some more characteristic cell types of the mature respiratory epithelium are depicted in Figure 2. In line with this, Table 2 lists a summary of all the epithelial cells together with their specific markers, localization and special functions and features.

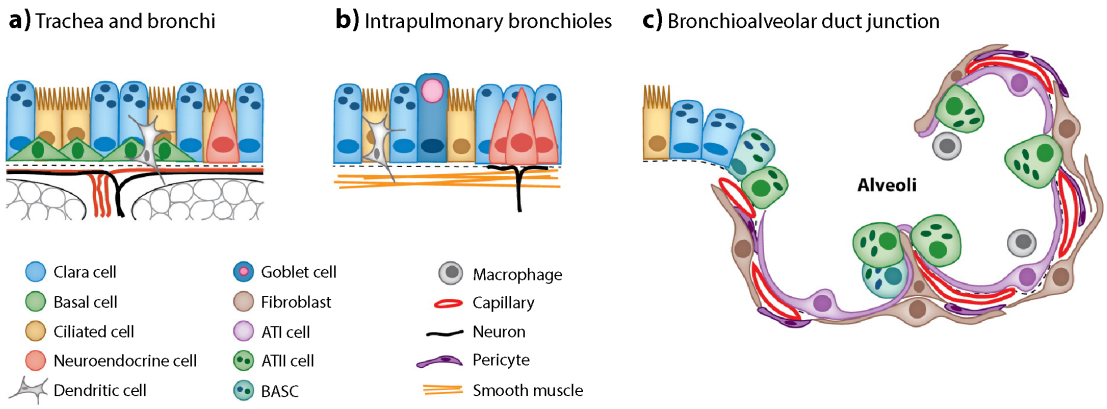

Figure 2: Proximodistal cell type pattern of the mature murine respiratory system.
Tracheobronchial region of the lung epithelium (a). This segment is marked by a pseudostratified epithelium consisting of basal, some individual neuroendocrine, ciliated (higher abundance) and Clara cells. The columnar epithelial segment of the intrapulmonary bronchioles (b) is characterized by a higher abundance of Clara and a lower amount of ciliated cells, a sparse distribution of goblet cells and clusters of neuroepithelial bodies (NEBs). The most distal segment comprising the alveoli (c) is lined by long and flat-shaped ATI and cuboidal ATII cells. In the region of the alveolar duct junction there are few Clara cells and a sparse BASC population. Figure adapted and modified from Rock, J. R. and Hogan, B. L. (2011) [36].

Cell type	Marker	Location	Features
ATI cell	*Aqp5, Cftr, Pdpn*	distal, alveoli	long, flat-shaped or squamous, gas exchange, alveolar fluid homeostasis, about 95 % of the lung surface area
ATII cell	*Sftpc*	distal, "corners" of alveoli	cuboidal, SP-C production to reduce surface tension and for host defense, alveolar fluid homeostasis, self-renewal, differentiation to ATI
BASC	*Sftpc, Scgb1a1*	alveolar duct junction	columnar, self-renewal, contribution to bronchiolar and alveolar lineages, tissue stem cell
Clara cell	*Scgb1a1*	proximal, high intralobar bronchiole, lower tracheal/ bronchi abundance	columnar, secretory cell, secretoglobin production, contribute to mucociliary clearance of microorganisms and particles, self-renewal, can differentiate to Ciliated cells, tissue stem cell
Ciliated cell	*Foxj1*	Proximal, high in trachea/bronchi, lower intralobar bronchiole abundance	columnar and apically multiciliated, contribute to mucociliary clearance of microorganisms and particulates
Basal cell	*Trp63, Krt5, Krt14*	proximal, trachea and bronchi, as separate layer attached to the basal lamina	desmosomal and hemidesmosomal attachments, structural functions [37], self-renewal, tissue stem cell pool, differentiation to ciliated and secretory lineages [38, 39]
Goblet cell	*Scgb1a1, Spdef, Muc5ac*	proximal, sparse, intralobar bronchioles	columnar, mucus production, involved in obstructive lung diseases [40]
Neuro-endocrine cell	*Calca, CGRP, Ascl1*	proximal, individually in trachea/bronchi, as clusters in bronchioles	columnar, sensing stimuli in the airway lumen (hypoxia, nicotine), secretory, production of serotonin, calcitonin and bombesin, influence of epithelial cells, immune function or air/blood flow [41], clustering in neuroepithelial bodies (NEBs)

Table 2: Cell types of the mature respiratory epithelium and their features.

1.1.3 Wnt/ß-Catenin signaling during lung epithelial development

The following section will provide an overview of canonical Wnt/ß-Catenin signaling and its implication in lung epithelial development. Canonical Wnt signaling involves the molecule ß-Catenin, which is associated to cadherin-mediated cell adhesion, as a transmitter of signals that are relevant for development and regeneration [42, 43]. The general mechanism of Wnt/ß-Catenin signaling is shown in Figure 3.

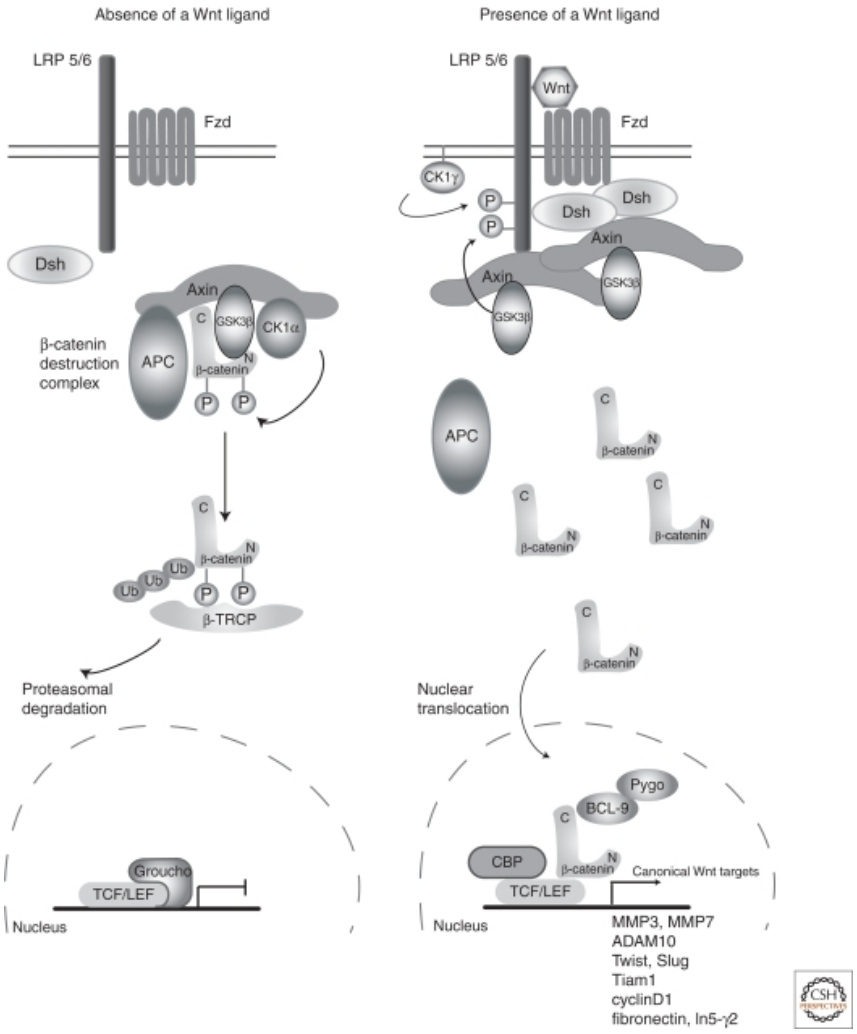

Figure 3: Wnt/ß-Catenin signaling pathway.
Absence of a Wnt ligand: ß-Catenin levels are kept low through its interaction with the destruction complex consisting of APC and Axin as well as the kinases CK1α, GSK3ß, which mediate subsequent phosphorylation of ß-Catenin leading to its proteosomal degradation initiated by the E3 ubiquitin ligase component ß-TrCP. This prevents the interaction of ß-Catenin with the transcription factors LEF1 and TCF in the nucleus. In the presence of Wnt ligands a receptor complex of Frizzled (Fzd) and LRP5/6 forms by recruiting Dishevelled (Dsh) to the intracellular domain of phosphorylated LRP5/6, which is promoted by CK1γ and GSK3ß. Subsequently, this leads to interaction of Dsh with Fzd and polymerisation with other Dsh molecules. Thereby, Axin gets recruited to the phosphorylated LRP5/6 receptor resulting in a destabilization of the ß-Catenin destruction complex and a cytoplasmic accumulation of ß-Catenin. Eventually, translocation of ß-Catenin into the nucleus, replacement of Groucho as well as interaction with TCF/LEF and additional co-factors (Bcl9, CBP, Pygo) drives the expression of downstream targets. Figure adapted from Heuberger, J. and Birchmeier, W. (2010) [43].

In the absence of Wnt ligands the cytosolic ß-Catenin levels are kept low through its enhanced proteasomal degradation, promoted by CK1α and GSK3ß mediated phosphorylation of ß-Catenin in the Axin/APC destruction complex. However, the binding of Wnt ligands to Frizzled (*Fzd*), a seven transmembrane receptor, initiates its heterodimerization with the Lrp5/6 transmembrane receptor. This receptor complex further interacts with Dishevelled (*Dsh*) at the intracellular part, which promotes phosphorylation of Lrp5/6 by GSK3ß, CK1γ and other kinases. Hence, Axin gets recruited to the intracellular domain of the phosphorylated LRP5/6 receptor thereby leading to a destabilization of the destruction complex followed by an accumulation of ß-Catenin in the cytoplasm. The cytoplasmic ß-Catenin eventually translocates to the nucleus where it binds together with other co-factors like Bcl9, Pygo or CBP to the transcription factors TCF/LEF. Ultimately, these interactions lead to the transcriptional activation of Wnt/ß-Catenin downstream targets by replacing the Groucho repressors. As described in the previous section it has been shown that Wnt/ß-Catenin signaling plays a fundamental role during lung development. Besides the fact, that mesodermal derived Wnt signals (Wnt2/2b) have a direct impact on Nkx2.1 expression in the lung epithelium marking the early lung budding, Wnt/ß-Catenin signaling is an important signaling pathway throughout entire lung epithelial development. Wnt-reporter lines like TOPGAL and BATGAL revealed a ß-Catenin expression pattern emerging in epithelial precursors of the early endodermal tube and lung buds from embryonic day E9.5 on, which is maintained during early lung branching [44, 45]. While the lack of ß-Catenin in the developing proximal respiratory epithelium has no effect on the structural specification of the lung, an early ß-Catenin inactivation in the distal epithelium impairs normal distal epithelial development characterized by a loss of *Sftpc* expression and a simultaneous proximalization of lung epithelium [46, 47]. These data revealed a notable importance for Wnt/ß-Catenin signaling in proximal-distal patterning and specification of distal respiratory epithelium.

1.2 Lung diseases and regeneration

In order to analyze the response of a certain tissue to its damage it is important to keep in mind that all tissues differ in their capability to self-renew senescent or injured cells. Some tissues like intestine, skin or the hematopoietic system exhibit a high potential of repair and renewal with a constant turnover of their cells already

during adult homeostasis due to their well-defined setting of stem/progenitor cells. Other organ systems like heart or brain are marked by quiescence during adulthood and show only poor response to tissue damage. The lung resembles a quiescent tissue system with a very slow cellular turnover during adult stages but contains, as already described in the previous sections, several cell populations along its proximal-distal epithelial axis that retained tissue stem cell characteristics. Intriguingly, these various stem/progenitor cell niches of the tracheobronchial (basal stem cells), intrapulmonary bronchiolar (clara stem cells) or alveolar region (BASCs and ATII cells) are not only capable to contribute to regeneration of local injury as recent studies also report about the existence of stem/progenitor cells that migrate to distant areas of damaged tissue. Trp63/Krt5 positive basal cells are able to migrate from the area of their origin in the tracheobronchial niche to distal alveolar regions to repopulate damaged ATI and ATII cells, after injury through H1N1 influenza virus infection [48]. These features eventually enable the lung to respond with robust regeneration to injury and disease. During the process of repair both activation of different progenitor cell niches and replacement of damaged tissue by proliferating undamaged cells is required [25, 39, 49, 50]. Overall, respiratory diseases are characterized by their pathological changes in the cellular composition and physiological functions of the airway epithelium. These epithelial abnormalities usually marked by loss of damaged cells, expansion and migration of surviving epithelial cells, hyperplasia, altered proliferation or impaired differentiation, might directly disturb lung function [51]. Airway obstructions caused by an increased mucus secretion of hyperplastic secretory cells, squamous metaplasia, dysplasia or malignant transformation, can be the result of these pathological alterations in the epithelium. Mutually, thickening of the basal lamina, smooth muscle hyperplasia, fibrosis and chronic inflammation account for mesenchymal lung perturbations. Combinations of these changes are commonly found in human lung diseases like chronic asthma, cystic fibrosis, chronic obstructive pulmonary disease (COPD) or cancer. In order to study the molecular pathways and mechanisms that are relevant for tissue regeneration and which drive these processes of pathologic remodeling after damage or during disease, a variety of different mouse injury models have been established. Ideally, a mouse model should mimic the pathological state of a human disease as close as possible. Gained insights in the occurring physiological and pathological changes can thereby ultimately be translated for therapeutic purposes. The robust reproducibility of an injury phenotype as well as

the simplicity to induce it resemble as well quite important criteria considering the application of a murine injury model. Induction of pulmonary fibrosis in mice is a good example for such kind of injury models that combine all these features to study idiopathic pulmonary disease (IPF). The following sections will provide a more detailed overview about this murine lung injury model as well as its importance for a better understanding of IPF.

1.2.1 IPF and a murine fibrosis model

Idiopathic pulmonary disease (IPF) is a rare human disease with severe features of a progressive lung structure disruption by fibrotic scars causing stiffness and the loss of its physiological function in providing a proper gas exchange. About 5 million people worldwide are affected, while incidents tend to increase [52]. The prevalence of this disease is about 20 per 100000 people for men and 13 per 100000 people for women [53] showing an average outbreak of the disease at an age greater than 50. Causes for this interstitial lung disease are still poorly defined but it is currently believed that cigarette smoke, exposure to certain dust particulates like metal, silica or wood belong to the potential risk factors [54, 55]. The chance of genetic transmission is existent but low [56]. Currently there are no effective medical treatments available to cure this disease. Hence, the necessity of using appropriate animal models to study the cellular sources and mechanisms that contribute to the progression of IPF gained increased importance. Therefor, various animal models of lung fibrosis have been established and characterized, which resulted so far in the identification of pathologically affected cellular targets, molecular pathways and processes that might be crucial as well in human disease. Although there is still some controversy, three cell sources have been suggested as potential fibrogenic populations, namely intrapulmonary fibroblasts or pericytes, bone marrow-derived stem cells and alveolar epithelial cells [57-60]. However, recent studies strongly propose alveolar epithelial cells as the most likely source triggering fibrogenesis. In this respect it is believed that abnormally activated ATII cells might either directly generate myofibroblasts via the process of epithelial to mesenchymal transition (EMT) [61] or stimulate and activate resident fibroblasts by secretion of signaling molecules mediating their differentiation to profibrotic myofibroblasts [62]. Thus, after their formation in fibrotic foci activated myofibroblasts promote scarring and disruption of lung architecture by their enhanced production and deposition of extracellular matrix proteins, like collagens or matrix

metalloproteinases. In order to induce pulmonary fibrosis in mice the usage of several different approaches evolved like for example the application of inorganic particles (silica) [63], FITC instillation [64], exposure to irradiation [65], gene overexpression models (TGFß) [66, 67], H1N1 influenza virus infection [48] or administration of bleomycin [68, 69]. The bleomycin injury model is the most extensively used animal model to induce pulmonary fibrosis. Bleomycin, originally a chemotherapeutic drug, is easy accessible and its application is relatively simple. The most common way to administer this profibrotic agent is its pharyngeo- or intra-tracheal instillation. This leads to the development of bronchiolocentric accentuated fibrotic changes, similarly found in human disease [70], over a time frame of only 14 to 28 days. Intravenous or intraperitoneal application is as well possible but results only in subpleural scarring. In detail, intra-tracheal induced bleomycin injury is characterized by acute interstitial and intra-alveolar inflammation, enhanced accumulation of neutrophils and activated macrophages, epithelial cell damage with consequent hyperplasia, disruption of the basement membrane as well as upregulation of cytokines like TNF-alpha, IL-6, IL-8, TGF-ß and CTGF [69, 71]. Thereby, the bleomycin animal model closely mimics several pathologic features that are reproducible, consistent and can also be observed in IPF. Despite its dose dependent reversibility, which is inconsistent with human disease, the bleomycin animal model provides a highly beneficial system to study injury responses and progression of pulmonary fibrosis in regard to discover medical treatments for this devastating disease.

1.2.2 Signaling pathways in pulmonary fibrosis

Molecular signaling and communication between cells of the same or different tissues is not only important during development but also plays a crucial role in regeneration and repair. Signaling pathways that play an important role during lung development have been studied and well characterized over the past decades. These studies further provided considerable evidences delineating a deregulation of some embryonic pathways in lung disease or injury by using animal models. Thereby, these indications strongly suggest a fundamental role of reactivated developmental programs during processes of tissue remodeling or repair following abnormal stimulation. Wnt/ß-Catenin pathway marks one of the signaling pathways that is essential for early lung morphogenesis and specification, as described above, but gets reactivated again during the progression of pulmonary fibrosis. IPF patients for example exhibit an

enhanced expression of diverse members of the Wnt/ß-Catenin pathway like secreted Wnt ligands (*Wnt1, 7b, 10b*), Frizzled receptors (*Fzd2, 3*), ß-Catenin or *Lef1* [72]. The increased expression of those components has been localized to alveolar epithelial cells. Simultaneous upregulation of Wnt target gene expression additionally suggests functional signaling leading to hyperproliferation of epithelial cells. Moreover, a pronounced secretion of Wnt ligands derived from these aberrant ATII cells results in the stimulation and activation of myofibroblasts, which respond with an excessive extracellular matrix deposition [72-74]. These phenotypic observations can be similarly achieved in bleomycin treated mice [62]. Another critical pathway, which triggers pulmonary fibrosis, is represented by TGFß signaling. Several studies, including TGFß overexpression models [66, 67], revealed its significant contribution to the progression of this disease. These studies indicate that TGFß acts as an important cytokine, which is able to induce migration, proliferation and differentiation of mesenchymal cells like fibroblasts by regulation and activation of additional cytokines, including platelet-derived growth factor (PDGF), tumor necrosis factor alpha (TNF-alpha), fibroblast growth factor (FGF), epidermal growth factor (EGF) or endothelin-1 [75]. TGFß thereby acts as a chemotactic factor secreted by alveolar epithelial cells to mobilize resident fibroblasts and to induce their differentiation to myofibroblasts as well as the production of matrix proteins [71]. Further studies provide evidence that epithelial cells not only stimulate myofibroblast differentiation and their matrix protein deposition but also might contribute directly to the expansion of a myofibroblast population by EMT [76]. This process is described by the transformation of epithelial cells to cells that acquire mesenchymal properties characterized by enhanced motility and interstitial matrix production. EMT is mainly induced and driven by TGFß-signaling involving key regulators such as *Snai1, 2* and *Twist*. Both factors are upregulated in IPF affected lungs especially in hyperplastic ATII cells [77-79]. Last not least, there are yet other signaling molecules that have been implicated in IPF, namely sonic hedgehog (Shh) and phosphatase and tensin homologue (Pten). Similar to TGFß, Shh represents an important mediator of early branching morphogenesis in lung. However, it has been shown that under disease conditions, e.g. IPF, Shh expression was upregulated especially in epithelial cells located in areas of fibrotic foci while its receptor Patched 1 is highly abundant in infiltrating immune cells [80]. This suggests a communication of the aberrant epithelial cells with the immune system during pulmonary remodeling processes of

damaged lung tissue. Pten on the other hand, as a regulator of cell polarity, proliferation and apoptosis [81], displays an attenuated expression in myofibroblasts that accumulate in fibrotic foci of IPF lungs. It is suggested that this circumstance explains an increased resistance of myofibroblasts to apoptosis. Furthermore, *in vitro* studies demonstrated that Pten inhibits myofibroblast differentiation, which is an important feature of fibrogenesis [82]. In summary, a better understanding of such deregulated developmental signaling pathways during damage induced tissue remodeling, remains an important issue concerning the development of more efficient medical therapies or drugs. However, there are recent studies that have already successfully identified potential therapeutic targets of the disease involved signaling pathways promising an amelioration of pulmonary fibrosis such as the Wnt signaling downstream target Wisp1 (Wnt1-inducible signaling protein 1). Animal models of bleomycin induced pulmonary fibrosis as well as *in vitro* studies have shown that Wisp1, which is extensively secreted by ATII cells during fibrosis, induces ATII cell hyperplasia as well as activation of myofibroblasts and their matrix production in a paracrine manner [62]. Hence, targeting Wisp1 attenuates the fibrotic phenotype and might serve as a therapeutic target.

1.3 Controlling gene activity via inducible Cre-loxP systems

The identification of the Cre-loxP recombination system considerably revolutionized the control and modulation of gene activity in different eukaryotic model systems [83-85]. In order to use this system in various experimental approaches it was increasingly refined over the past decades and thus became indispensable for modern genetics. However, especially the functional characterization of genes that are relevant during the development of an advanced model organism like the mouse promoted the need for more specialized approaches. The generation of *loxP* site-specific recombination systems allowing conditional regulation of *in vivo* gene expression (activation or inactivation) was achieved by driving the *Cre* gene expression under the control of tissue-specific promoters. This enables a tissue restricted gene recombination during embryo- or organogenesis in order to prevent embryonic lethality and to study tissue-specific gene functions at later developmental stages. Though, the control of gene modulation underlies the temporal and spatial expression pattern of the corresponding developmentally regulated and tissue-specific promoter mediating an irreversible Cre-recombination induced loss or gain of gene function. Hence, tissue-specific inducible

recombination systems were designed to govern reversibility of genetic modifications at any desired time point. Thereby it is beneficial to develop a regulatory system, which creates no off-target effects, can be efficiently induced in all cells, guarantees a low basal but high induced expression levels and is easy to establish *in vivo*. One of these inducible recombination systems, which fulfill all these beneficial criteria, is the bacterial tetracycline-dependent regulatory system. While this system was slightly modified for eukaryotic organisms, the original role and function of the tetracycline-system (Tet-system) in bacteria (*Escherichia coli*) is the regulation of their antibiotic resistance against tetracycline (Tet) [86]. In the absence of Tet, a Tet-repressor protein TetR is expressed. TetR binds to its operator in the promoter region of the *Tn10*-specified tetracycline-resistance operon (*tetO*), which consequently leads to the limitation of its own expression and the transcriptional repression of the Tet-resistance gene (tet^{Res}) (Figure 4A). In the presence of Tet, which easily penetrates the bacteria or cells by passive diffusion [87], Tet interacts with TetR mediating its conformational change. This structural change of the regulatory element leads to a loss of binding affinity for *tetO*, which results in the expression of the resistance protein. In order to improve this basic system a tet-controlled transactivator (tTA), which comprises the tetR fused with the C-terminal domain of the virion protein 16 (VP16) derived from *herpes simplex virus* [88], was generated. VP16 is a strong transcriptional activator of viral genes and thereby enables the tTA fusion protein to effectively stimulate minimal promoters (*TATA*-box) that can be combined with *tetO* sequences, in total representing the tetracycline responsive element (*TRE*). Their silenced activity at low Tet concentrations (Tet-Off), which prevents transactivation of the repressed genes downstream of the *tetO* sequences by tTA, is a clear advantage of this TRE system. Together, the specificity of tetR for its operator [86], the high affinity of tetracycline for tetR [89] combined with the high transactivation potential mediated by the tTA-VP16 fusion protein [90], creates the basis for a highly efficient inducible recombination system. Hence, this system allows the temporal and spatial regulation of gene inactivation or overexpression in all tissues by application or withdrawal of the tetracycline derivate doxycycline (Dox). An alternative system that requires Dox for the activation of the Tet-repressor protein promoting its binding to the *TRE* is provided by the mutated version of tTA, which was also found in *Escherichia coli*. This reverse Tet-dependent transactivator (rtTA), fused with the VP16 domain, finally enabled the generation of a Dox inducible system, which can be

activated upon administration of Dox (Tet-On, Figure 4B) [90]. In combination with Cre/loxP, this system offers a powerful tool to induce and activate Cre mediated recombination of a floxed target gene, which we also attempted in this study.

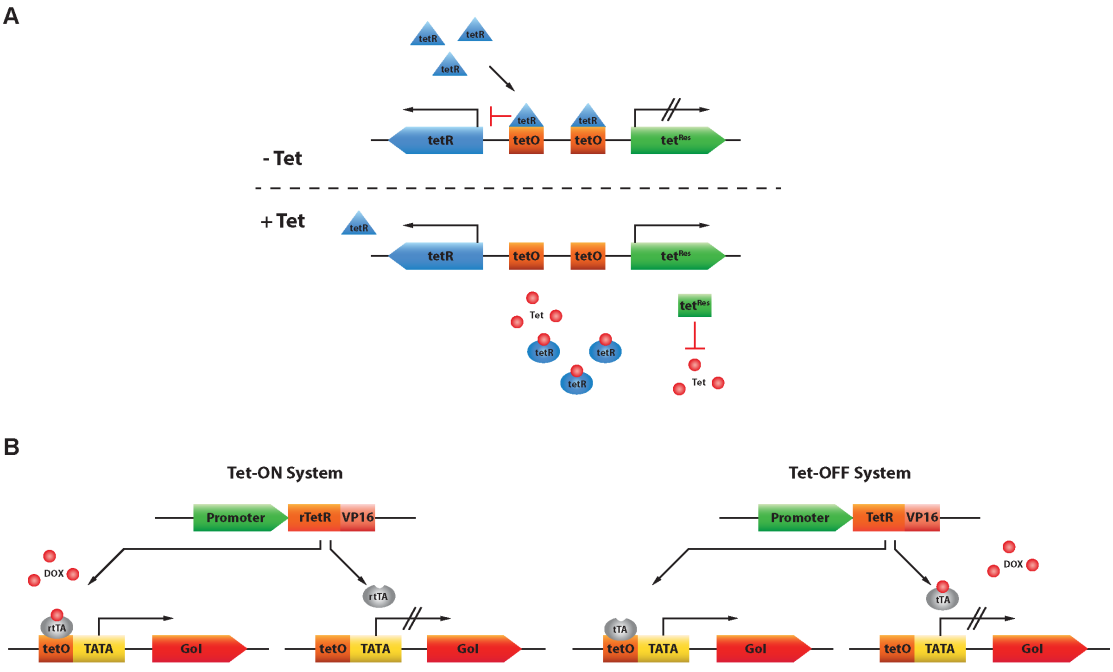

Figure 4: Tetracycline dependent gene regulatory systems.
A: Procaryotic tetracyclin-dependent regulatory system (*E. coli*). Tet-system is silenced in the absence of Tet. TetR (blue) interacts with Tet-operator (*tetO*) sequence (orange) repressing the tet^{Res} gene (green) and limits also its own expression. In presence of Tet (red), TetR binding to *tetO* is abolished due to conformational changes. Consequently, the Tet-resistance gene (tet^{Res}) expression is switched on and promotes bacterial resistance against Tet. **B:** Eucaryotic doxycycline inducible Tet-On and –OFF system. In the Tet-ON system the default state is a repression of the gene of interest (*GoI*, red), due to the inactive form of rtTA (grey), a fusion protein of mutated TetR and VP16 (magenta). Upon application of Dox rtTA gets activated, binds to the *TRE* (tetO & minimal promoter i.e. TATA, yellow) and drives *GoI* expression. The vice versa model Tet-OFF is permanently switched on as default state. To repress the system it is necessary to apply Dox in order to induce inactivation of the tTA transactivator and consequently inhibition of *GoI* expression.

However, this system provides the major advantage of reversibility compared to the conditional alteration of gene expression mediated via constitutive Cre/loxP systems or analog also Flp-FRT, another site-directed recombination technology [91]. The use of inducible systems emerged tremendously and remains till today a versatile method not only to generate genetic knockout or overexpression models but also to study stem/progenitor cell fate relations during normal and pathological development. The discovery of the *Rosa26* locus in mice by Philippe Soriano in 1991 [92] allowed to generate reporter mouse strains by the insertion of specific reporter genes like *GFP*, *YFP* or *LacZ* into this locus flanked by *stop-flox* sites that enable an activation of

reporter gene expression only after Cre-expression and recombination. Thereby, the joint application of Cre-expressing systems together with reporter gene mouse lines, like *Rosa26-Stopflox-LacZ* or *Rosa26-Stopflox-eYFP* permits the visualization of Cre mediated recombination activity in cells. Thus, especially doxycycline induced Cre-reporter gene expression provides an eclectic tool to investigate tissue-specific lineage and cell fate origins in developing or regenerating tissues. Such lineage tracing experiments have been extensively studied in different tissues so far, including lung. As mentioned above, lineage tracing studies thereby revealed novel stem/progenitor cell pools that are relevant during lung epithelial specification as well as after lung injury using the Tet-system under the control of lung epithelial specific promoters like *SPC* or *CC10* (*SPC-rtTA, CCSPrtTA* [93]). Hence, the identification of different cell type specific markers is essential in order to design Cre-recombination systems that exhibit restricted tissue specificity. Taken together, inducible Cre-loxP systems are indispensable whenever a higher resolution in the temporal-spatial control of gene activity is needed.

1.4 Numb and Numblike – multifunctional proteins

The multifunctional protein Numb was originally discovered in *Drosophila Numb* mutants, which display changes in the establishment of cell identities derived from sensory organ precursors [1]. Thus, it has been suggested that Numb plays a critical role in cell fate determination during development of sensory neurons in the peripheral nervous system of *Drosophila*. The membrane-associated protein Numb has further been shown to localize in an asymmetrical manner as a cortical crescent to one pole of a dividing sensory organ precursor cell [94, 95]. Hence, during this process of asymmetric cell division Numb gets segregated to the developing daughter cell, where it further promotes cell fate decisions via an interaction and inhibition of Notch-signaling cascade [96]. The evolutionary conserved Numb has two mammalian homologs, namely *Numb* and its cytosolic homolog *Numblike* [97, 98]. Mammalian Numb, which exhibits closely related cellular functions to Drosophila Numb, however displays much more versatility in mammals. This will be highlighted more detailed in the following sections.

1.4.1 Structural features of Numb and Numblike

Both, mouse and human Numb and Numblike share a high similarity in their protein structures. Numb has four different biological active isoforms that are derived from four alternatively spliced transcript variants, which differ in the sequences encoding for protein domains of two major binding sites of the Numb protein (Figure 5) [99, 100]. One of the alternative peptide sequences is located in the N-terminal phospho-tyrosine-binding domain (PTB) comprising an 11 amino acid insert that is present in Numb isoform 1 and 2 (Numb1 and 2) and absent in isoform 3 and 4 (Numb3 and 4).

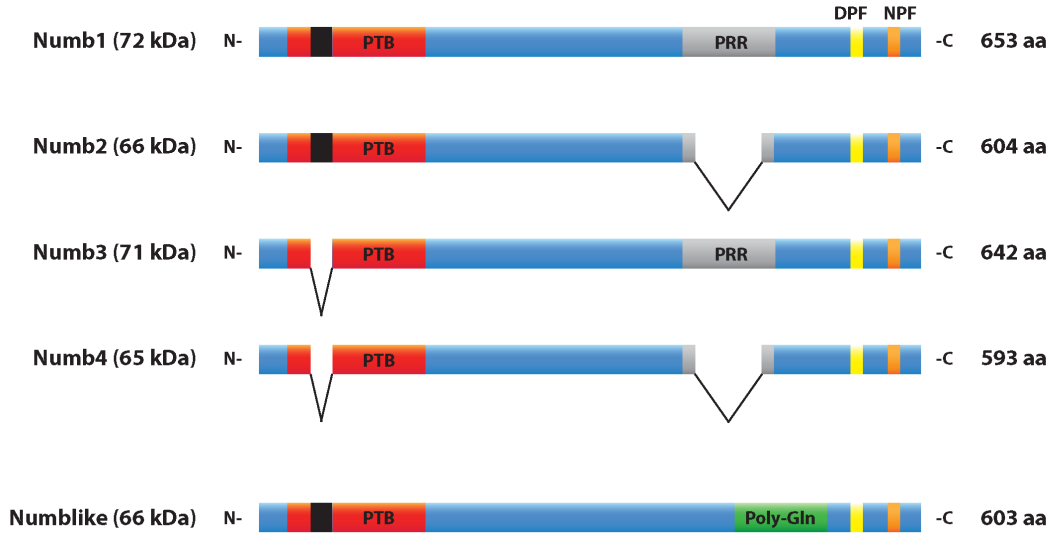

Figure 5: Structural features of Numb and Numblike.
Mammalian Numb is encoded by four alternatively spliced transcript variants. Each of the protein isoforms have an N-terminal phospho-tyrosine binding domain (PTB, red) and a C-terminal proline-rich region (PRR, grey). Numb3 and 4 lack 11 amino acids in their PTB domain, which are included in Numb1 and 2 (black). The N-terminal PRR domain of Numb2 and 4 are missing 48 amino acids that are included in Numb1 and 3. This results in four different protein isoforms of a molecular mass between 65 and 72 kDa. Moreover, all isoforms are characterized by C-terminal located DPF and NPF motivs. Numblike is structurally highly similar to Numb1 isoform but lacks the PRR domain in the C-terminus while it contains a repeat of 15 glutamines. Furthermore, Numblike also includes DPF and NPF motivs. The length of each protein is depicted by the number of amino acids (aa).

Correspondingly, the isoforms that contain the PTB insert are exclusively membrane-associated, while those without the insert localize in the cytoplasm. The second alternative peptide sequence spans 48 amino acids of the C-terminally located proline-rich region (PRR) that is present in Numb1 and 3 or missing in Numb2 and 4. Furthermore, all Numb isoforms contain Eps15 (EH) homology domains (DPF and NPF), which enroll Numb in endocytic functions [101, 102]. Mammalian Numblike on the other hand shows a strong sequence similarity to mammalian Numb and to a

smaller magnitude also to *Drosophila* Numb [98]. Like Numb it contains a N-terminal PTB-domain but lacks the C-terminal PRR-domain. Moreover, Numblike contains a poly-glutamine stretch in its C-terminal region, which is missing in all four Numb isoforms. Besides this, its subcellular localization is restricted exclusively to the cytoplasm, where Numblike is homogenously distributed. Although, its functions have been less well characterized yet, Numblike is believed to partially mimic the functions of Numb, according to its high structural similarity to Numb1, but it might likely inherit distinct functions in the cytosol as well. However, specific subcellular localization and structural features given by the interaction domains of the different isoforms enable Numb to interact with a broad spectrum of proteins serving as an adaptor protein involved in divers cellular functions.

1.4.2 Functional features of Numb and Numblike

As already mentioned previously Numb has originally been identified in Drosophila, where it exerts Notch-signaling inhibition during cell fate determination of sensory organ precursors. In brief, Notch proteins (*Notch1-4*) are transmembrane receptors presenting their extracellular domain to their ligands Delta-like (*Dll1-4*) or Jagged (*Jag1, 2*), which are expressed by neighboring signal sending cells. Upon binding of the ligand to the Notch extracellular domain cleavage of the Notch intracellular domain (NICD), mediated by γ-secretase, occurs leading to the translocation of NICD to the nucleus where it binds to CSL (RBPJκ) and promotes expression of Notch-signaling target genes like the *hes* or *hey* family [103, 104]. Similar to *Drosophila* Numb, mammalian Numb can directly interact with NICD. Through additional recruitment of the E3-ubiquitin ligase Itch, which thereby interacts with the PTB domain of Numb, polyubiquitination of NICD is mediated initiating its consequent degradation by the proteasome. Hence, translocation of NICD to the nucleus is abolished leading to the inhibition of canonical Notch signaling [6]. At this juncture, the involvement of Numb in endosomal trafficking plays a crucial role in controlling the internalization of the Notch receptor, thus contributing to a suppression of signal transduction [5]. It has been shown that Numb interacts with α-Adaptin, Eps15 or EHD, components of the Clathrin mediated endosomal trafficking machinery, via the DPF and NPF domains. Thereby Numb regulates membrane-tethered receptors like Notch by recruiting them into early endosomal vesicles followed by either their recycling and reorganization to the cell surface or their degradation [5, 102]. The

interaction between Numb and Itch has furthermore been reported to mediate proteasomal degradation of Notch receptors as well as Gli1, which is a transcription factor acting downstream of Hedgehog-signaling [105, 106]. The Hedgehog pathway, an important regulator of tissue development, plays a fundamental role also during self-renewal of neural progenitor cells and their physiological maintenance [106]. The proteasome-dependent degradation of Gli1 initiated by Numb/Itch association results in the inhibition of Hedgehog signals, which in turn promotes the differentiation of neural stem cells. This further emphasizes Numbs function as a cell fate determinant. Besides its interaction with the E3-ubiquitin ligase Itch, Numb has also been shown to associate with other E3 ligases like LNX, Siah-1 or Mdm2 via the PTB domain [8, 107, 108]. These E3 ligases directly mediate the polyubiquitination of Numb itself and thereby regulate its abundance promoting degradation of Numb by the proteasome. By Numb binding to Mdm2, which is simultaneously regulating the levels of the tumor suppressor p53, furthermore has a stabilizing effect on p53 [109]. Finally, Numb has also been reported in mediating cell migration and adhesion. Both of these processes are closely related since trafficking and redistribution of adhesion molecules like integrins is necessary for the action of cell migration. Numb has thereby been implicated in directing the endocytic trafficking of directly associated Integrin-ß to membrane protrusions at the leading edge of the cell, where it is fundamental for the progression of cell movement [110]. This process is further regulated by the phosphorylation of Numb through atypical protein kinase C (aPKC), which promotes its release from Integrin-ß and clathrin-coated sites at the protrusions. Moreover, Numb as well as Numblike have been shown to mediate and maintain adherens junctions and cell polarity in neural stem cells and in epithelial cells [10, 111]. In this respect, Numb binds directly with E-Cadherin via the PTB domain to stabilize the adherens junctional complex at the lateral part of the cells. Besides the interaction with E-Cadherin, it has been shown that Numb interacts with Par3 of the polarity complex Par3-aPKC-Par6, which additionally promotes maintenance of cell-cell contacts as well as polarity of epithelial cells [10]. At this juncture, cell contacts and polarity can be negatively regulated by Src tyrosine kinase or HGF stimulation, which destabilize Numb interaction with E-Cadherin and Par3, likely mediating EMT [10]. In addition to this, it has been shown that a loss of Numb in epithelial cells results in mislocalization of E-Cadherin and ß-Catenin from baso-lateral to apical domains, which consequently causes disruption of the adherens junctional complex

[10]. *In vivo* studies of epicardial development in mice revealed similar results showing that vice versa epicardial specific depletion of ß-Catenin results in disruption of adherens junctions as well accompanied by mislocalization of Numb and randomization of mitotic spindle orientation within epicardial cells [112]. Mice that lack both Numb and Numblike in epicardial cells also show a randomized orientation of mitotic spindle [112]. Regardless of Numb potential to interfere with the Notch-signaling cascade [98, 113] and its contribution to cell adhesion and polarity maintenance [111, 112], Numblike functions still remain, unlike those of its homolog Numb, less well studied. However, there is some data suggesting that Numblike, differently from Numb, does not exert stabilizing and enhancing effects on p53. In addition to this observation Numblike rather potentiates downstream signaling of Shh (sonic hedgehog) than reducing it, resulting in an advanced expression of pluripotency markers like Sox2 or Oct4 in embryonic stem cells [113]. Moreover, Numblike is similar to Numb (see following section) involved in tumorigenesis. There are studies, which revealed an increased expression of Numblike in divers human tumors including lung cancer [114]. This Numblike overexpression is related to a loss of the tumor suppressor *miR-296*, a micro-RNA that directly inhibits translation of Numblike. During cancer progression Numblike thereby maintains together with Klf4 signaling a pool of cancer progenitor cells. However, this data only suggested correlations of Numblike expression with tumorigenesis but does not yet explain specific and mechanistic functions of the Numblike protein in this process so far. In summary, all these findings underline once more the homologies of both Numb and Numblike but highlight as well that they potentially inherit distinct and specific functions.

1.4.3 Numb and Numblike during development and disease

The roles of Numb and Numblike have been well described during neurogenesis in *Drosophila* and also mammals. Both have been implicated as cell fate determinants of neuronal progenitor cells, regulating their differentiation [97, 98]. However, both genes are widely expressed also in other tissues during development and adulthood implicating that their purpose is not restricted to the development of the nervous system [97, 115]. Moreover, the different isoforms of Numb (isoform 1 – 4) seem to play distinct roles at different developmental stages. The long isoforms Numb1 and 3, containing the 48 amino acid insert in their PRR-domain, are expressed early during

neural development between E7 and E10, emphasizing their role rather in controlling proliferation. The shorter isoforms Numb2 and 4 on the other hand are expressed during all developmental stages and also in mature brain, suggesting their importance for differentiation [99, 100, 116]. Total gene inactivation studies demonstrate that Numblike depleted mice are viable and don't exhibit any severe defects except an infertility of homozygous mutant females. Homozygous loss-of-function mutants for Numb in contrast are embryonic lethal and die at stage E11.5. These animals reveal prominent defects in cranial neural tube closure and precocious neuron production in the forebrain at this stage [117]. However, the cause of their lethality is most likely the result of vascular defects, since the embryos show extensive bleeding as well. Indeed, both Numb and Numblike inherit common roles in maintenance of neural progenitor cells during neurogenesis. Neural tissue specific inactivation of the two cell fate determinants during embryogenesis shows that early neurons emerge at a normal time point while the expansion of self-renewing neural progenitor cells fails leading to a loss of dividing cells shortly after onset of neurogenesis resulting eventually in a highly specific malformation of the neocortex and hippocampus [118, 119]. Observations of an asymmetric localization of Numb to the apical membrane in dividing progenitor cells propose a general mechanism for mammalian stem cells to regulate self-renewal and differentiation by Numb-mediated asymmetric cell division [97, 119, 120]. Further evidence for redundant functions of *Numb* and *Numblike* was provided by combined constitutive knockout studies for both genes resulting in an earlier embryonic lethality at E9.5. The severe and widespread defects depicted by these *Numb/Numblike* double mutants suggested a fundamental role of both proteins in regulating proliferation and differentiation also in other tissues than the central nervous system [118]. Tissue specific deletion of both *Numb* and *Numblike* in developing epicard for example results in embryonic lethality between E12.5 and E14.5 suggesting an important role of both proteins during heart specification [112]. As previously mentioned, the loss of *Numb* and *Numblike* specifically in developing epicardial cells results in disruption of adherens junctions and cell polarity similar to an epicardial specific deletion of *ß-Catenin* [112]. Additionally, it is believed that the proteins Numb, Numblike and ß-Catenin synergistically control the orientation of mitotic spindle and thereby direct the division of epicardial cells [112]. Moreover, Numb and Numblike once more have been shown to interfere with Notch signaling during heart development as well [2]. Here, Numb and Numblike are capable to

suppress Notch2 activity during the process of myocardial compaction, trabeculation and ventricular septum formation. Only the concomitant inactivation of both genes results in an upregulation of Notch2 activity accompanied by Bmp10-signaling with defects characterized by hypertrabeculation as well as incomplete myocardial compaction and ventricular septum development. Thus, Numb and Numblike were identified as important inhibitors of Notch- and Bmp10-signaling in mouse heart development. Furthermore, Numb is highly expressed in developing and adult lung epithelium with a characteristic cortical distribution of the adaptor protein [99, 121]. Distal lung epithelial progenitors exhibit asymmetric segregation of Numb to their apical pole similar than in neural progenitor cells. In these distal epithelial progenitor cells, Numb has been shown to promote cell polarity as well as asymmetric cell division, which are both features that play an important role during the progress of proper lung morphogenesis and epithelial specification [122, 123]. Consistent with this observation, the polarity proteins Inscuteable (Insc), G-protein-signaling modulator 2 (Gpsm2/LGN), Nuclear mitotic apparatus protein 1 (NuMA) as well as the Eyes absent protein 1 (Eya1) depict asymmetric distribution in distal embryonic lung epithelium similar to Numb localization and exhibit the potential to regulate mitotic spindle orientation during lung epithelial morphogenesis [122, 124, 125]. Functional disruption of these polarity proteins *in vitro* randomizes mitotic spindle orientation and negatively influences the balance between proliferation and differentiation. In case of *Eya1*, *in vitro* but also *in vivo* inactivation of *Eya1* impairs epithelial cell polarity, proper spindle orientation as well as cell fate decision accompanied by the loss of asymmetric Numb segregation. In support of this, shRNA mediated depletion of *Numb* in the lung epithelial cell line MLE15 results in an increased expression of the progenitor cell marker *Sox9* and decreased cell differentiation [122]. These pivotal features of Numb, acting as an intrinsic key determinant of asymmetric versus symmetric cell division and defining cell polarity, are upon their impairment also critical for the formation and progression of tumors. There is indeed evidence that Numb and Numblike are implicated in different human tumors, such as breast cancer [109, 126] or non-small-cell lung carcinomas (NSCLCs) [114, 127]. At this juncture, tumorigenesis has generally been correlated with a loss of Numb expression and consequent activation of oncogenic Notch-signaling as well as attenuation of p53 tumor suppressor pathway [109, 128]. Moreover, loss of Numb abundance has also been described in brain tumorigenesis, where hedgehog signaling

is consequently hyperactivated promoting tumor growth [106]. In contrast, Numblike usually shows overexpression and mislocalization in tumor cells, which correlates with a loss of tumor suppressive *micro RNA 296* (*miR-296*) that negatively regulates Numblike in normal cells [114]. In lung carcinomas (NSCLCs) Numblike and the stem cell specific transcription factor Klf4 might act synergistically in maintaining progenitor-like cell populations [114]. Taken together, these results show clear correlations between Numb/Numblike expression, their control of cell polarity as well as cell fate balance between proliferating progenitor cells and their differentiation for several tissues. Observations in human tumors evidently point out associations of Numb and Numblike deregulation with carcinogenesis but mechanistic insights are superficial, just as explicit actions of Numb and Numblike during lung epithelial development and regeneration are only poorly understood so far.

1.5 Aim of this study

In this study I aimed to investigate the role of Numb and its cytosolic homolog Numblike during murine lung epithelial development as well as their potential impact in lung disease in more detail. Functional characterization of both genes upon their concomitant lung epithelial specific inactivation in mouse should help to pinpoint their importance during epithelial specification, the establishment of cell polarity as well as the maintenance of epithelial integrity and last not least their functions in lung regeneration after injury. To my knowledge there are no existing data describing the role of Numb and Numblike in lung fibrosis, which represents another devastating lung disease besides lung cancer. Using bleomycin to induce experimental lung fibrosis in *Numb/Numblike* double mutant mice, I tried to elucidate potential functions of both proteins in the regulation of fibrosis triggering pathways like Wnt/ß-Catenin signaling. In support of this, I wanted to reveal novel mechanisms that might help to explain the establishment and maintenance of epithelial integrity and cell polarity, as Numb and Numblike have recently been involved in such processes. The performance of interactome analysis for both proteins by mass spectrometry, validation of novel potential interaction partner as well as shRNA-mediated silencing of *Numb* and *Numblike* in lung epithelial cell lines are aspired to provide advanced mechanistic insights.

2 MATERIAL AND METHODS

2.1 Transgenic mice

The animal experiments in this work were done according to the regulations issued by the Committee for Animal Rights Protection of the State of Hessen (Regierungs-pärsidium Darmstadt) or the Instituto de Investigacion en Biomedicina de Buenos Aires (IBioBA)-CONICET-Partner Institute of the Max Planck Society (C1425FQD Buenos Aires, Argentina). The animals were kept under sterile approved animal facility conditions with an appropriate day and night cycle.

2.1.1 Numb//Numblike

Mice containing homozygous *Numb*-floxed alleles (*Numb*$^{fl/fl}$) were kindly provided and originally generated by Zilian, O., et al. (2001) [129]. These animals were crossed with mice containing a Numblike null allele (*Numblike*$^{+/-}$), lacking 90% of the coding region (originally from Petersen, P. H., et al. (2002) [118]). Females homozygous for Numblike null are infertile. In order to obtain double homozygous Numb/Numblike mutants we mated *Numb*$^{fl/fl}$*//Numblike*$^{-/-}$ males with *Numb*$^{fl/fl}$*//Numblike*$^{+/-}$ females.

2.1.2 SPCrtTA//tetOCre

The doxycycline inducible lung epithelial specific Cre line used for our studies was originally generated by Perl, A. K., et al. (2002) [130]. These mice express the rtTA activator under control of the human *SPC* promoter. Gene expression is exclusively directed to the developing and mature lung epithelium in epithelial cells of primordial lung buds, with maintenance of expression in alveolar and bronchiolar epithelial cells after birth [131, 132]. These transgenic *SPCrtTA* mice were previously crossed to the transgenic (*tetO*)$_7$*-Cre* (*tetOCre*) line to obtain the transgenic doxycycline inducible *SPCrtTA//tetOCre* animals. This line was always kept heterozygous.

2.1.3 SPCrtTA//tetOCre//Numb//Numblike

This transgenic line was generated in crossing *SPCrtTA*$^{+/-}$*//tetOCre*$^{+/-}$ mice either with *Numb*$^{fl/fl}$*//Numblike*$^{-/-}$ males or vice versa with *Numb*$^{fl/fl}$*//Numblike*$^{+/-}$ females to obtain double mutants. Upon doxycycline application (Dox; Doxycycline hyclate; # D9891-25G – Sigma) in the drinking water of the animals the floxed *Numb* alleles are recombined by the activated Cre generating the inactivation of *Numb* on a *Numblike* deficient background later on referred to as dKO.

2.1.4 SPCrtTA//tetOCre//Numb//Numblike//RosaYFP

This reporter line was generated the same way as in 2.1.3 including breeding to the *Rosa26-Stopflox-eYFP* reporter line (The Jackson Laboratory). This reporter line was crossed in for the purpose of lineage tracing, monitoring Cre activity or FACS sorting of epithelial cells. As wild type control mice we especially crossed *SPCrtTA//tetOCre* animals with *Rosa26-Stopflox-eYFP* mice obtaining mice with Numb/Numblike in their wild type state. These mice are later on referred to as WtCtrl.

2.2 Genotyping of mice

2.2.1 Mouse tail biopsies and extraction of tail DNA

The preparation of mouse-tail biopsies (tailing) was done by the local animal-caretakers in the animal facilities under appropriate conditions. After obtaining the tails the samples were digested in 500 µl TENS-Buffer (Table 23) with Proteinase K (500 mg Proteinase K - Roth) over night at 56°C. After complete digestion of the tails each sample is centrifuged at 14000 rpm in a table centrifuge (Centrifuge 5417R, Centrifuge 5430 - Eppendorf), the supernatant is collected in a fresh tube, and the DNA precipitated by adding 500µl Isopropanol. After another centrifugation step (14000 rpm) DNA gets pelleted and can be washed 1x with 70 % Ethanol (EtOH). Finally the dried DNA pellet is resuspended in 300 µl TE-Buffer (Table 24) or Milli-Q H_2O (Milli-Q® Advantage A10 System – Millipore) 3h at 56 °C. The tail DNA is then ready to use for genotyping.

2.2.2 Polymerase Chain Reaction (PCR)

To genotype the different mouse strains we performed PCR on extracted genomic tail DNA (2.2.1) using corresponding primer combinations (2.2.3 Primer by Sigma-Aldrich) either with the Sigma REDTaq® DNA Polymerase mix (D4309) or a homemade Taq-mix (Table 3; Table 4). PCR was performed in a Thermocycler (Mastercycler Nexus – Eppendorf, Labcycler – Sensoquest) at a cycle program corresponding to the PCR (2.2.3). The PCR products were loaded on a 1 – 2% agarose gel (LE Agarose, #840004 – Biozym) and separated in 1x TAE (Tris-acetate-EDTA) buffer (Table 16) at 100 – 180 mV (Power Supply: E455 – Consort, Power Pack P25 T – Biometra, T100 Thermal Cycler – Biorad). Gel documentation was performed with a UV gel documentation device (BioDocAnalyze - Biometra).

Homemade-Taq-Mix	25µl Mix
dNTPs	0.5µl
10x Taq-Buffer with $MgCl_2$	2.5µl
Primer 5’	1µl
Primer 3’	1µl
Homemade-Taq	0.25µl
Milli-Q-H_2O	18.75µl
Template DNA	1µl

Table 3: Homemade-Taq-Mix

REDTaq® DNA Polymerase Mix	23µl Mix
Primer 5’	0.5µl
Primer 3’	0.5µl
REDTaq® DNA Polymerase Mix	8µl
Milli-Q-H_2O	13µl
Template DNA	1µl

Table 4: REDTaq® DNA Polymerase Mix

2.2.3 Primers and PCR programs

SPCrtTA	Homemade-Taq-Mix	
Primer 5’	GACACA TATAAGACCCTGGTCA	
Primer 3’	AAAATCTTGCCAGCTTTCCCC	
Program (35 cycles)	94°C	3:00 min
	94°C	0:30 min
	58°C	0:30 min
	72°C	0:30 min
	72°C	5:00 min
	12°C	Hold

Expected size	340bp

Table 5: SPCrtTA PCR

CMV-Cre	Homemade-Taq-Mix	
Primer 5’	GACCAGGTTCGTTCACTCATGG	
Primer 3’	AGGCTAAGTGCCTTCTCTACAC	
Program (39 cycles)	94°C	3:00 min
	94°C	0:30 min
	61°C	0:30 min
	72°C	0:30 min
	72°C	5:00 min
	12°C	Hold
Expected size	218bp	

Table 6: CMV-Cre PCR

Numb	Homemade-Taq-Mix	
Primer 5’	GAA GGA GCC TTC CAA AAT CGT ATT C	
Primer 3’	TAA GGG CTA CAG AGT AAG TTC AAG GAC AG	
Program (36cycles)	94°C	3:00 min
	94°C	0:30 min
	53°C	0:30 min
	72°C	0:30 min
	72°C	5:00 min
	12°C	Hold
Expected size	Wt 341bp, Mut 360bp	

Table 7: Numb PCR

Numblike	Homemade-Taq-Mix
Primer 5’ AS196	CTG TTT CCT GCC TTC CTT CCT AGT C
Primer 3’ AS197	GCA GGC AGT GAA AAA CCA TCT CTC

Primer 3' AS198	CAC TCT GCC ACC TAG CTT CAT GTC	
Program (35cycles)	94°C	3:00 min
	94°C	0:30 min
	62°C	0:30 min
	72°C	0:35 min
	72°C	5:00 min
	12°C	Hold
Expected size	Wt 258bp, Mut 341bp, 3rd band at 500bp (heterozygous)	

Table 8: Numblike PCR

RosaYFP	REDTaq® DNA Polymerase mix	
Primer 5' RosaFA	AAA GTC GCT CTG AGT TGT TAT	
Primer 3' RosaRF	GGA GCG GGA GAA ATG GAT ATG	
Primer 3' RosaSpliAC	CAT CAA GGA AAC CCT GGA CTA CTG	
Program (39cycles)	94°C	3:00 min
	94°C	0:30 min
	57°C	0:30 min
	72°C	0:50 min
	72°C	5:00 min
	12°C	Hold
Expected size	Wt 650bp, Mut 250bp	

Table 9: RosaYFP

SPC-YiCreZ	Homemade-Taq-Mix	
Primer 5'	TACCAGCTCTCAGGTGGCCCT	
Primer 3'	CAGCTCCTCGCCCTTGCTCAC	
Program (36cycles)	94°C	3:00 min
	94°C	0:30 min
	65°C	0:30 min
	72°C	0:30 min

	72°C	5:00 min
	12°C	Hold
Expected size	426bp	

Table 10: SPC-YiCreZ PCR

2.3 Cloning and preparation of plasmid DNA

2.3.1 Transformation of bacteria with plasmid DNA

In order to amplify a DNA fragments or plasmid DNA constructs it is necessary to bring this foreign DNA into bacterial microorganisms. Therefor, we made use of electrocompetent XL1 blue bacterial stocks, which we transformed by electroporation with an electroporator (Gene Pulser™ – Bio-Rad). At first, we diluted a 50µl XL1blue stock with an appropriate amount of pre-cooled sterile H_2O (maximum 500µl) and transferred 100µl of this bacterial dilution to a pre-cooled electroporation cuvette (Electroporation Cuvettes, #71-2020 blue cap – Peqlab). Then, 250 ng – 1µg of DNA was added and the cuvettes were subjected to the electroporator. As transformation control we used sterile H_2O instead of DNA. All previous steps were processed on ice to prevent the bacteria of loosing their electrocompetence. The electroporation was performed at 2.5 kV and poration time was always in a range of 4.6 to 4.7 ms. After that, the electroporated bacteria were resuspended in 400µl of cold LB-medium (LB-Medium (Lennox), #X964.2 - Roth) without antibiotics and pre-incubated at 37°C on a heating block (Thermo Mixer F 1.5 - Eppendorf) for 30 min. The pre-incubated bacteria suspension was finally transferred to an antibiotics containing (50-100 µg e.g. Ampicillin, Amp) agar dish (LB-Agar (Lennox), #X965.2 – Roth), nicely distributed on the dish with a sterile Drigalski scoop and finally the inoculated dish was incubated upside-down in a bacteria incubator (#26126010 – Heraeus) at 37 °C over night.

2.3.2 Preparation of plasmid DNA – Mini-preparation

After bacteria were successfully transformed with the plasmid DNA of interest and formed colonies on the Amp-agar dish, the colonies could be picked with a pipet tip and inoculated in 3 ml of LB-Amp in a glass tube (Mini-preparation). Once the Minis got incubated at 37°C in a bacteria shaker (Innova® 44 Incubator Shaker Series – New Brunswick Scientific) over night, the preparation of the Mini-DNA was performed.

First, 1.5 ml of over night grown bacterial suspension was transferred to a 1.5 ml reaction tube and centrifuged at 14000 x rpm for 1 min to pellet the bacteria. After supernatant was removed the bacterial pellet was resuspended in 200 µl of cold Buffer I (Table 20). Then, 200µl of Buffer II (Table 21) was added, samples were inverted several times and incubated at RT for 5 min. After incubation, 200 µl cold Buffer III (Table 22) was added and the samples were vortexed well. The vortexed samples were then centrifuged at 4 °C, 14000 x rpm for 5 min and the supernatant was carefully transferred with a pipet to a fresh 1.5 ml reaction tube. 400 µl of Isopropanol was added to each sample and the tubes were inverted to precipitate the DNA. Samples were then again centrifuged at 14000 x rpm for 5 min at RT. Once the supernatant was removed the pelleted DNA was washed with 500 µl of 70 % EtOH and the samples were centrifuged once more for 5 min at RT and 14000 x rpm. After the washing step, the DNA pellet was dried at RT and then got resuspended in 100 µl of TE-Buffer (Table 24) supplemented with 10 µg of RNaseA. Finally, the isolated DNA was usually validated by restriction enzyme digest, which was controlled on a 1% agarose gel, and additionally sequenced with corresponding primer.

2.3.3 Preparation of plasmid DNA – Maxi-preparation

In order to obtain larger quantities of plasmid DNA we performed Maxi-preparation with a purchased plasmid DNA purification kit (NucleoBond® Xtra Maxi, #740.414.100 – Macherey-Nagel). Therefor, we first inoculated transformed bacteria either directly from bacterial suspensions of a previously performed Mini-preparation or by inoculating a single bacterial colony grown on an agar dish in 250 ml of LB-medium in a glass flask with an appropriate antibiotic (e.g. Amp). The inoculated LB-medium was incubated and shaken over night at 37 °C in a bacterial incubator. The next day, the over night grown bacterial culture suspension was centrifuged at 5000 x g for 15 min at 4 °C in an ultra centrifuge (Sorvall® RC 5B Plus or Sorvall® Evolution RC #72811 – Thermo Scientific) and the bacterial pellet was further processed as described by the manufacturers protocol (NucleoBond® Xtra Maxi). After the DNA pellet was washed twice with 70 % EtOH and dried we resuspended the pellet in minimum 100 µl of TE-Buffer (Table 24). The DNA purity and concentration was measured in a spectrophotometer (NanoDrop 2000c - Peqlab).

2.4 Cell culture

2.4.1 Mouse lung epithelial cells (MLE12)

In vitro studies were mainly performed with the mouse lung epithelial cell line (MLE12). The cells were cultured in Dulbecco's Modification of Eagle's Medium (D-MEM/F-12 (1:1) (1X); #21331-046 – Gibco) supplemented with 10% Fetal Calf Serum (FCS, #F7524 – Sigma) and 1% Penicillin/ Streptomycin/ Glutamin (P/S/G 100x, #G1146 – Sigma). To keep the cells in culture for longer time they were passaged twice a week, depending on their density. Therefor the used culture media was removed from the dish first. Then cells were washed once with sterile 1x PBS pH7.4 (phosphate buffered saline, Table 18; 10ml per 10 cm dish) and trypsinized with 1x Trypsin/EDTA (10x T/E, #59418C – Sigma; Table 19) to detach the cells from the culture dish. To obtain a single cell suspension culture media was added to stop trypsination and cells were resuspended nicely with a glass pipet. Finally, cells were seeded in a low density to a fresh cell culture dish (ratio 1:5 – 1:10 per 10 cm dish; Cellstar® #664160 – Greiner Bio-One) and kept at humidified conditions (37°C/ 5% CO_2) in an incubator (Heracell 150i – ThermoFisher Scientific). All cell culture work was done at a sterile hood (HeraSafe KS – ThermoFisher Scientific) at either safety level 1 or 2 (S1, S2) facilities.

2.4.2 Human Embryonic Kidney Cells (HEK293T)

Human Embryonic Kidney Cells (HEK293T) cells were cultured in DMEM/10% FCS/1% PSG (1 x Dulbecco's Modified Eagle Medium (DMEM 4.5 g/L D-Glucose, #42430-025 – Gibco). The cells were passaged every 2nd day and used as packaging cells to produce lenti-virus containing shRNA for the generation of knockdown cells (2.4.4). The cells were kept at humidified conditions (37°C/ 5% CO_2). Stocks were prepared in 90% FCS/ 10% DMSO (Dimethyl sulfoxide, #D4540-100ML - Sigma) and frozen and stored at -80°C (in a styrofoam box).

2.4.3 Transient transfection of cell lines with Calcium-Phosphate

Cultivated HEK293T cells were passaged one day in advance or the same day of transfection to grow to a density of about 70% of the culture dish (amounts according to a 6-well-plate: Cellstar® #657160 – Greiner Bio-One). Two aliquots A and B were prepared for transfection in advance. Aliquot A contains 5µg DNA and 30.5 µl 2M

$CaCl_2$ filled up to 250 µl with sterile H_2O. Shortly before performing the transfection aliquot A is applied drop wise to 250 µl of 2x HBS (Aliquot B), mixed once with the pipet and added drop wise to the media of the cultured HEK293T. The cells are incubated and kept at humidified conditions at 37°C/ 5% CO_2 in a cell culture incubator.

2.4.4 Generation of stable shNumb/shNumblike RNA silenced MLE12 cells

MLE12 cells were virally transduced using small hairpin RNA against *Numb* and *Numblike* (shNb/shNbL) that are generated on a *pLKO.1-puro* vector backbone (Table 11). As packaging and lentivirus producing cells, HEK293T were cultured in DMEM/10% FCS/1% PSG and co-transfected with the corresponding shRNA vectors, *psPAX2* packaging vector and *pMD2.G* envelope vector (Table 11). As controls we used *pLKO.1-puro-Scrambled* (shScr), as well as *pLKO.1-GFP* (transfection efficiency control). The used vector DNA was obtained in using methods described in 2.3. The target cells (MLE12) were then infected with the lentivirus containing culture media of the transfected, virus producing HEK293T cells. To obtain stably transduced knockdown (kd) cells, MLE12 cells were cultured in puromycin (# -) supplemented (5 µg/ml) culture media (D-MEM/F-12 (1:1) (1X)/10% FCS/ 1% PSG/ Puro), selecting for successfully transduced cells for several passages. Cryo-stocks of stably transduced shNb/shNbL and shScr MLE12 cells were prepared in 90% FCS/10% DMSO and frozen in -80°C.

Plasmid	Description	Source
pLKO.1-puro (SHC001)	MISSION® TRC lentiviral control vector with puromycin resistance gene.	Sigma-Aldrich Chemie GmbH, Steinheim
pLKO.1-GFP	MISSION® TRC lentiviral control vector for expression of a green fluorescence protein (GFP). This vector contains no puromycin resistance gene.	Sigma-Aldrich Chemie GmbH, Steinheim
pLKO.1-puro-Scrambled shRNA	MISSION® TRC lentiviral control vector with puromycin resistance for the expression	Sigma-Aldrich Chemie GmbH,

	of a shRNA, that doesn't match and interfere with a known mouse or human gene.	Steinheim
pLKO.1-puro-Numb shRNA (NM_010949)	Set of five different MISSION® TRC lentiviral vector with puromycin resistance for the expression of shRNA against mouse *Numb.*	Sigma-Aldrich Chemie GmbH, Steinheim
pLKO.1-puro-Numblike shRNA (NM_010950)	Set of five different MISSION® TRC lentiviral vector with puromycin resistance for the expression of shRNA against mouse *Numblike.*	Sigma-Aldrich Chemie GmbH, Steinheim
psPAX2	Plasmid for the expression of the packaging genes *gag*, *pol* and *rev* for the production of lentivirus.	Sigma-Aldrich Chemie GmbH, Steinheim
pMD2.G	Plasmid for the expression of the viral envelope proteins VSV-G for the production of lentivirus.	Sigma-Aldrich Chemie GmbH, Steinheim

Table 11: List of plasmids/ shRNA

2.4.5 Generation of stable Numb and Numblike overexpressing MLE12 cells

MLE12 cells that stably express one of the four human Numb isoforms or Numblike N-terminally fused to GFP (Numb1-4:GFP, Numblike:GFP) as well as GFP expressing control MLE12 cells (GFP Ctrl) were kindly generated and provided by Dr. André Görgens (Group Bernd Giebel, University of Duisburg-Essen). Originally, the Numb expression plasmids were provided by Verdi et *al.* [100] and the coding regions of all isoforms were cloned into the lentiviral transfer vector pCL6-EG-wo as described by Dr. André Görgens (Funktionelle Analyse von Numb und Redefinition der humanen hämatopoetischen Hierarchie - 2012). These vectors where then used for the production of lentiviral particles in HEK293T cells followed by the transduction of MLE12 cells with the produced lentiviral supernatants. The transduced MLE12 cells were FACS sorted for GFP positive cells in order to obtain purified cell lines that stably overexpress the different GFP fusion proteins.

2.4.6 GSK3-ß inhibition experiments (WNT/ß-Catenin signaling)

MLE12 kd cells were seeded on a 6-well-plate (#657160 – Greiner Bio-One) at a density of 5 x 10^5 cells/ well the night before performing the treatment. The cells were then treated with 20 mM LiCl (4M Lithiumchlorid stock in H_2O, at 4°C, powder: #P007.1 - Roth) and 30 µM SB216763 (10 mM stock in DMSO, at -20°C, #ab120202 – Abcam) to inhibit GSK3ß-activity. Furthermore, cells were treated with 10 µM MG132 (10 mM stock in DMSO, at -20°C, #474791 – Calbiochem) to totally block proteosomal degradation (positive control). DMSO (0.3 %) treated and untreated cells were used as negative controls. The incubation time for the treatment was 2 to 4h at 37°C/ 5% CO_2.

2.4.7 Cultivation of primary mouse lung epithelial cells

Isolated, FACS sorted primary lung epithelial cells were plated on a 4-well chamber slide (Lab Tek® Chamber Slide™ system, 4-well Permanox® Slide, #177437 Nunc/ Sigma-Aldrich) and coated either with fibronectin (FN; #C-43050 – PromoCell; 10µl FN/ 1ml 1x PBS; coating 30-60 min at RT) or matrigel (MG; # - ; 1:50 in D-MEM/F-12 (1:1) (1X)/10% FCS/ 1% PSG; coating 2h at RT). Cells were seeded at a density of 3.0 – 5.0 x 10^4 cells/ well and kept at humidified conditions at 37°C/ 5% CO_2.

2.5 Isolation of primary lung epithelial cells and FACS sorting

2.5.1 Isolation of primary lung epithelial cells

Narcotized animals (1:1:1; Ketamin 10% – Medistar, Xylariem® (20mg Xylazin) – Ecuphar, 0.9 % NaCl – B Braun) were nicely perfused with 1x PBS via the right ventricle to get lungs blood free and primary lung epithelial cells were isolated as previously described [133] using a slightly modified procedure. After perfusion the lungs were filled up with 1 ml of dispase (#354235 – Corning) and the trachea was ligated to keep the dispase in the lung. After isolation of the filled lung it was minced into small pieces in a petri dish with a scissor. Lung pieces were transferred with additional 1 ml of dispase to a 50 ml Falcon tube (Cellstar® Tubes #227261 – Greiner Bio-One) and kept on ice until all samples were prepared. 20µg DNaseI (10mg/ml – 20U/ml; #) was added to the lung/dispase suspension (2 ml) followed by digestion of the samples on a shaker at 37°C for 45 min. After digestion of the lung pieces, the

suspension was resuspended with a plastic pipet (Cellstar® #607180/10ml, #606180/5ml – Greiner Bio-One) and passed via a 100µm and a 40µm strainer (EASYstrainer™ 100µm, #542000; 40 µm #542040 – Greiner-Bio-One) to obtain a primary lung cell homogenate (filters were flushed at each step with D-MEM/F-12 (1:1) (1X)/10% FCS). The homogenates were centrifuged for 10 min at 1200 rpm (300 x g) and the supernatant was carefully removed. The cell pellet was resuspended in 1 ml of precooled FACS sorting buffer (Table 37) and then passed through the filter of a FACS sorting tube (40 µm FALCON®, #352235 – Corning) to get a single cell suspension that was subjected to the FACS sorter.

2.5.2 FACS sorting of YFP$^+$ lung epithelial cells

Single cell suspensions derived from isolated primary lung epithelial cells (2.5.1) of SPCrtTA// Cre// Numb// Numblike// RosaYFP mutant and littermate control mice (treated with doxycycline) were subjected to the FACS sorter (BD FACSAria III Cell Sorter) in a FACS tube. Samples were nicely resuspended in FACS sorting buffer together with DAPI to exclude dead cells during sorting. FACS sorter was gated for both YFP$^+$ single cell events (doublet exclusion of FITC high positive events) and negative events (FITC low positive events) as control fraction. Both fractions were collected in a 15 ml Falcon tube (coated and filled with 4 ml D-MEM/F-12 (1:1) (1X)/10% FCS) and either seeded for cell culture (2.4.7) or resuspended in 1 ml of peqGOLD® TriFast for RNA preparation (2.6.1).

2.6 RNA preparation and cDNA synthesis

2.6.1 RNA preparation with peqGOLD® TriFast™ reagent

In order to isolate RNA of mouse tissue, e.g. mouse lung, organs were isolated from the animal, snap frozen in liquid nitrogen, and either stored at -80°C or directly resuspended in 1ml of peqGOLD® TriFast™ (#30-2010 – Peqlab) reagent, with the help of sterile metal beads (grinding balls ss 5 mm, #22.455.0003 – Retsch) in a tissue homogenizer (Retsch MM301). Cells that were grown in cell culture were first washed with 1x PBS and then 1ml of peqGOLD® TriFast™ was added directly to the dish. The cell samples were harvested with a cell scraper (#83.1830 - Sarstedt), transferred to a fresh tube and resuspended with a pipet. After homogenization of the samples in peqGOLD® TriFast™ they were incubated 5 min at room temperature (RT), 200µl Chloroform (#6340.2 - Roth) was added and the samples mixed well.

Once the samples were incubated again for 5 min at RT they were centrifuged at 12000 rcf (4°C) to perform a phase separation. The upper aqueous phase was transferred to a fresh tube (the residual inter- and organic phase were kept at 4°C for protein extraction; 2.8). Isopropanol was added to precipitate the RNA (10 min on ice). After centrifugation (12000 rcf, 4°C, 10 min) the RNA pellet was washed 2 times with 75% EtOH. Finally, the dried pellet was resuspended in 20-60µl of RNase free H_2O and used for cDNA synthesis (storage of RNA at -80°C).

2.6.2 cDNA synthesis

In order to perform relative quantitation of RNA expression levels cDNA was synthesized. Therefor RNA concentration of the purified RNA samples were measured (NanoDrop ND-2000c Spektralphotometer - Peqlab) and 0.5 – 2µg of RNA were used for the synthesis (Table 12). After cDNA was synthesized it was diluted 1:100 with Milli-Q H_2O for the use in TaqMan® Gene Expression Assays (Applied Biosystems) to determine relative RNA expression levels quantitatively (2.7).

Reagents/Steps	cDNA synthesis mix (total 20µl)	
dNTPs (#R0186 – Fermentas)	1µl	
Oligo(dt)15 Primer (#C1101 – Promega)	1µl	
RNA (0.5 – 2µg) xµl	10-x	
RNase free H_2O	Add to 12µl	
Step 1 (12µl mix)	65°C	5 min
	4°C	Hold
Add synthesis mix:	At 4°C	
5x FS buffer (*)	4µl	
0.1M DTT (*)	2µl	
RNasin Plus (#N2615 – Promega)	1µl	
SSII RT (* #18064071 – Invitrogen)	1µl	

Step 2 (20µl mix)	42°C	50 min
	70°C	15 min
	4°C	Hold

Table 12: cDNA synthesis

2.7 Real-Time PCR (qPCR)

The quantitation of RNA expression levels was performed in using TaqMan® Gene Expression Assays for the corresponding targets (FAM Dye; Table 13) versus an endogenous loading control e.g. *Gapdh* or *Hprt* that are designed with a different dye than the targets (VIC Dye). The quantitation was done by a qPCR thermocycler (Step OnePlus Real-Time PCR System – Applied Biosystems) that calculated fold changes (RQ-values) of the examined samples based on their ddCT values with the step one software (StepOne™ Software v2.3).

Target name	TaqMan® Gene Expression Assay
Numb	Mm01302750_m1
Numb	Mm00477927_m1
Numblike	Mm01171278_m1
Sftpc (SP-C)	Mm00488146_g1
Scgb1a1 (CC-10/CCSP)	Mm01230908_m1
Podoplanin	Mm01348912_g1
Foxj1	Mm01267279_m1
Ascl2	Mm01268891_g1
Col1a1	Mm00801666_g1
Ctgf	Mm01192933_g1
Tnf-alpha	Mm00443258_m1
Acta2	Mm00725412_s1
Wisp1	Mm01200484_m1

FN1	Mm01256744_m1
Mmp2	Mm00439498_m1
Mmp9	Mm00442991_m1
Snai1	Mm00441533_g1
Twist1	Mm00442036_m1
Axin1	Mm01299060_m1
Axin2	Mm00443610_m1
Ctnnb1 (ß-Catenin)	Mm00483039_m1
cMyc	Mm00487804_m1
T2 (Brachyury2)	Mm00496699_m1
Ccnd1 (CyclinD1)	Mm00432359_m1

Table 13: TaqMan® Gene Expression Assays

2.8 Protein extraction and analysis

2.8.1 Preparation of cell/ tissue lysates

In order to analyze protein levels of cultured cells or isolated mouse tissue samples, e.g. lung, the extraction of proteins was either performed in using 5x LB-sample buffer (for cell lines; Table 25) or Extraction buffer (EP; for tissue; Table 26) with a supplementation of protease inhibitors (Table 29) to homogenize the samples. Cultured cells were harvested with a cell scraper after adding 5x LB buffer directly to the dish in a reasonable amount (100 – 150µl per 6-well-plate). After transfer to a fresh tube samples were resuspended and homogenized properly by pipetting and following sonication with a sonicator (00:22 sec/5 cycles/30% power; Bandelin Sono Plus). The protein homogenate was centrifuged (10000 rcf, 5 min, RT). Cleared lysate was then collected in a fresh tube and protein concentration was measured using Bradford method (2.8.2). Samples were diluted in corresponding lysis buffer together with NuPAGE® LDS Sample Buffer (4x) (1:3 dilution of Sample; #NP007 – ThermoFisher Scientific) to obtain ready-to-use protein working solutions (10-30µg/µl) that were denatured by supplementation of 1M DTT (4µl per 100µl sample) and heating up to 95°C (3 min). Mouse tissue samples were treated the same way as

cells after homogenization of the isolated tissue with metal beats in a homogenizer in EP-lysis buffer. Protein that was obtained via peqGOLD® TriFast™ phase separation (2.6.1) was further processed following stringently the manufacturer's protocol (peqGOLD® TriFast™) and finally treated the same way as previously described.

2.8.2 Protein concentration measurement with Bradford

Protein concentration measurements were performed using the Bradford method. Therefor 5µl of protein sample was supplemented with 25µl reagent A (Bio-Rad DC™ Protein Assay Reagent A #500-0113 – Biorad) followed by 200µl reagent B (DC™ Protein Assay Reagent B #500-0114 – Biorad). Samples were incubated 10 min at RT (dark) and then added on a 96-well plate (Microplate, #655101 – Greiner-Bio-One) together with a blank (only lysis buffer) and a BSA protein standard row (BSA dilution series: 1, 5, 10, 20, 30 µg; 100x BSA #B9001S - NEB) to measure the sample absorptions in a photometric plate reader (FluoStar). Samples were all prepared in duplicates. The protein concentrations were calculated based on the standard regression curve in an Excel sheet.

2.8.3 Protein expression analysis by Western Blot

In order to analyze protein levels based on Western Blot the protein samples were first loaded in equal amounts (10 – 30µg per well) on a self-made polyacrylamide gel (e.g. 9% PAA gel (Table 36); filled in a purchased NOVEX® Cassettes 1 mm #NC2010 – Invitrogen) to perform a separation of the proteins by their mass via electrophoresis. The electrophoresis were performed in a gel running chamber (NOVEX® Invitrogen) at separation times between 1.5 – 2h using, depending on the protein size of interest, either 1x MOPS (>50kDa; Table 30) or 1x MES (<50 kDa; Table 31) buffer (Invitrogen). For a better separation and running behavior running buffers were supplemented with 5 mM sodium bisulfite (1M sodium bisulfite). Protein mass could be detected in using Protein-Marker VI (#27-2311 – Peqlab). After separation via gel electrophoresis the proteins were transferred to a nitrocellulose membrane (Amersham™ Protran™ 0.45 µm NC, #10600002 – GE Healthcare) in performing Western Blot. The protein transfer was achieved using 1x Transfer buffer (Table 32) and blotting times of between 2 to 2.5 h at 30 mV (Power Pac 200 – Bio-Rad) in a blotting chamber (NOVEX® XCell II Blot Module – Life Technologies/ Invitrogen). After the protein transfer the membranes were stained with

1x Red Alert (dilution of 10x Red Alert™ Western Blot Stain #71078-50ML – Merck) for 10 min on a shaker (Rotamax120 – Heidolph). The stained membranes were washed with desalted water (until band pattern got clear), cut according to the size of the proteins of interest and blocked in 5% milk powder solution (#70166-500G – Fluka®) in 1x TBS-T (Table 35) for 1h at RT. After blocking the membranes were incubated with the primary antibodies at dilutions noted in Table 14 (either in 5% BSA/TBS-T or 5% milk powder solution in TBS-T; antibodies: Table 14) over night (o.n.) at 4°C.

After incubation with primary antibody membranes were washed thrice with 1x TBS-T (15min – 1h each washing step) and then incubated with the secondary antibody (Table 14) in 5% milk powder/ 1x TBS-T for 2h at RT. Membranes were washed again thrice with 1x TBS-T and then subjected to a chemiluminescence analyzer (ChemiDoc™ MP Imaging System – Bio-Rad) for detection of protein bands using 1:1 femto solution (SuperSignal® West Femto Maximum Sensitivity Substrate #34096 – ThermoFisher Scientific). Densitometry and data analysis was done with Image Lab 5.1 software (Bio-Rad).

2.8.4 Co-Immunoprecipitation with magnetic GFP-Trap®_MA beads

Experiment was executed mostly according to the manufacturers protocol, with slight modifications. GFP-overexpressing MLE12 cells (Numb1-4:GFP; Numblike:GFP) were cultured as described before (2.4.1) 48 h on a 10 cm culture dish. After removal of the culture medium, the cells were washed once with 1 x PBS. Next, 200 µl of freshly prepared RIPA modified lysis buffer (Table 27), supplemented with protease inhibitors (Table 29), was added to the dish, cells were harvested with a cell scraper and the pre-lysate was transferred to pre-cooled 1.5 ml tube. Cell-lysates were placed on ice, incubated for 30 min and resuspended with a pipet every 10 min. In order to obtain pure lysates and to exclude cell debris, the samples were centrifuged at 4°C at a speed of 20000 x g for 10 min. Pure lysates were then transferred to a fresh pre-cooled 1.5 ml tube and diluted with Dilution/Wash buffer (DB/WB; Table 28), including protease inhibitors as well, up to 500 µl in total. For the use of equal amounts of protein inputs (Inp) in each immunoprecipitation (IP) sample, protein concentrations of the lysates were determined with Bradford (2.8.2). A total amount of about 1 mg of protein was applied for each IP, while a residual amount of protein was retained as input (Inp) control of each sample for later comparative analysis by

western blot. For the IP, 25 µl of GFP-Trap®_MA (gtma-20 (500µl) – ChromoTek) bead slurry was equilibrated and washed thrice in cold DB/WB before 1 mg of protein lysate was added. The IP works via anti-GFP V_HH antibodies that are coupled to magnetic agarose beads to precipitate GFP-tagged fusion proteins. Therefor, the protein samples with the beads were incubated on a rolling wheel at 4°C for 1 ½ h. Finally, after supernatant was removed carefully, while beads are separated with the help of a magnetic rack and were washed thrice gently in cold DB/WB (including protease inhibitors), the beads were eluted in 50 µl of 2 x LDS sample buffer/40 mM DTT (1:1 dilution of 4x LDS sample buffer with RIPA modified including protease inhibitors) at 95°C on a 1.5 ml tube shaker at 900 x rpm for 10 min. After elution, the beads were magnetically separated in a magnet stand and eluted IP was transferred to a fresh tube. IP samples were eventually either loaded on a 4-12% Bis-Tris gel (Novex® - NuPAGE 4-12% Bis-Tris Gel, 1.0 mm x 10 well; #NP0321 – Thermo Fisher) and then further processed and subjected to mass spectrometry for protein quantification (2.8.5) or the samples were loaded on a 9 % PAA gel together with inputs to perform PAGE followed by analysis of the co-immunoprecipitated proteins by western blot (2.8.3).

2.8.5 Co-immunoprecipitation with Protein-G Sepharose beads

In order to precipitate proteins with Protein-G Sepharose™ beads (#17-0618-01, 5ml – GE Healthcare) together with an antibody of interest, lysates of GFP-overexpressing MLE12 cells (Numb1-4:GFP; Numblike:GFP), that were cultured as described before (2.4.1) 48 h on a 10 cm culture dish, were prepared as described in 2.8.4. Protein-G Sepharose™ beads slurry (30 µl) was first equilibrated and washed thrice in cold DB/WB and each time centrifuged at a speed of 10000 x g at 4°C for 20 sec. In further, 1 mg of freshly prepared protein lysate was incubated at first with 8 µg of the antibody of interest and additionally a control fraction of lysate was incubated only with normal mouse IgG1-isotype (8 µg) as negative IP control. A residual amount of protein was retained as input (Inp) control of each sample for later comparative analysis by western blot. Incubation of the IP-fractions was performed at 4°C on a rolling wheel for 1 ½ h. After that, precipitated proteins were indirectly coupled via the 1st antibody to Protein-G Sepharose™ beads. Therefor, whole IP fraction was transferred to the pre-washed beads and incubated for another hour at 4°C on a rolling wheel. Finally, beads were washed thrice gently in cold DB/WB (including protease

inhibitors). The beads were eluted in 50 µl of 2 x LDS sample buffer/40 mM DTT (1:1 dilution of 4x LDS sample buffer with RIPA modified including protease inhibitors) at 95°C on a 1.5 ml tube shaker at 900 x rpm for 10 min. Finally, beads with the coupled precipitates were washed thrice gently in cold DB/WB (including protease inhibitors). The beads were then eluted in 50 µl of 2 x LDS sample buffer/ 40 mM DTT (1:1 dilution of 4x LDS sample buffer with RIPA modified including protease inhibitors) at 95°C on a 1.5 ml tube shaker at 900 x rpm for 10 min. After elution, the beads were separated by centrifugation at a speed of 10000 x g and 4°C for 20 sec and the supernatant containing the eluted precipitates carefully transferred to a fresh tube. IP samples were eventually either loaded on a 4-12% Bis-Tris gel (Novex® - NuPAGE 4-12% Bis-Tris Gel, 1.0 mm x 10 well; #NP0321 – Thermo Fisher) and then further processed and subjected to mass spectrometry for protein quantification (2.9) or the samples were loaded on a 9 % PAA gel together with inputs to perform PAGE (polyacrylamide gel electrophoresis) followed by analysis of the co-immunoprecipitated proteins by western blot (2.8.3).

2.9 Mass spectrometry analysis

In order to measure and quantify proteins and potential novel interaction partners of immunoprecipitated proteins, that were processed as described in 2.8.4 or 2.8.5, we made use of the following methods. These were mainly performed and executed by the mass spectrometry facility of the Max Planck Institute Bad Nauheim headed by Dr. Ansgar Pötsch, formerly by Dr. Marcus Krüger.

2.9.1 In-gel digestion

Protein samples were separated according to their molecular weight by SDS-PAGE (Novex® - NuPAGE 4-12% Bis-Tris Gel, 1.0 mm x 10 well; #NP0321 – Thermo Fisher) followed by Instant Blue Staining (Instant Blue, Expedeon) for 15 minutes on a shaker. Then, gel was washed twice with distilled water. Protein gels were either stored at 4°C in destilled water or directly further processed by cutting the single lanes into cubic pieces of similar size and subsequently digested in gel as described by Shevchenko et al. [134]. Therefore, gel pieces were first decolored by incubating twice with 100 µl of 50 mM ammonium bicarbonate (ABC) solution for 20 min. Next, the gel pieces were dehydrated by incubating twice with 100 µl ethanol for 10 min and dried in a SpeedVac (Concentrator plus, Eppendorf) for 5 min at 30°C. In

following, protein samples were reduced with 10 mM dithiothreitol (DTT) at 56°C for 45 min under constant shaking at 600 rpm in a Thermomixer. After this, proteins were alkylated with 55 mM iodoacetamide (IAA) in the dark for 30 minutes. In order to wash the gel pieces 100 µl 50 mM ABC was added and incubated for 15 min. Then, pieces were dehydrated with 100 µl ethanol for 15 min and again washed with 100 µl 50 mM ABC for 15 min. Final dehydration was performed twice with 100 µl ethanol for 15 min. The dehydrated gel pieces were dried in a SpeedVac for 5 min at 30°C and subsequently 40 µl 12ng/µl LysC (WAKO) or trypsin (Promega) was added. The gel pieces were incubated on ice for 15 min until they swelled, 50 mM ABC was added until the gel pieces were fully covered and everything was finally incubated at 37°C overnight for digestion of the proteins. The next day, digested peptides were extracted by increasing acetonitrile (ACN) concentrations. Therefore, enzymatic digestion of proteins in the gel pieces was stopped by incubation with 100 µl 30% ACN / 3% trifluoroacetic acid (TFA) for 20 minutes. In following, the pieces were incubated twice with 100 µl 70% ACN for 20 min and then twice with 100 µl 100% ACN for 20 min, while the peptide solution was collected after each of the incubation steps. Finally, the collected peptide solutions were concentrated in a SpeedVac to about 80 µl and additional 80 µl Buffer C (5% ACN, 1% TFA) was added before the samples were desalted by performing the stop and go extraction (STAGE) technique on STAGE Tips [135]. These were prepared in advance (self-made) by stacking two layers of C18 material in pipette tips. To bring the extracted peptide solutions on the C18 material, STAGE Tips were first activated with 20 µl 100% methanol, washed with Buffer B (80% ACN, 0.1% formic acid) in order to elute any dirt from the C18 material and eventually twice with Buffer A (0.1% formic acid) to remove any remaining acetonitrile from Buffer B. For these equilibration steps the wash buffers were removed from the C18 material by centrifugation at RT and a speed of 2600 rpm for 2min each. After the STAGE Tips were equilibrated, digested peptide solutions were loaded on the C18 material. All samples were then centrifuged at 2600 rpm and RT for 4 min to bind the peptides to the C18 material. At last, STAGE Tips were washed with 20 µl Buffer A, dried with a syringe and stored at 4°C until they were measurement in the mass spectrometer.

2.9.2 Acquisition of mass spectra

Peptides that were processed and loaded to the C18 material of STAGE Tips as described above (2.9.1) were eluted and separated during reversed phase liquid chromatography (LC) on an Easy nano-flow UHPLC system (Thermo Fisher Scientific). In order to perform mass analysis and quantification of the eluted peptides by Tandem Mass Spectrometry (MS/MS) the UHPLC system is connected to the Q Exactive or Q Exactive Plus mass spectrometer via a nano electrospray ionization source.

2.9.3 Analysis of data

The acquired raw data were processed using the MaxQuant software versions 1.3.7.4 to 1.5.2.8 as well as the implemented Andromeda search engine. In order to perform protein identification MS/MS spectra were correlated and compared to the latest Uniprot mouse (Mus musculus) data, which involves 74,265 protein sequence entries. For the purpose of filtering and exclusion of contaminants an additional list of common contaminants was used. Perseus (version 1.4.1.3) and R package was used for following data analysis and visualization as well as the statistical environment R. Proteins were characterized by quantitative co-enrichment in the IP compared to their intensity profiles across triplicates. In order to obtain quantitative protein ratios, the normalized intensities of enriched proteins for the baits were compared to the normalized intensities of proteins that were detected in lysates of controls. A significance line for potential interacting proteins was calculated by Perseus software with $p < 0.05$ and additionally a *fold change* cut-off was set to FC > 2. Proteins below this threshold were either background binding proteins or false positives.

2.10 Histology

2.10.1 Preparation of mouse lung for paraffin and cryosections

Mice were narcotized and perfused with 1x PBS via the right heart ventricle. Perfused lungs were then fixed with 4% Paraformaldehyd (PFA, #0335.4 – Roth) for 5 min at RT via the vasculature (right ventricle), inflated with 4% PFA via the trachea and ligated to keep the lungs expanded. Perfusions and filling were done with a perfusion stand and pressure was adjusted to 10 cm water column not to harm structures. The inflated lobes were then isolated and fixed in 4% PFA for 2h at 4°C. After fixation

lungs were nicely washed thrice with 1x PBS and for Tissue-Tek® O.C.T™ embedding (Tissue-Tek® O.C.T™, #4583 - Sakura) then incubated in 30% sucrose at 4°C o.n. . After sucrose incubation the lungs were inflated with Tissue-Tek®, then embedded in a Tissue-Tek® filled cryo-mold (Tissue-Tek® Cryomold® #4565 – Sakura or Peel-A-Way® Disposable Embedding Molds #677352 – Polysciences Inc.) on dry ice and frozen at -80°C for later cryo sections. Cryosections were performed in a cryotome (Leica CM1950) and sections transferred consecutively (2-3 lung sections on one slide) on a glass slide (Superfrost Ultra Plus®; #J3800AMNZ – Thermo Scientific) at a thickness of 5 µm. Slides were either used directly for histological staining or stored at -80°C. For paraffin sections PBS washed lungs were further processed in a dehydration series of 70% EtOH (o.n. at 4°C or for 2 h on a shaker at RT), 80% EtOH, 90% EtOH, 100% EtOH (Rothipuran® Ethanol > 99.8 % (EtOH); #9065.4 - Roth) for 2h on a shaker at RT each step. Lung samples were then incubated in 100% isopropanol (2h or o.n. on a shaker, RT) and after that transferred to 1:1 isopropanol/paraffin mix at 65°C for several hours (min. 2h). Finally the lungs were transferred to 100% paraffin at 65°C o.n. and before embedding in molds they were subjected to a vacuum oven at 65°C to better penetrate the tissue with paraffin and to get rid of residual air in the lung lumen. The sections were performed with a microtome (Leica RM2265) at 5 – 10 µm and collected on a glass slide (Superfrost Ultra Plus®; #J3800AMNZ – Thermo Scientific). Sections were dried on a heating plate (42°C; HI1220 – Leica) and stored in a box at RT.

2.10.2 HE-staining

Paraffin sections were first deparaffinized (2 x xylene, 5 min; Xylene > 98 % #9713.3 – Roth) and then rehydrated in a decreasing EtOH row (100%, 90%, 80%, 70%) and finally dipped in ddH_2O. At -80°C stored cryosections were thawed and dried for 30 min at RT and then rinsed with ddH_2O for 5 min (shaker) to remove Tissue Tec. After washing the slides were transferred to Mayer's hematoxylin (Haemalum, acidic #2E-038 – Waldeck) and incubated 10 min at RT to stain the nuclei. Subsequently, the sections were cleared 10 min in running tap water then dipped 10 times in 2% HCL/70% EtOH followed by 2 times in ddH_2O. After that the slides were incubated in eosine (Eosine Solution, #2C-140 – Waldeck) for 7 min. After the eosin staining the slides were dehydrated again in an increasing EtOH series (70%, 80%, 90%, 96% - 2 dips each, 100% EtOH 5 min). Finally sections were fixed in xylene (twice 5 min)

and mounted with Entellan (Entellan®, #107960, Merck). Images were acquired with a Keyence microscope (Keyence BZ-9000) or Zeiss Axioplan 2 microscope.

2.10.3 Trichrome staining

Paraffin sections were first deparaffinized and rehydrated (2.10.2). Cryosections were thawed and cleaned of Tissue Tec (2.10.2). The sections were stained using the Masson-Trichrome kit (HT15, Sigma). Both paraffin and cryosections were then processed the same way. After the sections were washed they were incubated at 56 °C for 15 min in preheated Bouin's solution. The slides were then first rinsed in running tap water for 20-25 min and shortly dipped in ddH_2O. Subsequently, sections were incubated 5 min in Mayer's hematoxylin (Haemalum) to stain the nuclei followed by 5 min in Biebrich Scarlet-Acid Fuchsin solution, 5 min in working Phosphotungstic/ Phosphomolybdic acid/ddH_2O solution (1:1:2), 5 min in Anilin Blue solution and finally 2 min in acetic acid 1%. Between each step the slides were rinsed in running tap water for 5 minutes followed by a short dip in ddH_2O. The sections were then dehydrated again in an increasing EtOH series (90% EtOH for 2 sec, 96% EtOH for 2 sec, twice 2 min in 100% EtOH). Finally the sections were fixed twice in xylene for 10 min each and subsequently mounted with Entellan (Entellan®, #107960, Merck). Images were acquired with a Keyence BZ-9000 or Zeiss Axioplan 2 microscope.

2.10.4 Immunofluorescence analysis

In order to examine subcellular protein localizations and abundance we made use of immunofluorescence labeling of fixed cultured cells and tissue sections. Therefor we used a standard antibody staining protocol as described in the data sheet of the antibodies (Table 14). It was adjusted depending on the examined cells or tissues. For the purpose of immunocytochemistry we first washed (1 x PBS) and fixed (4% PFA, 1-5 min, RT) cells that were either cultured on cover slips (cover slips 13 mm, #41001113 – Hecht-Assistent) or chamber slides (Lab Tek® Chamber Slide™ system, 4-well Permanox® Slide, #177437 Nunc/Sigma-Aldrich). After that, cells were permeabilized (0.1 – 0.3% Triton X100, #6683.1 – Roth) and blocked with a blocking solution containing 1% bovine serum albumin (30% BSA, #A7284-500ML – Sigma-Aldrich), 5% normal goat serum (NGS, #16210-064 – Gibco), 0.1% Triton X100 in 1x PBS. Subsequently, the blocked cells were incubated with the appropriate primary antibody (Table 14) in blocking solution in a humidified chamber o.n. at 4°C. Cells

on cover slips were incubated upside-down in a drop of antibody/blocking solution (25 µl) on a strip of parafilm (Parafilm® 'M' #P7793-1EA – Sigma-Aldrich) while cells on a chamberslide were sealed with parafilm. After primary antibody incubation the cells were washed 3 times with 1x PBS and then incubated with an appropriate secondary antibody (Table 14) in 1x PBS for 2 h at RT in a humidified chamber (dark). Finally, the cells were washed again thrice with 1x PBS, nuclei were stained with DAPI for 10 min at RT (1:1000 in 1x PBS, #D1306 – Molecular Probes™, Thermo Fisher), again washed with 1x PBS and mounted with Mowiol (Mowiol® 4-88, #475904-100GM – Merck Millipore).

Paraffin sections were first deparaffinized and hydrated (2.10.2). In order to perform an antigen retrieval the slides were then cooked in sodium citrate buffer (Table 38) in a microwave for 12 min and cooled down at RT. The slides were then treated as cells described above.

Cryosections were thawed and cleaned of Tissue Tec (2.10.2). The slides were then treated like cells as described above. Numb antibody staining in tissue sections was performed with a TSA™ Fluorescein amplification kit (TSA™ Fluorescein System #NEL701A001KT – Perkin Elmer) and the use of TN buffer (Table 39).

Immunofluorescence pictures were acquired either with a fluorescence microscope (Zeiss Z1, Zeiss Imager) or a confocal laser scanning microscope (CLSM - Leica TCS SP2, AOBS) as z-stacks. The acquired images were further processed either with Zen software (Zeiss Z1) or multichannel image processing software (Bitplane, Zürich, Switzerland). The images were further edited and merged with Adobe Photoshop software CC2014.

2.10.5 Counting of immunofluorescence labeled cells

In order to determine ATII cell numbers in adult mouse lung (8 week old) cryosections were performed as described in 2.10.1 and 5 slides (2-3 consecutive sections each) with a distance of about 50 µm to each other were collected for each mouse lung. Immunofluorescence double staining was performed using both anti-SPC to stain for ATII cells and anti-CC10 to distinguish Clara Cells. As secondary antibodies anti-rabbit Alexa594 (ATII cells) and anti-goat Alexa488 (Clara Cells) were used (antibodies: Table 14). Nuclei were stained with DAPI (2.10.4). 5 eye fields per lung section on one slide were acquired randomly by CLSM in z-stacks (2.10.4), edited with Adobe Photoshop CC2014 and analyzed with ImageJ software

1.49r (Wayne Rasband – National Institutes of Health, USA). 15 eye fields in total were analyzed. Only SPC^+/ $DAPI^+$ cells were counted as one event (ATII cell) and compared to the total cell number ($DAPI^+$ cells of all eye fields). Double positive $SPC^+/CC10^+$ as well as single positive $CC10^+$ cells were not counted.

2.11 Pathology model

2.11.1 Bleomycin induced lung fibrosis

In order to induce lung fibrosis in our mice we made use of the quite well established bleomycin injury model [62, 136, 137]. The animals that we used for these experiments were male dKO and Ctrl (*SPCrtTA//Cre//Numb//Numblike//RosaYFP*) mice at an age of 10-12 weeks upon application of bleomycin. Therefor, we dissolved bleomycin sulphate (Bleomedac®, 15 mg, 15 USPI) in sterile NaCl solution (0.9 % NaCl – B Braun) and instilled the animals with a single dose of 0.0675 mg in 90 µl NaCl solution (2.5 U/kg BW) orotrachealy. As controls, both groups of mice were instilled only with NaCl solution. Treated animals were then sacrificed 14 and 21 days after induction of fibrosis by bleomycin and further analyzed.

2.11.2 Lung compliance measurement

The *in vivo* lung function measurements were performed in using the flexiVent™ system (Scireq®, Emka Technologies) [138, 139]. Bleomycin treated animals that were analyzed at 14 and 21 days post injury were first narcotisized as described previously and then immediately subjected to the flexiVent™ analyzer to assess lung compliance parameters such as lung volume, dynamic (Crs) and static (Cst/kg) compliance, tissue elastance (dynamic elastance) and tissue damping (dynamic resistance). The data acquisition was performed by flexiWare software (Scireq®, Emka Technologies) and results were exported to Microsoft Excel and further analyzed with Prism 5 software (GraphPad).

2.11.3 Sircol Collagen Assay

The total collagen contents of bleomycin treated animals as well as the control groups were determined by SIRCOL Collagen Assay (Sircol Collagen Assay Kit: Standard Assay (120 assays), #S1000 – Biocolor Ltd.) as described by the manufacturers protocol. This assay detects all collagen derivatives in total lung homogenates and thereby total collagen content in relation to total lung protein was quantified.

2.11.4 Fibrotic Score

In order to assess the actual degree of lung fibrosis in bleomycin treated animals, total lung sections were evaluated according to their amount of fibrotic foci by fibrotic scoring. Therefore, pictures of whole Trichrome or HE-stained lung tissue sections from bleomycin treated animals were acquired with a Keyence BZ-9000 microscope and merged lung pictures were randomly chosen for scoring. Each of the corresponding single pictures from a whole section scan was then analyzed and values from 0 (not fibrotic) to 7 (highly fibrotic) were assigned for all high power fields. The scoring results were averaged and presented in a bar diagram (Prism; GraphPad).

2.12 Statistical analysis

Data and results were analyzed and visualized with Microsoft Excel 2011 (Microsoft) and Prism software version 5 (GraphPad Software, San Diego, CA). Results are presented as mean ±SEM and *P*-values were determined by two-tailed Student's *t*-test (unpaired). Values of $P < 0.05$ were considered as significant and *n* represents the number of separate experiments performed.

2.13 List of Antibodies

Antibodies	Cat. N^{o} - Distributor	Dilution (WB/ IF/IP)
Anti-Numb (C29G11)	#2756 – Cell Signaling	1:1000/ 1:200-1:1000/ -
Anti-Numblike	#101111-AP – Proteintech	1:1000/ 1:200/ -
Anti-Numblike (NUMBL)	#ab37500 – Abcam	1:500/ 1:200/ -
Anti-E-Cadherin [DECMA-1]	#ab11512 – Abcam	1:1000/ 1:50/ -
Anit-ß-Catenin (pan)	#9562 – Cell Signaling	1:1000/ 1:100/ -
Anti-phospho-ß-Catenin (Ser33/37/Thr41)	#9561 – Cell Signaling	1:1000/ -/ -
Anti-non-phospho (active) ß-Catenin (Ser33/37/Thr41)	#8814 – Cell Signaling	1:1000/ -/ -
Anti-Cortactin	#3502 – Cell Signaling	1:1000/ -/ -
Anti-Cortactin (p80/85), Clone 4F11	#05-180 – EMD Millipore	-/ -/ 8µg per mg protein

Mouse IgG1 (G3A1) Isotype Control	#5415S – Cell Signaling	-/ -/ 6-8µg per mg protein
Anti-CK2alpha	#2656 – Cell Signaling	1:1000/ -/ -
Anti-CK2alpha (8E5)	#LF-MA0223 – Thermo Fisher	-/ -/ 6µg per mg protein
Anti-CK2beta	#PA5-27416 – Thermo Fisher	1:1000/ -/ -
Anti-proSPC	#AB3786 – Millipore	-/ 1:400/ -
Anti-CC10 (T-18)	#Sc-9772 - Santa Cruz	-/ 1:200/ -
Anti-ZO-1 (C-19)	#Sc-8146 – Santa Cruz	1:500/ -/ -
Anti-ZO-1/ TJP1	#40-2200 – Thermo Fisher	-/ 1:100/ -
Anti-rabbit-HRP (goat)	#31460 – Thermo Fisher	1:1000/ -/ -
Anti-mouse-HRP (goat)	#31430 – Thermo Fisher	1:1000/ -/ -
Anti-rat HRP (goat)	#HAF005 – R&D Systems	1:1000/ -/ -
Anti-rabbit Alexa488 (goat)	#A11070 – Thermo Fisher	-/ 1:1000/ -
Anti-rabbit Alexa594 (goat)	#A11012 – Thermo Fisher	-/ 1:1000/ -
Anti-rat Alexa594 (goat)	#A11007 – Thermo Fisher	-/ 1:1000/ -

Table 14: Antibodies – Dilutions for Western Blot (WB), immunofluorescence (IF) and immunoprecipitation (IP)

2.14 Buffers and solutions

50x TAE (Tris-acetate-EDTA)	5 l
Tris (#5429.2 – Roth)	1210 g
100% Acetic acid	285.5 ml
0.5 M EDTA	500 ml
MilliQ-H_2O, fill up to	5 L

Table 15: 50x TAE

1x TAE	10 L
50x TAE	200 ml
MilliQ-H_2O, fill up to	10 L

Table 16: 1x TAE

10x PBS	1 l
NaCl (#3957.2 – Roth)	80 g (1.37 M)
KCl (#6781.3 – Roth)	2 g (27 mM)
Na_2HPO_4	14.4 g (100 mM)
KH_2PO_4	2.4 g (18 mM)
Dissolve in ddH2O	800 ml
Adjust to pH 7.4 (30% HCL), fill up to	1 l

Table 17: 10x PBS

1x PBS	1 l
10x PBS	100 ml
H_2O dest.	900 ml

Table 18: 1x PBS

1x Trypsin/EDTA (T/E)	10 ml
10x T/E (Sigma)	1 ml
Sterile 1x PBS	9 ml

Table 19: 1x Trypsin/EDTA (T/E)

Buffer I (4°C)	1 L
5M EDTA	20 ml
1M Tris-HCl pH 8.0	50 ml
H_2O dest.	Add to 1 L

Table 20: Buffer I (Mini-preparation)

Buffer II (RT)	1 L
5M NaOH	40 ml
20 % SDS (or 10g SDS)	50 ml
H_2O dest.	Add to 1 L

Table 21: Buffer II (Mini-preparation)

Buffer III (4°C)	1 L
3M Potassiumacetate	1 L
Adjust to pH 5.5 with acetic acid	dropwise

Table 22: Buffer III (Mini-preparation)

TENS-Buffer pH 7.4	500 ml
1 M Tris/ HCl pH 8.0	25 ml
0.5 M EDTA	40 ml
10 % SDS	50 ml
5 M NaCl	10 ml
MilliO-H_2O	375 ml

Table 23: TENS-Buffer

TE-Buffer (Tris-EDTA)	50 ml
1 M Tris pH 8.0	0.5 ml
0.5 M EDTA pH 8.0	0.1 ml
MilliQ-H_2O	49.4 ml

Table 24: TE-Buffer

5x LB-sample buffer	45 ml
1M Tris-Hcl pH 6.8	3 ml
10% SDS	10 ml

H_2O	32 ml

Table 25: 5x LB-sample buffer

Extraction buffer (EP)	100 ml
1M Tris HCL pH 8.0	10 ml
SDS powder (#2326.2 – Roth)	10g (=10%)
EDTA	0,372g
H_2O	50 ml
With 30% HCl	Adjust pH 8.0
Add H_2O	To 100 ml
Aliquots to store at -80°C	2 ml, 10 ml

Table 26: Extraction buffer (EP)

RIPA modified buffer pH 7.4	100 ml
1M Tris/HCL pH 7.5	5 ml
10 % NP-40 (Roth)	10 ml
Sodium-desoxycholate (Sigma)	0.25 g
1M NaCl	15 ml
0.5 M EDTA	200 µl
Fill up with H_2O	70 ml

Table 27: RIPA modified buffer

Dilution/Wash buffer (DB/WB)	100 ml
1M Tris/HCl pH 7.5	1 ml
1M NaCl	15 ml
0.5 M EDTA	100 µl
Add H_2O	84 ml

Table 28: Dilution/Wash buffer (DB/WB)

Protease inhibitors	Per 1 ml of lysis buffer
Benzamidine (250mg/ml)	2µl
Aprotinin (2mg/ml)	1µl
Leupetin (2mg/ml)	1µl
PMSF (0,2M)	10µl
Na3VO4 (1M)	1µl
NaF (1M)	20µl

Table 29: Protease inhibitors

NuPAGE® MOPS SDS running buffer	2.5 l
20x MOPS (#NP0001-02 – Invitrogen)	0.125 l
Milli-Q H_2O	2.375 l

Table 30: MOPS running buffer

NuPAGE® MES SDS running buffer	2.5 l
20x MES (#NP0002-02 – Invitrogen)	0.125 l
Milli-Q H_2O	2.375 l

Table 31: MES running buffer

1x Transfer buffer	5 l
100% MeOH	0.250 l
20x Transfer buffer	1 l
Milli-Q H_2O	3.750 l

Table 32: 1x Transfer buffer

20x Transfer buffer	2 l
Bicine	163.2 g
Bis-Tris	209.6 g

EDTA	12 g
Milli-Q H_2O, fill up to	2 l

Table 33: 10x Transfer buffer

10x TBS	1 l
NaCl	80 g
KCl	2g
1 M Tris pH 7.5	25 ml
MilliQ-H_2O, fill up to	1 l

Table 34: 10x TBS-T

1x TBS-T	1 l
10x TBS	100 ml
Tween 20® (#9127.2 – Roth)	1 ml
MilliQ-H_2O	900 ml

Table 35: 1x TBS-T

9% Bis-Tris Polyacrylamid gel PAA	
Separation gel:	9 %
Rotiphorese® Gel 30 (37.5:1) (#3029.1 – Roth)	2.1 ml
3.5 x bis-Tris pH 6.5 – 6.8	2 ml
Milli-Q H_2O	2.9 ml
10 % Ammoniumperoxo-disulfat (APS #1.01201 - Merck)	25 µl
TEMED (#2367.1 – Roth)	7 µl
Stacking gel:	5 %
Rotiphorese® Gel 30 (37.5:1) (#3029.1 – Roth)	0.29 ml

3.5 x bis-Tris pH 6.5 – 6.8	0.5 ml
Milli-Q H_2O	0.96 ml
10 % Ammoniumperoxo-disulfat	8 µl
TEMED	3 µl

Table 36: 9% Bis-Tris Polyacrylamid Gel

FACS sorting buffer	100 ml
0.5 M EDTA pH 8.0	1 ml
1 M HEPES	2.5 ml
1x PBS	96.5 ml

Table 37: FACS sorting buffer

Sodium citrate buffer pH 6.0	1 L
Tri-sodium citrate (dihydrate)	1.47 g
Dissolve in ddH_2O	800 ml
Adjust to pH 6.0 (30% HCl), fill up to	1 L
Add Tween 20	250 µl

Table 38: Sodium citrate buffer

TN buffer pH 7.4	1 L
1 M Tris/ HCl pH 7.5	100 ml
1 M NaCl	150 ml
MilliQ-H_2O	750 ml
Adjust to pH 7.4 (30 % HCl)	Few drops

Table 39: TN buffer

3 RESULTS

3.1 Lung epithelial specific inactivation of Numb on a Numblike deficient background in mice exhibits mild structural phenotype and does not affect viability

As previously described, constitutive gene inactivation of both *Numb* alleles in mice results in embryonic lethality at day E11.5 associated with neuronal defects as well as extensive bleeding, whereas single constitutive depletion of *Numblike* exhibits only a loss of fertility in females [117]. However, constitutive double knockout of both *Numb* and *Numblike* results in a more severe phenotype accompanied with an earlier embryonic lethality at E9.5 [118]. In order to study tissue specific functions of Numb and Numblike proteins, conditional inactivation strategies have been utilized and studied in brain or heart so far [2, 112, 118]. During heart development for example, myocardial directed inactivation of *Numb/Numblike* revealed that both proteins synergistically control myocardial compaction by inhibiting Notch-signaling pathway [2]. Actually, there are also investigations in murine lung associating Numb, amongst other polarity proteins, with functions in Eya1 controlled epithelial cell polarity as well as asymmetric cell division during lung morphogenesis [122]. Additionally, there is evidence showing that Numb might exhibit tumor suppressive potential in human non-small-cell lung carcinomas (NSCLCs) [127]. Nevertheless, the underlying mechanisms, in which Numb might be involved during these processes, remain poorly understood. In order to elucidate the functional impact of both proteins Numb and Numblike during lung epithelial development and regeneration, conditional loss-of-function double mutants in mice were performed.

3.1.1 Conditional Numb/Numblike double mutants display no obvious pulmonary epithelial defect

In order to elucidate the role of Numb and Numblike specifically during murine lung epithelial development and regeneration conditional loss-of-function, double mutants were generated. The reverse tetracycline transactivator (rtTA) expressed under control of the lung epithelial specific *Spc* promoter (*SPCrtTA* [130]) was utilized to induce Cre-mediated (*tetO-Cre*) depletion of *Numb* ($Numb^{fl/fl}$) on a *Numblike* deficient ($Numblike^{+/-}$) background upon administration of doxycycline (Tet-On System). To

ensure complete recombination of *Numb*$^{fl/fl}$ in developing lung epithelium, mice received doxycycline (Dox) supplemented to their drinking water from gestation to postnatal stage P28 (Figure 6A). Offsprings were born according to Mendelian ratios and double homozygous *Numb/Numblike* mutants (dKO) are viable showing no severe phenotypic abnormalities of the lung. Additionally, the animals were combined with a fluorescent Cre-reporter (*RosaYFP*) to visualize and trace Cre activity and to obtain a tool that enables isolation of lung epithelial cells by FACS sorting (dKO: *SPCrtTA*$^{+/-}$*// tetO-Cre*$^{+/-}$*// Numb*$^{fl/fl}$*// Numblike*$^{-/-}$*// RosaYFP*$^{+/-}$). Dox treated mice containing the wild type alleles for *Numb* and *Numblike* served as controls (WtCtrl: *SPCrtTA*$^{+/-}$*// tetO-Cre*$^{+/-}$*// Numb*$^{+/+}$*// Numblike*$^{+/+}$*// RosaYFP*$^{+/-}$). As demonstrated in Figure 6E, Dox activation of the Cre system from gestation on results in a YFP positive lineage tracing of cells comprising the entire mature lung epithelium driven by the Alveolar Type II (ATII) cell-specific expression of *SPCrtTA*$^{+/-}$*//tetO-Cre*$^{+/-}$ in a proximo-distal pattern. In order to test both the recombination efficiency of conditional *Numb* as well as constitutive *Numblike* deficiency, RNA of 8 week lungs was extracted to determine relative mRNA expression levels for both genes by TaqMan® Gene Expression analysis (Figure 6B). Since *Numb* is expressed in multiple cell types of the entire lung no significant reduction of relative mRNA level was detectable in the lung epithelial specific dKOs, while *Numblike* expression was absent compared to littermate controls (Ctrl). In order to enrich for a lung epithelial cell population, lineage traced YFP positive epithelial cells of dKOs and WtCtrl animals were FACS sorted and subjected to TaqMan® Gene Expression analysis. By using this approach, *Numb* expression of dKO derived epithelial cells revealed a dramatic and significant reduction in comparison to sorted primary lung epithelial cells from WtCtrl animals. This clearly demonstrated that *Numb*$^{fl/fl}$ was specifically depleted in lung epithelial cells, while surrounding mesenchymal cells remained unaffected. *Numblike* mRNA level of sorted epithelial dKO cells showed a robust loss of expression as well. Furthermore, protein analysis of total lung homogenates went in line with immunofluorescence analysis of embryonic (E16.5) and adult lungs, confirming decreased Numb and Numblike expression levels in dKOs (Figure 6C, D). Numb protein could be detected with a moderate but significant decrease in adult dKO lung homogenates, while immunostained embryonic and adult dKO lung sections displayed a specific Numb depletion restricted to lung epithelium from early lung development onwards.

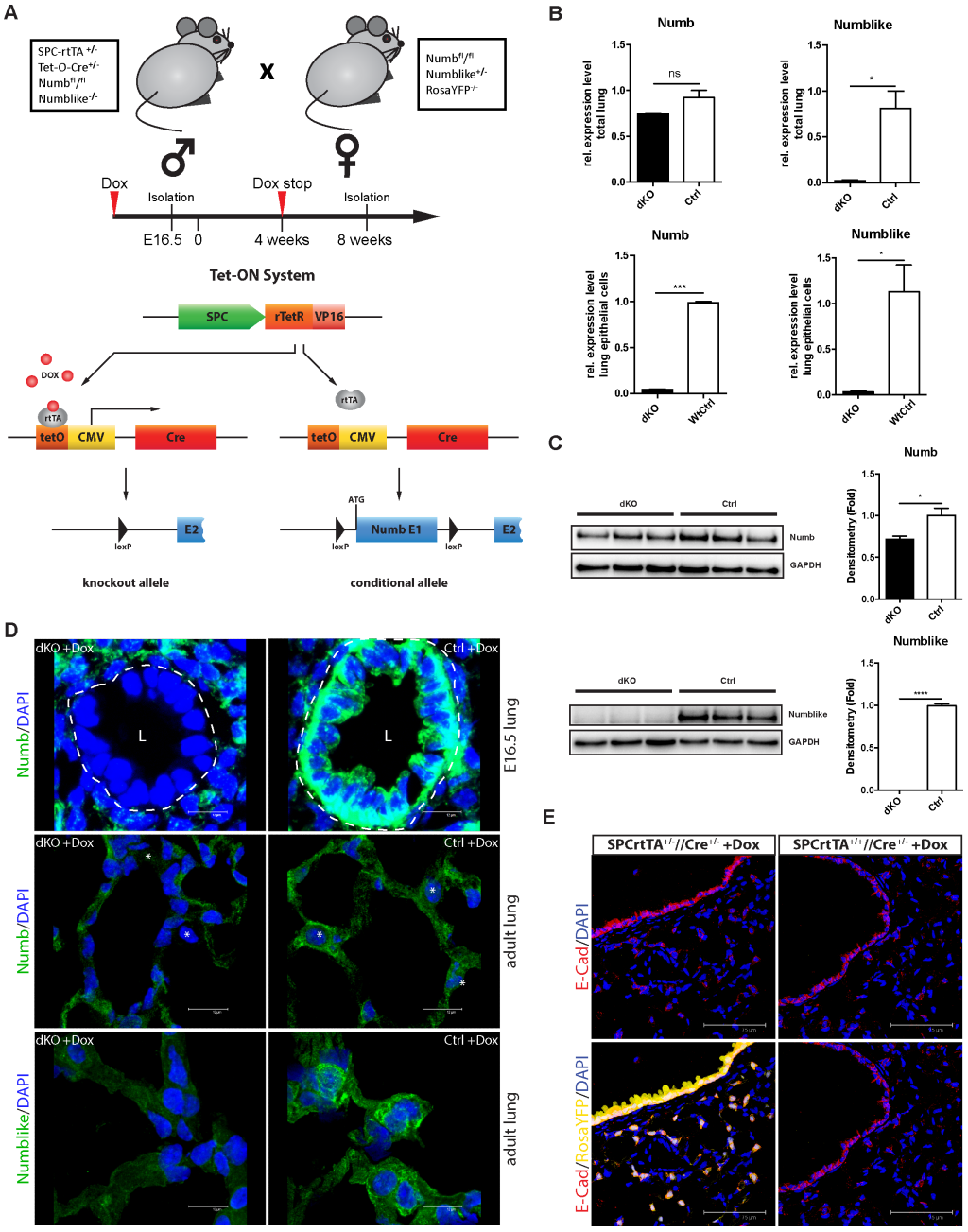

Figure 6: Inducible conditional knockout of Numb in lung epithelium (Tet-ON).
A: Mice were crossed as depicted. Induction of the Tet-ON system occurs after administration of doxycycline (Dox) supplemented drinking water. The lung specific *SPC*-promoter drives expression of the *reverse Tetracycline Repressor* domain (*rTetR*). In the presence of Dox reverse Tetracycline Transactivator (rtTA) is expressed and binds to the *tet-operon* of *CMVCre* (*tetO-Cre*). Expressed Cre mediates recombination of the floxed *ATG* region of *Numb Exon1*. **B:** Relative mRNA expression levels of total lung homogenates and FACS sorted YFP^{+} primary lung epithelial cells. **C:** Western Blot analysis of total lung protein (n=3 each group) for Numb and Numblike. Densitometry analysis *vs.* GAPDH. **D:** Cryosections of E16.5 and 8 week old lungs, isolated from dKO and littermate control mice treated with Dox, were immunostained for Numb (both) and Numblike (adult). Images were acquired as confocal z-stacks. Basal lamina is depicted by dashed line in white (E16.5). White stars depict epithelial cells (e.g. ATII) determined by E-Cadherin staining (here not shown). L highlights the primordial respiratory lumen. **E:** Cryosections of adult Dox treated animals, showing proximal and distal YFP^{+} labeled, E-Cadherin positive (E-Cad; red) lung epithelial cells *vs.* YFP^{-} littermate controls. Pictures were acquired with a Leica confocal laser microscope as z-stacks. Scale bars in D: 12 µm (digital zoom of 63x magnification), in E: 75 µm (cropped image of 40x magnification). Graphs show mean ±SEM of n=3 animals each group with *$p < 0.05$, ***$p < 0.001$ and ns = not significant.

Numb expression in mesenchymal lung cells remained unaffected in the mutants, which is indicated by their positive indirect immunofluorescence labeling of Numb. Immunofluorescence analysis of Numblike showed a loss of protein abundance in the entire lung, which was consistent with the loss of relative mRNA expression and protein levels of Numblike in total lung homogenates (Figure 6B, C, D). Taken together, the data revealed an efficient and lung epithelial specific depletion of the floxed first exon encoding the *ATG* start codon of *Numb*, which terminates Numb translation in Dox induced dKOs. The loss-of-function studies for Numb and Numblike in lung epithelium showed that both are dispensable for lung development, maturation and maintenance and consequently for survival of the animals.

3.1.2 Loss of Numb/Numblike in lung epithelium results in reduction of ATII cell numbers

The early embryonic depletion of *Numb* and *Numblike* in lung epithelium didn't affect overall lung architecture and had no impact on the viability of dKOs (examination of lung structure on HE-stained lung sections, data not shown). However, the Dox induced ablation of *Numb* on a *Numblike* deficient background was efficient and specifically restricted to lung epithelium. In order to get a deeper insight into subtle changes of the lung epithelium, mRNA expression of well-defined characteristic epithelial marker genes was analyzed to deduce potential changes of different cell type abundance along the proximo-distal axis of mature lung epithelium. This analysis was performed by using cDNA of total adult lung homogenates and taking in consideration that relative expression levels of the examined marker genes correlate to the relative cell abundance in the epithelium. The data showed that the expression profiles for all tested lung epithelial specific cell marker genes, *Pdpn* (ATI cell), *Sftpc* (ATII cell), *Scgb1a1* (Clara cell), *Foxj1* (Ciliated cell) and *Ascl2* (Neuroendocrine cell), remained unaffected in dKOs except the ATII cell specific *Sftpc* (SPC) marker gene expression, which was significantly decreased by nearly 50 % (Figure 7A). In order to correlate the reduced *Sftpc* expression with ATII cell abundance in the lung epithelium of dKOs, tissue sections of mature lungs were labeled with anti-SP-C antibody and SP-C$^+$ cells were quantified compared to total cell numbers (DAPI$^+$) per high power field (hpf). The results documented that dKOs indeed exhibited a significant decrease of SP-C$^+$ labeled ATII cells around nearly one third compared to SP-C$^+$ positive cells in Ctrl animals (Figure 7B). This data could be additionally

confirmed by quantification of ATII cells on ultrastructural images acquired by electron microscopy (Data by Dr. Sawa Kostin, Figure 7C).

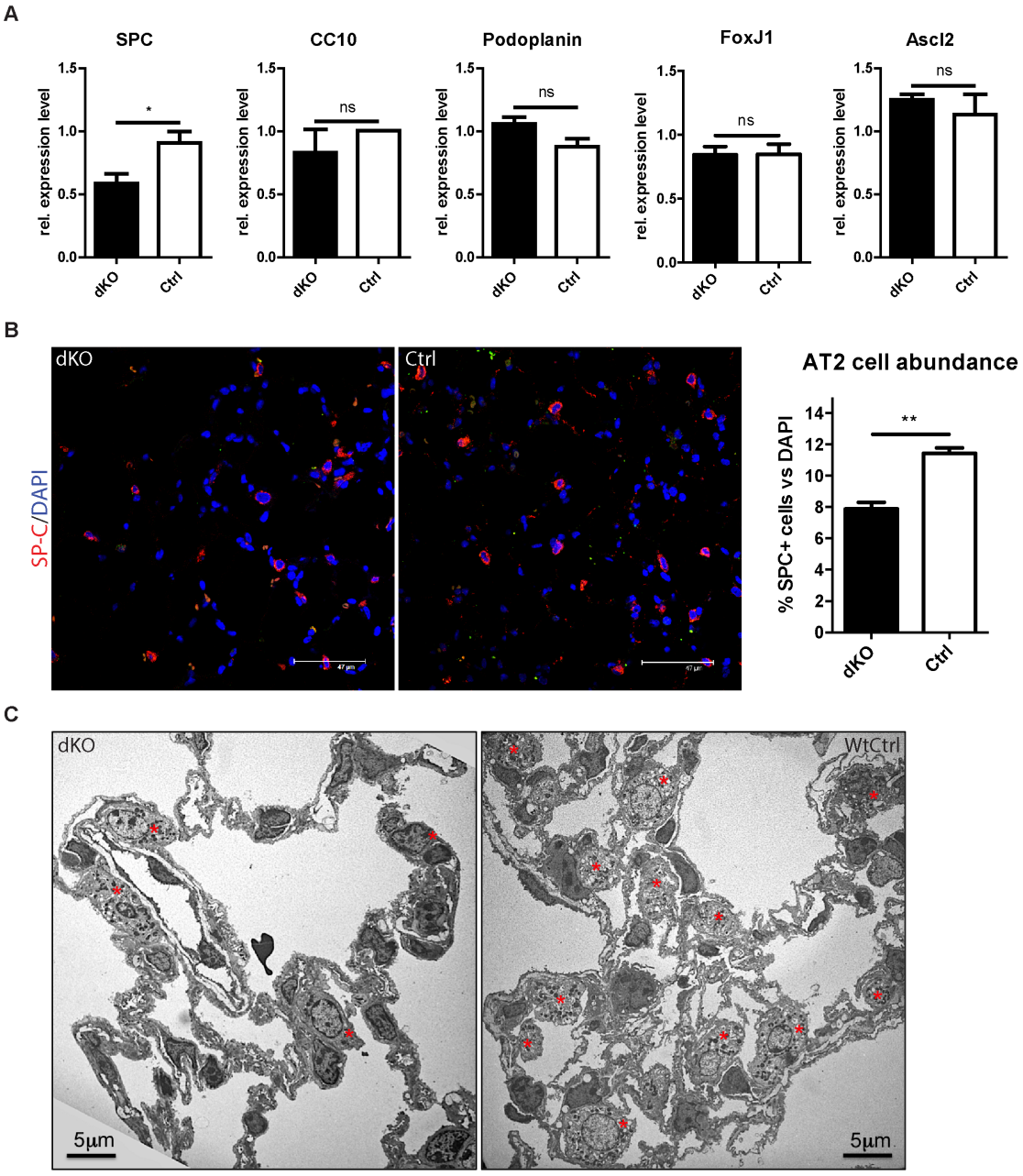

Figure 7: Reduction of ATII cell abundance in Numb/Numblike dKOs.
A: Relative expression levels of lung epithelial cell markers of total adult lung RNA. TaqMan® Gene Expression probes were used to analyse specific marker genes for ATI cells (*pdpn*, Podoplanin), ATII cells (*sftpc*, SP-C), Clara cells (*scgb1a1*, CC10), Ciliated cells (*foxj1*, Foxj1) and Neuroendocrine cells (*ascl2*, Mash2). **B:** Cryosections (5µm) of adult dKO and Ctrl lungs immunostained for SP-C (red). Three serial lung sections with a distance of 50µm between each other were analyzed per animal. Quantification of SP-C$^+$ cells to total cell numbers (DAPI) of 5 randomly acquired confocal z-stack images per tissue section. Images at a magnification of 63x, Scale bars 47 µm **C:** Ultrastructural analysis of adult dKO and Ctrl lungs by electron microscopy. Red stars refer to ATII cells that could be determined by characteristic ultrastructural features on the image (scale bar 5 µm). All graphs show mean ±SEM of n=3 animals each group with *$p < 0.05$, **$p < 0.01$ and ns = not significant.

3.1.3 Numb/Numblike mediate cell-cell contacts and apico-basal epithelial cell polarity

It has been previously shown that the loss of Numb can influence cell-cell contacts as well as an apico-basal polarity of epithelial cells *in vitro* [10]. In this respect, the epithelial cell marker E-Cadherin and its interaction with membrane located Numb play an important role. Numb regulates the localization of E-Cadherin to the lateral domain of epithelial cell-cell junctions in polarized cells. Reduced Numb protein level in these cells promoted by shRNA mediated silencing of *Numb* expression results in baso-lateral to apico-lateral translocation of E-Cadherin and ß-Catenin [10]. Hence, the subcellular localization of the adherens junction mediating E-Cadherin was examined in dKOs at embryonic stage E16.5 as well as in mature lung epithelium. Therefore, immunofluorescence stainings for E-Cadherin and Numb were performed on embryonic lungs (E16.5) and adult lungs. Analysis of these stainings revealed a translocation of E-Cadherin from baso-lateral to apico-lateral in E16.5 dKO lung epithelium in the absence of Numb (Figure 8A), whereas Numb and E-Cadherin partially co-localize at the baso-lateral membrane in epithelial cells of control lungs. The same phenomenon was observed in mature lung epithelium of dKO animals where mislocalized E-Cadherin was identified along the entire proximo-distal axis of lung epithelium in an apico-lateral pattern upon loss of Numb and Numblike (Figure 8B). However, ultrastructural analysis of proximal epithelial cells from adult dKO lungs revealed no changes in the presence of cell-cell contacts compared to Ctrl lungs. In both groups contact zones could be classified by their morphology in tight junction (TJ), adherence junction (AJ) and desmosome (Ds) zones (Figure 8C). Yet, ultrastructural analysis of epithelial cell-cell contacts in dKO and Ctrl lungs were not statistically evaluated or quantified concerning parameters such as contact zone length, interstitial gap opening or numbers of TJ, AJ as well as Ds, which might indicate alterations in quality and numbers of contact zones of dKOs. Furthermore, previous studies revealed direct interaction between ß-Catenin and E-Cadherin in epithelial cells and subcellular localization of ß-Catenin can be influenced by the mislocalization of E-Cadherin upon loss of Numb [10, 140, 141]. Accordingly, ß-Catenin localization was examined in E16.5 dKO lungs where a similar translocation of the membrane-tethered E-Cadherin to apical membrane was initially illustrated (Figure 8A).

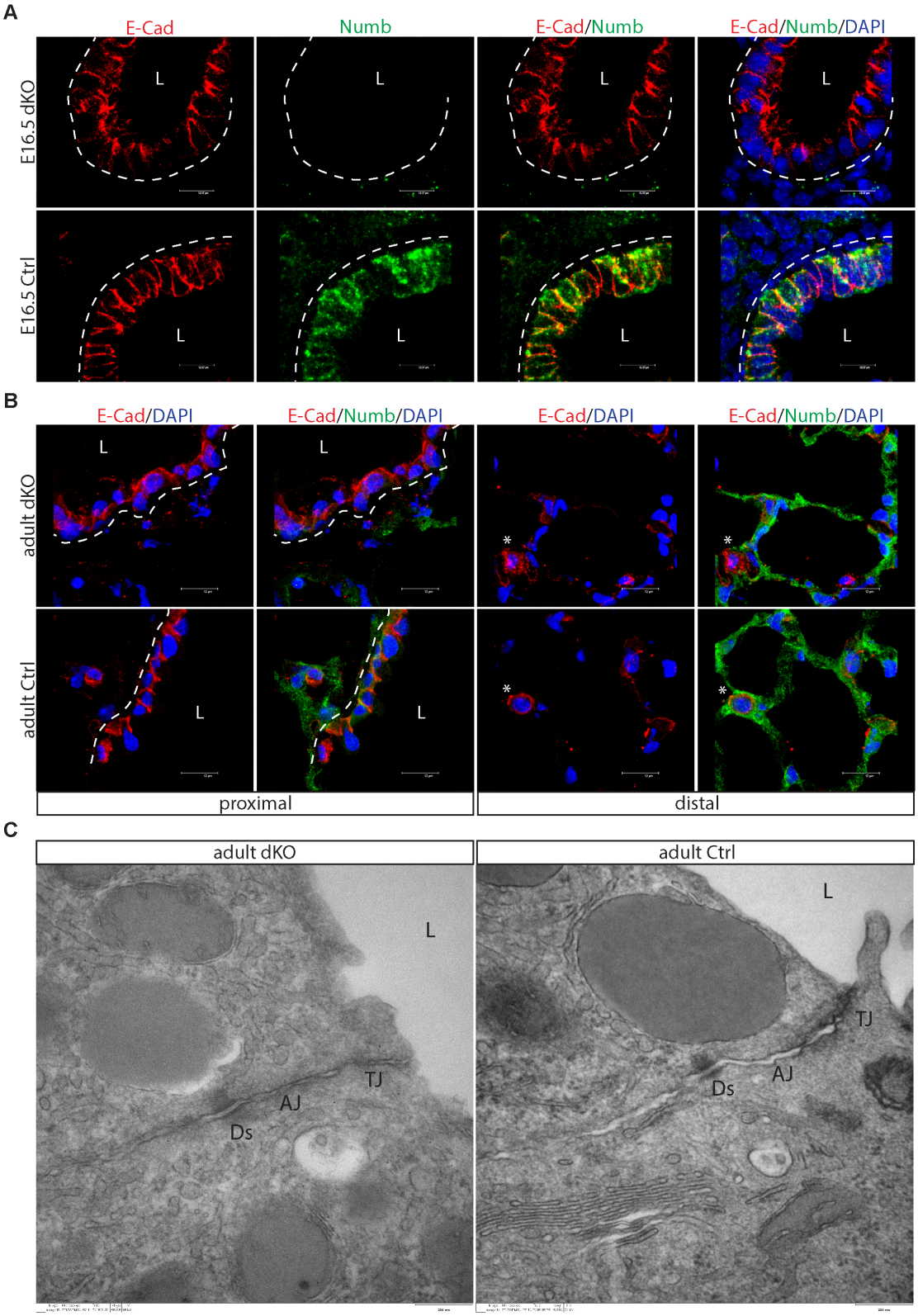

Figure 8: Mislocalization of E-Cadherin in Numb/Numblike depleted lung epithelium.
A + B: Immunofluorescense images for E-Cadherin (red) and Numb (green) of E16.5 and adult lungs. Confocal images acquired as z-stacks. Scale bars 12.37 µm (A) and 12 µm (B). Zoom of 63x magnification. White dashed lines resemble basal lamina while L highlights the lumen. Stars highlight distal ATII cells **C:** Ultrastructural analysis of cell-cell contacts between proximal lung epithelial cells of n = 2 dKO and Ctrl. Scale bar 250 nm. L represents the luminal (apical) side of the epithelium. Cell contacts between epithelial cells of dKO and Ctrl are marked by regions of tight junctions (TJ), adherence junctions (AJ) and desmosomes (Ds).

Additionally, immunofluorescence labeling of ß-Catenin also displayed translocation of the protein in primordial lung epithelial cells of E16.5 dKOs to apical cellular compartments (Figure 9A). This translocation is nicely depicted by cross-sectional projections of x/z and y/z as well as by x/y views of confocal z-stacks where ß-Catenin positive signal appeared more at the luminal (apical) borders (L) of embryonic epithelium, whereas ß-Catenin in E16.5 Ctrls mainly localized at the membrane in a baso-lateral pattern. Hence, these results clearly indicated a disorganization of E-Cadherin and ß-Catenin, which are both components of the adherence junction complex mediating cell-cell contacts [142]. In order to examine the state of tight junction mediated cell contacts in Numb and Numblike depleted lung epithelium, localization of the tight junction protein ZO-1 was determined in the lung epithelial membrane of E16.5 dKOs and their littermate controls by immunofluorescence labeling (Figure 9B).

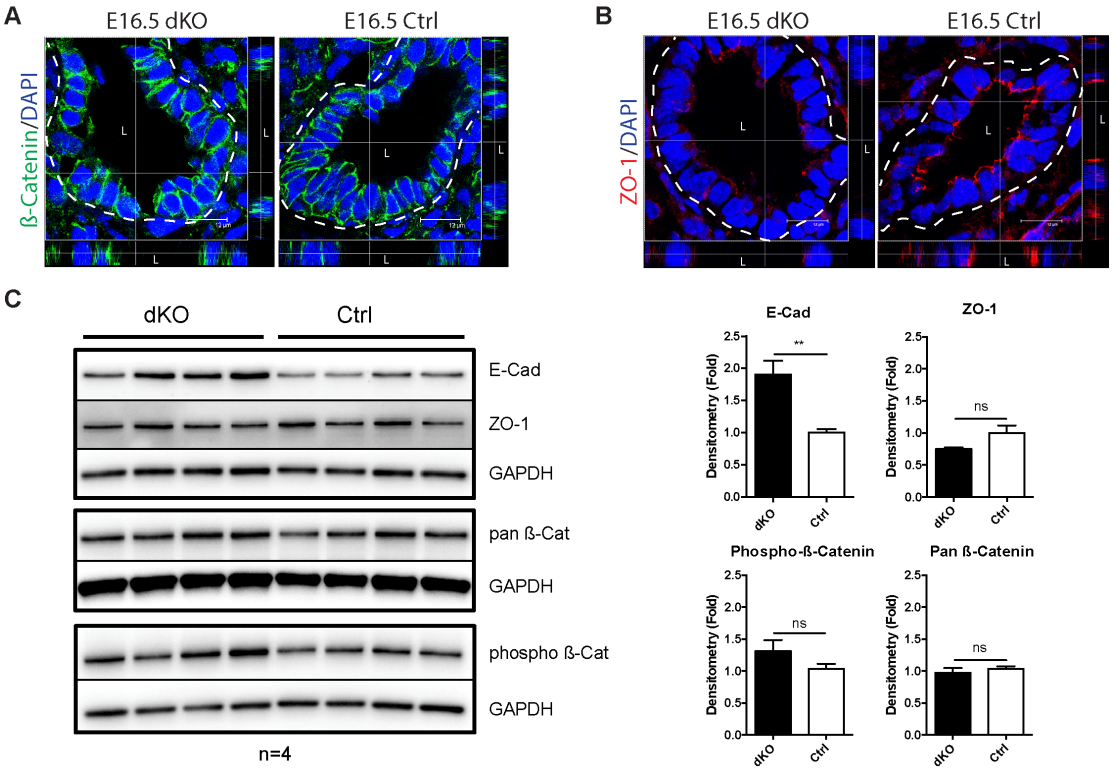

Figure 9: Mislocalization of ß-Catenin and ZO-1 in E16.5 lung epithelium.
A: Cryosections of E16.5 lung immunostained for ß-Catenin. **B:** Cryosections of E16.5 lung immunostained for ZO-1. Dashed lines in **A** + **B** represent the basal lamina. L = lumen. Pictures were acquired by CLSM as z-stacks and depicted as cross-sections with x/y, x/z, y/z projection. Digital zoom of 63x magnification with scale bar at 12µm. Randomly chosen cryosections of n=3 animals each group were stained and analyzed. **C:** Western blot analysis of total E16.5 lung protein homogenate for E-Cadherin (E-Cad), ZO-1, pan-ß-Catenin (pan ß-Cat), phospho-ß-Catenin Ser33/37-Thr41 (phospho-ß-Cat) and corresponding densitometry vs. GAPDH. n=4 animals each group. All graphs show mean ±SEM with $^{**}p < 0.01$ and ns = not significant.

In addition to mislocalization of E-Cadherin and ß-Catenin, the tight junction protein ZO-1 also mislocalized in an apical and diffuse pattern in comparison to Ctrls, which were marked by defined localization of ZO-1 at the apico-lateral membrane of contact zones between epithelial cells. Even though the abundance of ZO-1 signal in E16.5 dKOs seems slightly weaker compared to control staining, quantitative Western blot analysis of total E16.5 lung protein homogenates revealed no significant changes of ZO-1 protein abundance (Figure 9C). In order to examine potential alterations of E-Cadherin and ß-Catenin on the protein level as well, which might accompany their subcellular mislocalization, quantitative Western blot analysis of total E16.5 lung protein homogenates were performed. Both phospho-ß-Catenin and total ß-Catenin (pan) levels remained unaffected in total lung protein of E16.5 dKOs, while E-Cadherin protein level was significantly increased by two-fold. However, E-Cadherin level of total protein homogenates derived from adult dKO lungs was not altered in comparison to Ctrl (Figure 10C), while the mislocalization of E-Cadherin in the membrane of adult epithelium was still maintained, as described before (Figure 8B). Similar to the observations at embryonic stage E16.5, mislocalization of ß-Catenin concomitantly to E-Cadherin could be confirmed at adult stages as well. Apical localization and accumulation of ß-Catenin in epithelial cells of adult dKO lungs could be detected by confocal laser microscopy and was highlighted by white arrows on corresponding cross-sectional projections of confocal z-stacks (Figure 10A). This translocation of ß-Catenin to the luminal (L) side of the epithelium in dKOs could be also observed on x/z and y/z confocal projections, while epithelium of Ctrl lungs displayed normal basol-lateral localization of ß-Catenin in all projections. Moreover, alveolar compartments of dKO lungs contained ß-Catenin negative ATII cells, whereas ATII cells of Ctrls exhibited membrane abundance of ß-Catenin (white stars). This partial lack of ß-Catenin could be further verified by Western blot analysis of total lung homogenates. Here, significantly decreased protein levels could be detected for phospho-ß-Catenin Ser33/37-Thr41 as well as for the active (non-phosphorylated) form of ß-Catenin, while total ß-Catenin protein amounts remained unaltered for both groups (Figure 10C). Similar to E16.5, adult dKO lung epithelium displayed a decrease of ZO-1 signal detected by immunohistochemistry and a significant reduction of ZO-1 protein level revealed by Western blots from total lung homogenates (Figure 10B, C). ZO-1 positive clusters of tight junctions between adjacent membranes of distal lung epithelial cells were highlighted by white arrows

on cross-sections of confocal z-stacks and were additionally visualized as x/z or y/z confocal projections (Figure 10B). These tight junction clusters were barely detectable at contact zones of lung epithelial cells in dKO lungs (see white stars Figure 10B).

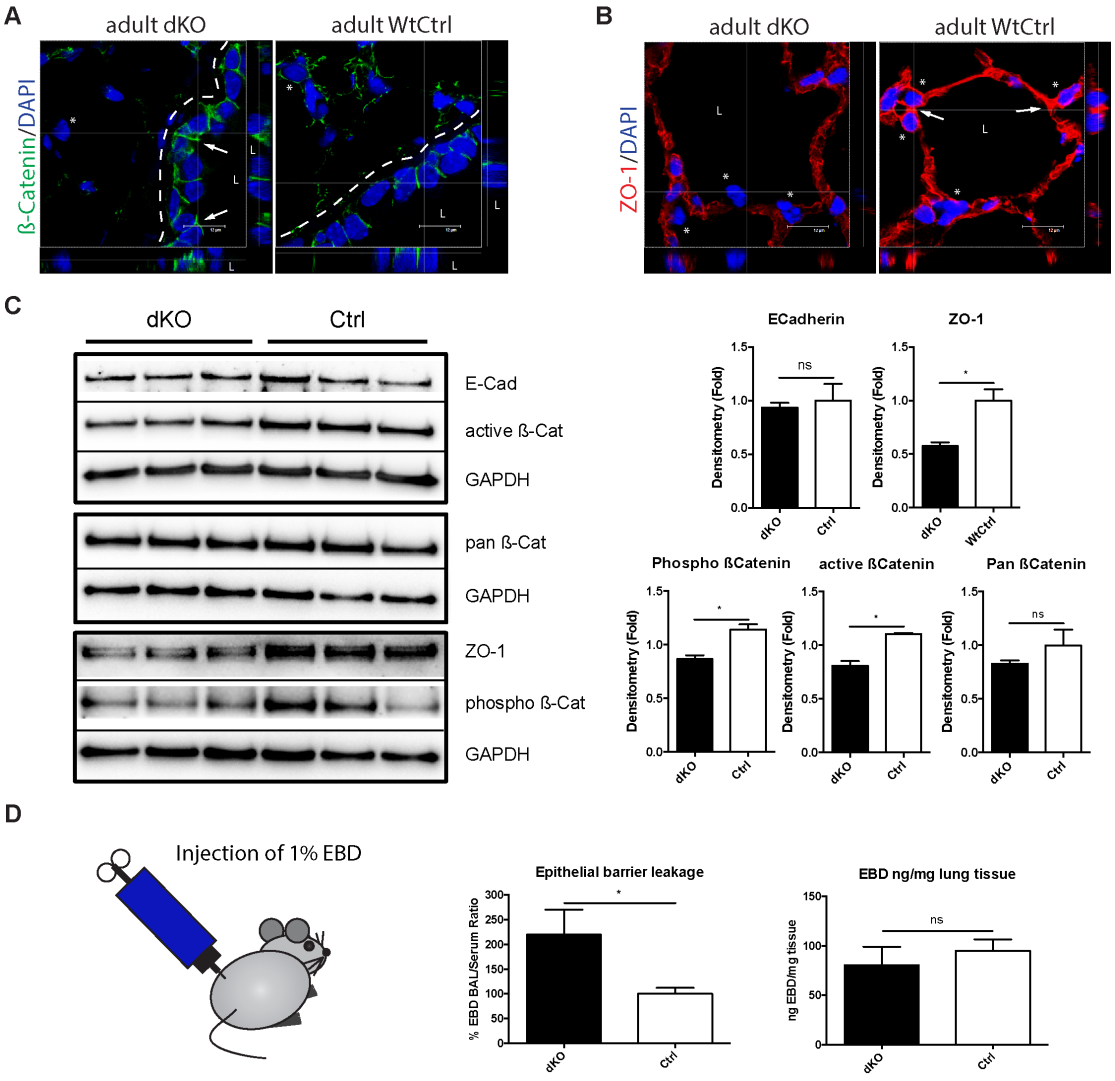

Figure 10: Mislocalization and downregulation of ß-Catenin and ZO-1 in adult lung epithelium. **A:** Cryosections of adult lung immunostained for ß-Catenin. Dashed lines represent the basal lamina. **B:** Cryosections of adult lung immunostained for ZO-1. L = lumen. Pictures were acquired by CLSM as z-stacks and depicted as cross-section with x/y, x/z, y/z projection. Digital zoom of 63x magnification with scale bar at 12µm. Randomly chosen cryosections of n=3 animals each group were stained and analyzed. **C:** Western blot analysis of E-Cadherin (E-Cad), ZO-1, active ß-Catenin (active ß-Cat), pan-ß-Catenin (pan ß-Cat), phospho-ß-Catenin (phospho-ß-Cat) from total adult lung protein homogenates and corresponding densitometry vs. GAPDH. n=3 animals each group. **D:** Analysis of epithelial barrier leakage. n=4 animals each group were *i.p.* injected with 1% Evans Blue Dye (EBD) in 0.9% NaCl solution. After 2h of incubation, first bronchio-alveolar lavage (BAL) was performed and BAL fluid collected. Blood was collected via the eyes. Finally, mice were sacrificed and EBD was extracted from isolated lung tissue as control for accumulation of dye in lung interstitial spaces (ng EBD/mg tissue). Epithelial barrier leakage was determined as percentage EBD in BAL/Serum. All graphs show mean ±SEM with $*p < 0.05$, $**p < 0.01$ and ns = not significant.

Alterations in abundance and localization of adherens and tight junction proteins in dKO animals might influence and destabilize the maintenance of the epithelial barrier function and thereby the integrity of the entire lung epithelium as well. In order to examine potential epithelial barrier leakage in dKO compared to Ctrl lungs, *intra peritoneal* (*i.p.*) injections of 1% Evans Blue Dye (EBD) solution were conducted and leakage of the dye into lung cavity was measured for both groups. After two hours of incubation a lung lavage was performed and bronchio-alveo-lavage fluid (BAL) as well as blood serum were collected to assess the percentage of EBD BAL/Serum ratio by calculating OD_{600} of BAL and blood serum. This ratio provides information about the amount of EBD, which passes the epithelial barrier to the lung lumen. The results clearly displayed a more than two-fold increase of EBD BAL/serum ratio for dKOs in comparison to Ctrls (Figure 10D). In fact, this strongly indicated a disruption of the lung epithelial barrier function, which strengthened the hypothesis of a compromised lung epithelial integrity in Numb/Numblike dKOs. The amount of EBD, which accumulated in lung interstitial spaces during incubation time, is displayed by the amount (ng) of extracted EBD per mg lung tissue (Figure 10D; second graph). These results indicated to what extent EBD was absorbed and retained by the interstitium and thereby served as an experimental control. After isolation of lung tissue and extraction of EBD absorbed by the pulmonary interstitium, the amount of EBD/mg lung tissue (ng EBD/mg lung tissue) was determined. Both groups did not reveal any significant differences in the amount of EBD that accumulated in lung interstitial spaces indicating that the absorption of the dye by the interstitium of dKO and Ctrl lungs was equal. Hence, the elevated EBD measured in the lung cavity (BAL) of dKO mice clearly resulted by an enhanced paracellular dye leakage via the epithelium, whereas the content of the dye that remained in lung interstitial spaces of lungs was similar for both groups. In summary, these results suggested that Numb and Numblike mediate lung epithelial cell polarity as well as the maintenance of cell-cell contacts.

3.2 Numb/Numblike in bleomycin induced fibrosis

3.2.1 Loss of Numb and Numblike is beneficial for survival after lung injury

Previous results of this study unveiled that the conditional lung epithelial specific depletion of *Numb* on a *Numblike* deficient background neither has impact on lung

development and maturation nor leads to any severe phenotypic abnormalities of the lung. In order to investigate potential functions of Numb and Numblike in the regeneration of respiratory epithelium, lung damage experiments were performed. A well-characterized and suitable model to study this is the bleomycin-induced damage of distal epithelial airway cells [62, 143-145]. The application of bleomycin (bleo) via the trachea leads to an inflammation of mouse lung distal alveolar compartments accompanied by a massive onset of fibrogenesis during regeneration, which is characterized by collagen deposition in the extracellular matrix of alveolar epithelial cells as well as by scar formation [146, 147]. In order to achieve a maximal challenge of dKO and Ctrl lungs, bleomycin was administered intratrachealy with sub lethal doses of 2.5 U/Kg, while dKO and Ctrl animals treated only with vehicle served as non-injured controls. Males at an age of 10 to 12 weeks were injured and analyzed 14 respectively 21 days after bleomycin application (Figure 11A).

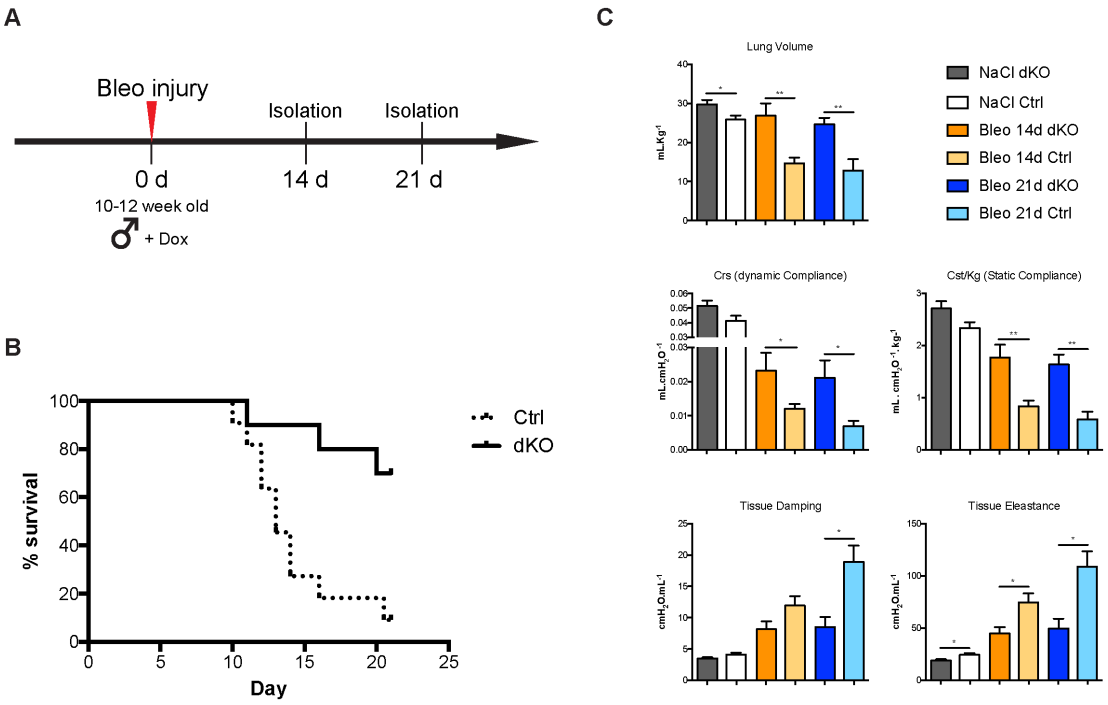

Figure 11: Enhanced survival of bleomycin treated Numb/Numblike deficient animals.
A: 10 to 12 week old males were treated with bleomycin with a dose of 2.5 U/kg at day 0 (0 d). **B:** Survival curve of bleomycin treated animals. Bleomycin challenged dKO animals (n = 10) showed a survival rate of about 70%. Ctrls (n = 11) died approximately 10 to 14 days after treatment. Curve comparison by Mantel-Cox test $p = 0.0028$. **C:** Compliance parameters of narcotized mice were measured with FlexiVent system 14 and 21 days after injury (14 d, 21 d). Subsequently, BAL fluid was taken from each lung followed by the isolation of both lung lobes. Total left lobe was used for histologigal analyses while right lobes were isolated to prepare either RNA or protein. n = 8 NaCl Ctrl, n = 7 NaCl dKO, n = 10 Bleo 14 d Ctrl, n = 6 Bleo 14 d dKO, n = 3 Bleo 21 d Ctrl and n = 5 Bleo 21 d dKO animals were analyzed. All graphs show mean ±SEM with $*p < 0.05$, $**p < 0.01$.

The most striking difference upon lung damage was a significantly improved survival of *Numb/Numblike* dKOs about 70 % after 21 days, while the majority of control mice died 15 days after injury (Figure 11B). In order to better characterize the degree of fibrotic lesion, lung compliance measurements of narcotized animals were performed 14 respectively 21 days after bleomycin and vehicle treatment (Figure 11C). Lung compliance parameters, which provided information about lung functionality in injured dKO and Ctrl mice, were assessed using flexiVent^{TM} analyzer. One of these parameters is represented by the lung volume, which reflects the inspiratory capacity of the lung in relation to body weight (ml/kg) [148, 149]. In patients with idiopathic pulmonary fibrosis (IPF) as well as in experimental lung fibrosis in mice, lung tissue is degenerated, stiff and less flexible due to excessive incorporation of extracellular matrix proteins into alveolar walls [69, 71]. Hence, inspiratory capacity decreases with an increased degree of lung fibrosis [150]. Accordingly, lung volume (ml/kg) of bleomycin treated Ctrl mice displayed a reduction by one half for both analyzed time points (Figure 11C; first graph). However, lung volume of treated dKOs remained relatively normal at 14 respectively 21 days. Moreover, the measurements revealed a slightly higher inspiratory capacity of non-injured NaCl treated dKO lungs compared to the non-injured Ctrls. Furthermore, dynamic and static compliance resemble parameters, which characterize the expansibility of the lung volume in relation to pressure [148-150]. According to degeneration and increased stiffness of fibrotic lungs, the volume and ease, by which these lungs can be extended at a constant pressure, is markedly reduced compared to healthy lungs. These volume alterations in relation to pressure are expressed by the dynamic compliance (Crs), which declines the more severe lungs are disrupted by fibrosis. Strikingly, the Crs (ml/cmH_2O) remained only moderately reduced in bleomycin treated dKO lungs reflecting a lower degree of fibrotic lung stiffness accompanied by better lung functionality. In contrast, injured Ctrl lungs displayed a dramatic reduction of volume per pressure ratios (Crs) by one half at 14 days and by two third at 21 days after bleomycin administration in comparison to treated dKOs indicating profound fibrotic injury in Ctrl animals (Figure 11C; second graph panel). In order to expand fibrotic lungs with the same volume of normal lungs, higher pressures are needed due to their stiffness. This static elastic recoil pressure of the lung at a given lung volume in relation to the body weight is reflected by the static compliance (Cst/kg), which declines like the Crs with an increased degree of fibrosis [150, 151]. In line with the previous Crs results, static

compliance values (ml/cmH_2O*kg) significantly sloped to a similar degree in fibrotic Ctrl lungs of about one half at 14 days and two third at 21 days after bleomycin treatment compared to treated dKOs. These displayed a static compliance with moderate reduction, similar to their Crs values, at both time points, which further argued for ameliorated fibrosis in dKO lungs. The previous compliance parameters directly revealed alterations in respiratory tissue mechanics of diseased lungs. In order to obtain more detailed insights into airway mechanics of injured lungs as well, tissue damping and elastance were analyzed in bleomycin treated and non-treated mice (Figure 11C; third graph panel). Tissue damping is related to the resistance of lung tissue and reflects the energy dissipation in the alveoli at increasing pressure in relation to the volume [148]. In healthy lungs lower energy (pressure) is dissipated from alveolar walls due to their higher elasticity compared to collagen enriched fibrotic alveoli. Thus, the more severe lungs are affected by fibrosis the more respiratory pressure is adsorbed by alveolar walls. Consequently, a higher pressure is needed to compensate this dissipative energy loss in order to maintain an appropriate lung volume. Respectively, bleomycin treated Ctrl mice depicted an increased tissue damping (cmH_2O/ml) of more than two-fold at 14 days and even about four-fold at 21 days after injury compared to NaCl treated Ctrls. In contrast, the pressure dissipation in alveoli of bleomycin treated Numb/Numblike dKOs was only elevated by two-fold at both stages compared to non-injured Ctrls, further arguing for milder fibrotic lung damage in these mice. Similar results were obtained for the tissue elastance, which is related to the elasticity of lung tissue describing the energy conservation in alveoli at a certain pressure in relation to the volume [148]. This parameter is closely coupled to tissue damping, since an increased dissipative behavior of distal airways due to fibrosis simultaneously compromises tissue elasticity of the alveoli. Hence, higher pressure is required to compensate for reduced elasticity in order to maintain a certain respiratory lung volume. Equivalent to this, bleomycin treated Ctrls compared to NaCl treated animals displayed a pressure per volume ratio (cmH_2O/ml) for the tissue elastance, which was three times higher at 14 days and even more than four times higher at 21 days after lung injury. This clearly reflected dramatically reduced tissue elasticity of the alveolar compartments as a result of excessive alveolar matrix protein deposition in these mice. Although the required respiratory airway pressure in bleomycin treated dKO lungs increased by twofold after 14 days compared to NaCl treated controls, tissue elastance did not further deteriorate 21 days after injury and

maintained at a similar level. However, the tissue elastance of treated dKOs remained significantly ameliorated for both time points compared to bleomycin treated Ctrl lungs. Strikingly, airway elasticity of *Numb/Numblike* dKO lungs after 21 days was even improved by one half compared to the strongly compromised tissue elastance in challenged Ctrl mice. Interestingly, non-injured dKO lungs revealed in terms of tissue elastance a slight but significant decrease of the required respiratory airway pressure compared to NaCl treated Ctrls, while both displayed no significant changes at the level of tissue damping. Hence, this suggested an enhanced elasticity of distal airways in lungs of non-injured *Numb/Numblike* dKO mice. Taken together, both parameters, the tissue damping and elastance, demonstrated that the alveolar airway mechanics were highly impaired 21 days after bleomycin injury underlining a severe fibrotic damage at this stage in treated Ctrl animals. In contrast, challenged *Numb/Numblike* dKO lungs displayed airway function that was similar for both time points suggesting that epithelial loss of Numb and Numblike is ameliorative for bleomycin-induced lung fibrosis in mice. Beyond that, this model might propose potential therapeutic targets for the human lung disease IPF, which is marked by similar abnormalities like enhanced production of extracellular matrix proteins at the level of respiratory airways compromising lung function. The underlying mechanisms that may lead to this amelioration were further elucidated in this work.

3.2.2 Epithelial Numb/Numblike depletion reduces expression of profibrotic markers during fibrogenesis

In order to further validate the observed compliance phenomena and to pinpoint the actual degree of fibrosis in the animals, bleomycin-injured and non-injured dKOs as well as Ctrls were characterized based on histological and molecular analysis. Bleomycin induced fibrosis in mice as well as IPF in humans are marked by elevated expression of profibrotic markers such as *Col1a1* or *Ctgf* accompanied by enhanced deposition of collagen into the extracellular matrix of distal lung cells [69-71]. Therefore, trichrome stainings of left lung lobe sections from animals treated with bleomycin or NaCl were performed to evaluate the degree of tissue disruption 21 days after lung injury (Figure 12A). Using this approach, massive accumulation of deposited collagen in the extracellular matrix of distal lung cells was observed 21 days after bleomycin (bleo) injury in Ctrl lungs, whereas the amount and size of collagen deposited spots in injured dKOs was significantly removed after 21 days in

comparison to bleo Ctrls. Besides the enlargement of fibrotic areas, bleo treated Ctrl lungs additionally displayed characteristic honeycomb formation of distal respiratory epithelium, a clear sign for end-stage pulmonary fibrosis [152], whereas these structures were less pronounced in bleo dKOs. In order to elucidate the actual degree of fibrosis, total lung sections were evaluated according to their amount of fibrotic foci per high power field from 0 (not fibrotic) to 7 (highly fibrotic). This unbiased fibrotic scoring (Figure 12C) further supported the histological data and clearly confirmed a significant reduction of fibrotic tissue areas in bleo treated dKOs compared to bleo Ctrl animals 21 days after lung damage. NaCl treated animals, both Ctrls and dKOs, did not reveal any lung structural disruptions, thus remained completely unaffected by the carrier treatment. Reduced deposition of collagen I (ColI) fibers in bleo treated dKO lungs was additionally confirmed by ultrastructural analysis comparing sections of bleo treated Ctrl and dKO animals with NaCl treated controls 21 days after treatment (Figure 12B). Collagen I fibers of bleo dKO lungs were smaller in size compared to bleo Ctrls whereas carrier treated lungs (NaCl Ctrl 21d) showed normal alveolar wall thickness without pro-fibrotic collagen deposition. Moreover, quantification of collagen content from whole lung homogenates was performed by SIRCOL assay (Figure 12E) comparing bleo injured and non-injured lungs. This assay detects all collagen forms, pro-fibrotic as well as non-fibrotic derivatives, and quantitative analysis of these total collagen contents in both bleo dKO and Ctrl lung homogenates displayed a significant increase by about two-fold after 14 days compared to collagen abundance in NaCl treated Ctrls. However, bleo dKOs revealed a significant decrease of collagen content compared to bleo Ctrls 21 days after injury supporting the previously observed histological results. Nevertheless, ameliorated collagen deposition in bleo dKO lungs was not fully restored to normal level detected in NaCl treated mice and remained slightly elevated in comparison to non-injured Ctrls at this time point. As expected, collagen deposition in whole lung homogenates of non-injured NaCl treated dKO mice was not affected. In order to unveil further molecular changes, mRNA expression analysis was performed for well-defined pro-fibrotic marker like collagen I (*Col1a1*), connective tissue growth factor (*Ctgf*), tumor necrosis factor alpha (*Tnf-alpha*) and alpha-smooth muscle actin (*Acta2*) (Figure 12D). In line with the reduced collagen content in bleo injured lung tissue of dKOs, relative *Col1a1* mRNA expression also revealed significant decrease to normal levels of NaCl Ctrls after 21 days whereas *Col1a1* expression remained 3-fold

upregulated at 14 days. However, bleo Ctrl lungs displayed nearly 3 times increased *Col1a1* mRNA expression level compared to non-injured Ctrls at both time points, 14 and 21 days post bleo injury (Figure 12D; *Col1a1*).

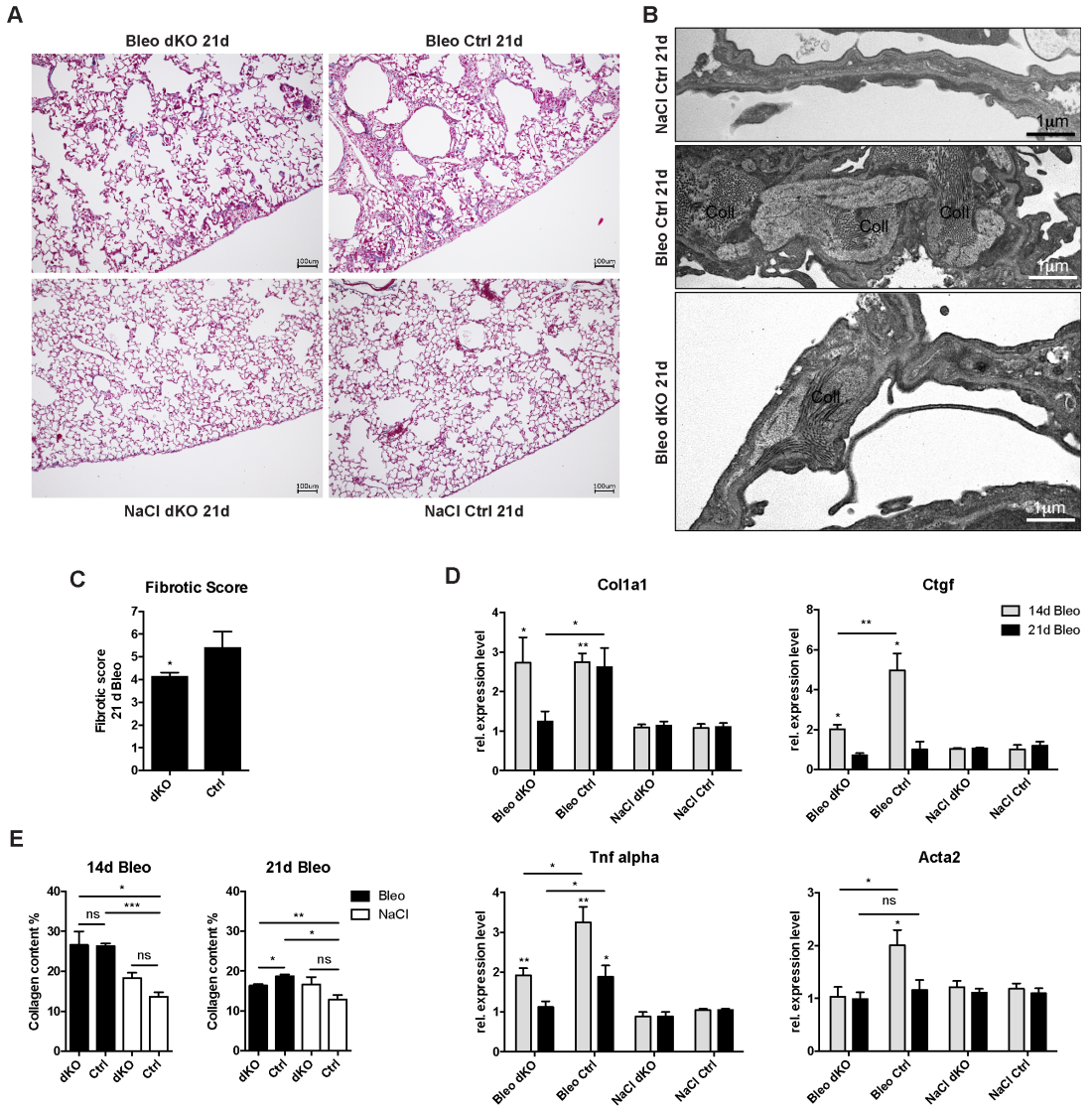

Figure 12: Reduced profibrotic markers in bleomycin treated dKO animals.
A: Trichrome staining of parafine sections (5 µm) of bleomycin injured dKO *vs*. Ctrl as well as NaCl controls at day 21 after treatment. Blue staining shows the profibrotic collagen deposition (fibrotic foci) in the lung periphery. Scale bars at 100 µm. **B:** Electron microscopic pictures of bleomycin treated animals at day 21 after injury showing collagen I fibers (ColI) deposited into the extracellular matrix of distal alveolar cells. Scale bar at 1 µm. **C:** Fibrotic score of bleomycin injured dKO (n=5) vs. Ctrl (n=3) animals 21 days post treatment. The degree of fibrosis was evaluated by analyzing randomly chosen trichrome stained tissue sections for each animal. According to the amount of fibrotic foci per high power fields of a whole lung section, values between 0 for non-fibrotic and 7 highly fibrotic tissue were assigned and averaged. **D:** Real time quantitative RNA expression level analysis of right lobe lung homogenates of bleomycin injured dKO (n=5) *vs*. Ctrl (n=3) as well as NaCl controls (n=3 each) at day 14 and 21 after treatment for profibrotic markers collagen I (*Col1a1*), connective tissue growth factor (*Ctgf*), tumor necrosis factor alpha (*Tnf-alpha*) and alpha-smooth muscle actin (*Acta2*). All are normalized to *Hprt*. **E:** SIRCOL assay of bleomycin injured dKO *vs*. Ctrl as well as NaCl controls at day 14 and 21 after treatment. Graphs show the percentage of collagen content of total lung homogenates under different conditions. All graphs are presented as mean ±SEM with $*p < 0.05$, $**p < 0.01$, $***p < 0.001$ and ns = not significant. Non-marked bars are as well considered as not significant compared to control.

Ctgf, a member of the CCN-family of secreted proteins, exhibits high expression during experimental lung fibrosis in mice and serves as a marker for lung fibrosis [62]. Strikingly, relative mRNA level of *Ctgf* in bleo dKOs revealed a moderate increase of only 2-fold compared to non-injured controls at day 14 post injury. In contrast, *Ctgf* displayed 5-fold higher relative mRNA level at this stage than NaCl treated control animals accounting for more than two times the *Ctgf* expression observed in bleo dKO lungs. However, expression of *Ctgf* was attenuated to a normal level in both bleomycin treated dKOs and Ctrls after 21 days. Non-injured (NaCl treated) dKO lungs expectedly did not reveal any altered *Ctgf* mRNA level compared to NaCl Ctrls. Analysis of *Tnf-alpha*, a pro-inflammatory cytokine upregulated in bleomycin-induced lung fibrosis and IPF [153], revealed only moderate increase of mRNA expression in bleo dKO lungs by 2-fold after 14 days, while mRNA level in bleo Ctrls was more than 3-fold higher compared to non-injured NaCl Ctrl animals at this time point. Furthermore, relative *Tnf-alpha* expression in bleo dKOs was fully restored after 21 days, whereas corresponding bleo Ctrls maintained a 2-fold higher mRNA level in comparison to NaCl Ctrls. Under non-injured (NaCl) conditions, dKOs exhibited no alterations in *Tnf-alpha* expression compared to Ctrls. In order to obtain insights into potential changes of fibroblast/myofibroblasts differentiation, which is another indication for lung fibrosis progression [76], *Acta2* mRNA expression levels were analyzed. The results clearly demonstrated that expression of *Acta2* in bleomycin treated (14 and 21 days) and NaCl treated *Numb/Numblike* dKOs remained unaffected. Exclusively, bleo Ctrl animal revealed a significant increase by 2-fold compared to NaCl Ctrls at 14 days post injury, but *Acta2* expression normalizes again after 21 days. In conclusion, these data supported the previous observations and suggested a considerable improvement of fibrosis in lung epithelial specific Numb and Numblike depleted animals after bleomycin injury.

3.2.3 Reduction of profibrotic Wnt/ß-Catenin downstream targets in lung epithelial Numb/Numblike dKO mice

Based on the reduced active ß-Catenin protein level and mislocalization in lung epithelium (Figure 9 and Figure 10) we concluded that Wnt/ß-Catenin signaling might be altered in non-injured dKOs. Since Wnt/ß-Catenin signaling has been previously implicated in pulmonary fibrosis [62, 72, 74], this signaling pathway was analyzed in lung epithelial specific Numb/Numblike dKOs to elucidate potential alterations under

normal and disease conditions. Apart from the reduced ß-Catenin protein level, relative *ß-Catenin* mRNA expression in non-injured adult dKO lungs remained unchanged in comparison to mRNA levels of Ctrls (Figure 13B). In order to shed light on the impact of declined active ß-Catenin regarding Wnt-signaling in dKO lungs, additional qPCR based expression analysis of well-defined Wnt-downstream target genes was performed in lung homogenates of bleomycin and NaCl treated dKO mice. All relative mRNA expression levels that are depicted in the graphs below (Figure 13A) and were normalized to the relative expression levels of NaCl treated Ctrls (fold change = 1).

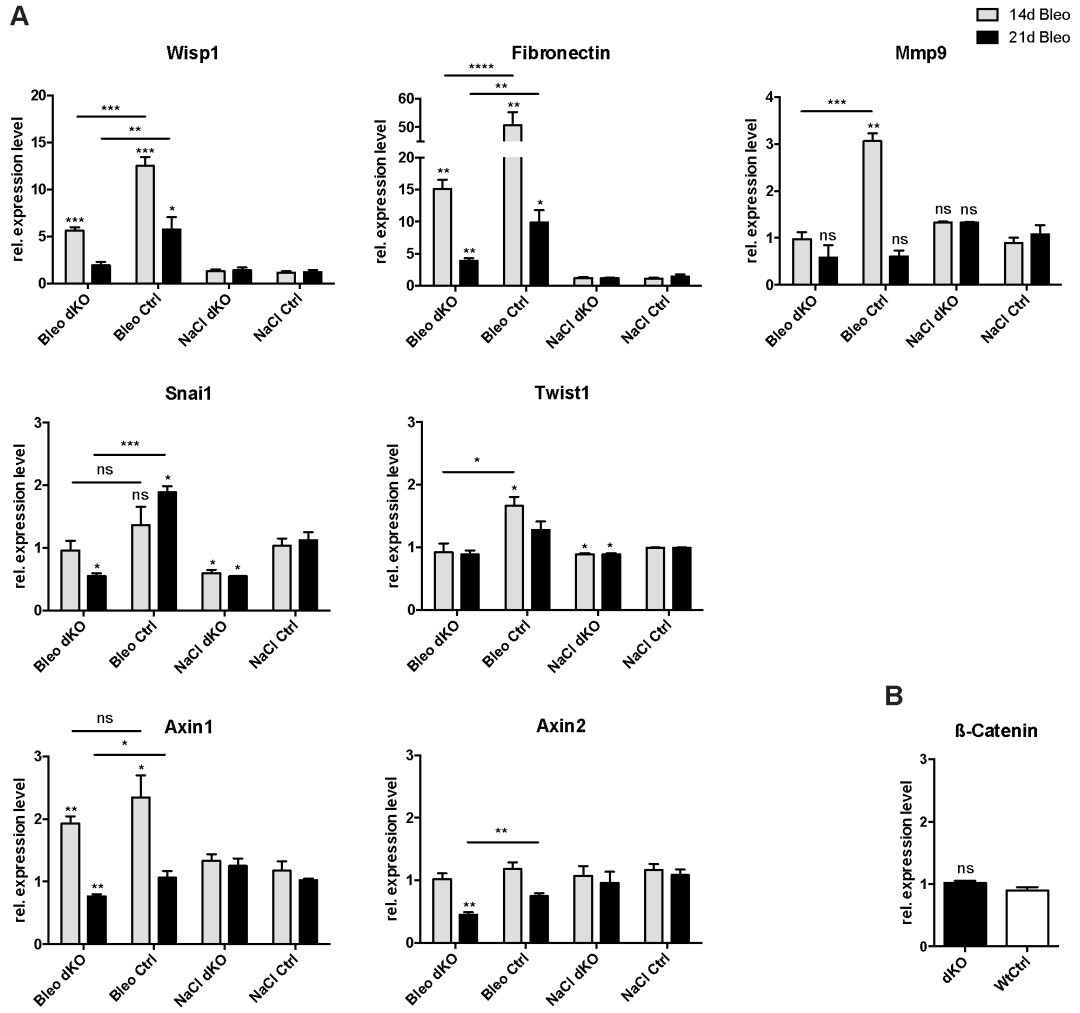

Figure 13: Wnt target gene expression of bleo injured and non-injured dKO vs. Ctrl lungs.
A: Relative mRNA expression analysis of Wnt/ß-Catenin signaling target genes *Wisp1*, *Fn1*, *Mmp9*, *Snai1*, *Twist1*, *Axin2* and *Axin2* of bleo injured (14 and 21 days) vs. vehicle treated dKO (n=3) vs Ctrl (n=3) lungs. Animals used for experiments in average n=5 to n=3 for all conditions. B: Relative mRNA level of *ß-Catenin* of uninjured lungs (n=3 each). All normalized to *Hprt*. All graphs are presented as mean ±SEM with **p* < 0.05, ***p* < 0.01, ****p* < 0.001, ****p < 0.0001 and ns = not significant. Bars without asterisc are also considered as not significantly altered compared to control.

Wnt1-inducible signaling protein-1 (*Wisp1*/*CCN4*) is one of the targets, which has also been previously linked to pulmonary fibrosis and belongs like Ctgf (*CCN2*) to the CCN-family of matricellular proteins [62]. *Wisp1* exhibits a high expression level in bleomycin-induced murine lung fibrosis model as well as in patients with idiopathic pulmonary fibrosis (IPF). Highly increased *Wisp1* mRNA expression in bleomycin-injured Ctrl lungs was confirmed in this study at 14 days after treatment by an approximately 13-fold upregulation. Strikingly, the expression level of *Wisp1* in damaged dKO lungs was reduced by more than one half (5,627 ± 0,3674, n=5) compared to bleo Ctrls at this time point. Remarkably, *Wisp1* level of bleo treated dKOs was restored to normal expression 21 days post injury, while the relative mRNA level of *Wisp1* in bleo Ctrls remained significantly elevated. It is worth mentioning that *Wisp1* expression in whole lung homogenates of vehicle (NaCl) treated dKOs was not altered. The matrix metalloprotease Mmp9, another Wnt-signaling downstream target and profibrotic marker [154], was significantly upregulated 3-fold in bleo treated Ctrl mice after 14 days whereas *Mmp9* in bleo treated dKOs remained at a normal level. 21 days after bleo treatment, normal *Mmp9* expression in dKOs was still maintained whereas the mRNA level in Ctrls was reconstituted to normal expression. However, the most dramatic changes were identified in expression of the Wnt target *Fibronectin1* (*Fn1*) [155], which displayed a 50-fold increase in bleo treated Ctrl mice at 14 days whereas bleo treated dKOs revealed a 15-fold upregulation of *Fn1*. The relative *Fn1* expression in bleo dKOs decreased to less than 4-fold after 21 days whereas corresponding bleo treated Ctrls maintained a 10-fold increased *Fn1* mRNA level. Hence, a significant difference between the *Fn1* expression levels of both treated mouse groups was observed for each time point. Furthermore, no significant alteration of *Fn1* expression was detected in the lungs of vehicle treated dKO animals. Moreover, Wnt/ß-catenin targets involved in EMT processes, which are believed to be a potential source of pulmonary fibrosis as mentioned above [76], were checked. One of these targets that play a crucial role in EMT is *Snai1* (also: *Snail*) [79]. Strikingly, *Snai1* revealed already a significant lower relative mRNA expression level in non-injured NaCl treated dKOs by almost one half (0,5999 ± 0,05153, n=3). Additionally, *Snai1* level increased only moderately during lung fibrosis progression in bleo treated dKOs to an expression level comparable with NaCl treated Ctrls after 14 days and decreased after 21 days to a similar level observed in the NaCl treated dKOs. *Snai1* expression in bleo treated

Ctrl lungs did not change significantly after 14 days but displayed 2-fold increased level 21 days post injury. Comparable to *Snai1*, the EMT marker and Wnt/ß-Catenin target gene *Twist1* [78] displayed also a significant decrease of mRNA level in non-injured NaCl treated dKO lungs. However, bleomycin treatment of dKOs revealed normal expression of *Twist1* 14 respectively 21 days post injury. In contrast, bleomycin treated Ctrl animals exhibited significantly higher *Twist1* expression after 14 days compared to corresponding bleo treated dKOs but this level was restored to normal after 21 days. Wnt/ß-Catenin target genes like *Axin1* and *Axin2* [156] demonstrated significantly decreased expression in dKO animals 21 days after fibrosis induction. Moreover, similar extents of induction (about 2- to 2.5-fold) were observed for *Axin1* expression in bleo treated dKO and Ctrl lungs after 14 days, while *Axin2* expression stayed at normal levels under all other conditions. In summary, these data provided further evidence for the impairment of Wnt/ß-catenin signaling in Numb/Numblike dKOs resulting in the inhibition of Wnt-downstream gene expression. Thereby, reduced profibrotic signals under non-injured conditions as well as upon bleomycin treatment suggested an amelioration of fibrosis in mice lacking Numb and Numblike specifically in lung epithelium.

3.3 Mechanistic studies on the role of Numb/Numblike in Mouse Lung Epithelial cells MLE12

In order to elucidate underlying mechanisms explaining the disruption of epithelial cell polarity and integrity as well as decreased fibrosis under pathological conditions in lung epithelial Numb and Numblike dKOs, *in vitro* experiments were performed using the mouse lung epithelial derived MLE12 cell line. These cells provide a perfect *in vitro* system for analyzing Numb and Numblike in lung epithelial cells and complementing the *in vivo* system. Therefore, silencing of *Numb* and *Numblike* in MLE12 cells mediated by shRNAs was conducted to examine changes that accompany *Numb*/*Numblike* inactivation by IHC, Western blot and RT-PCR analysis. Further mechanistic characterization of molecular alterations was promoted by additional screening for novel Numb and Numblike interaction partners based on GFP-tagged Numb and Numblike overexpressing MLE12 cells.

3.3.1 Mislocalization of E-Cadherin and ß-Catenin in Numb and Numblike double knockdown MLE12 cells

Towards the establishment of an *in vitro* system resembling the *in vivo* situation of epithelial specific Numb and Numblike depletion in lung, small hairpin RNA (shRNA) directed against *Numb* (shNb) and *Numblike* (shNbL) were utilized to generate a *Numb*/*Numblike* double knockdown (dKD) in MLE12 cells. These viral transduced and puromycin selected stable dKD cells were initially tested for Numb/Numblike inactivation efficiency. The analysis of *Numb*/*Numblike* mRNA expression levels as well as Numb and Numblike protein abundance clearly showed a highly efficient dKD of both genes in the stable transduced cell lines (Figure 14A, B). This was further validated by Numb and Numblike immunostainings of fixed *Numb*/*Numblike* dKD cells in comparison to *shScramble* (shScr) control cells (Figure 14C, D). Positive Numb antibody staining was mainly detected at the lateral membrane of contacting shScr cells as well as in cytosolic vesicle-like speckles, which couldn't be detected in *Numb*/*Numblike* dKD cells. Additionally, Numblike antibody staining clearly displayed cytosolic localization in shScr MLE12 control cells whereas dKD cells were negative for Numblike signal indicating an efficient depletion (Figure 14D). Previous studies demonstrated that silencing of *Numb* expression in the polarized Mardin Darby Kidney cell line (MDCKII) results in mislocalization of the adherens junction protein E-cadherin indicating a loss of polarity in these epithelial cells [10]. Strikingly, co-immunofluorescence stainings for Numb and Numblike in combination with E-Cadherin revealed the same mislocalization phenomenon in *Numb*/*Numblike* dKD MLE12 cells. Furthermore, it has been shown that mislocalisation of E-Cadherin in epithelial cells mediated by a loss of Numb additionally results in mislocalization of ß-Catenin [10]. In order to determine a potential ß-Catenin mislocalization in *Numb*/*Numblike* dKD cells, co-immunofluorescence stainings for ß-Catenin and E-Cadherin were performed. Concomitant with the alteration of E-Cadherin localization, dKD cells exhibited changes in the subcellular localization of ß-Catenin from the lateral membrane to apical parts. In comparison to shScr control cells, which displayed a prominent co-localization of ß-Catenin and E-Cadherin at the membranes of contacting cells typical for epithelial cells [10], ß-Catenin staining in *Numb*/*Numblike* dKD cells appeared weaker (Figure 14E). These results indicated that a loss of Numb and Numblike

mediates the subcellular translocation of adherens junction proteins and thereby disrupts epithelial cell polarity.

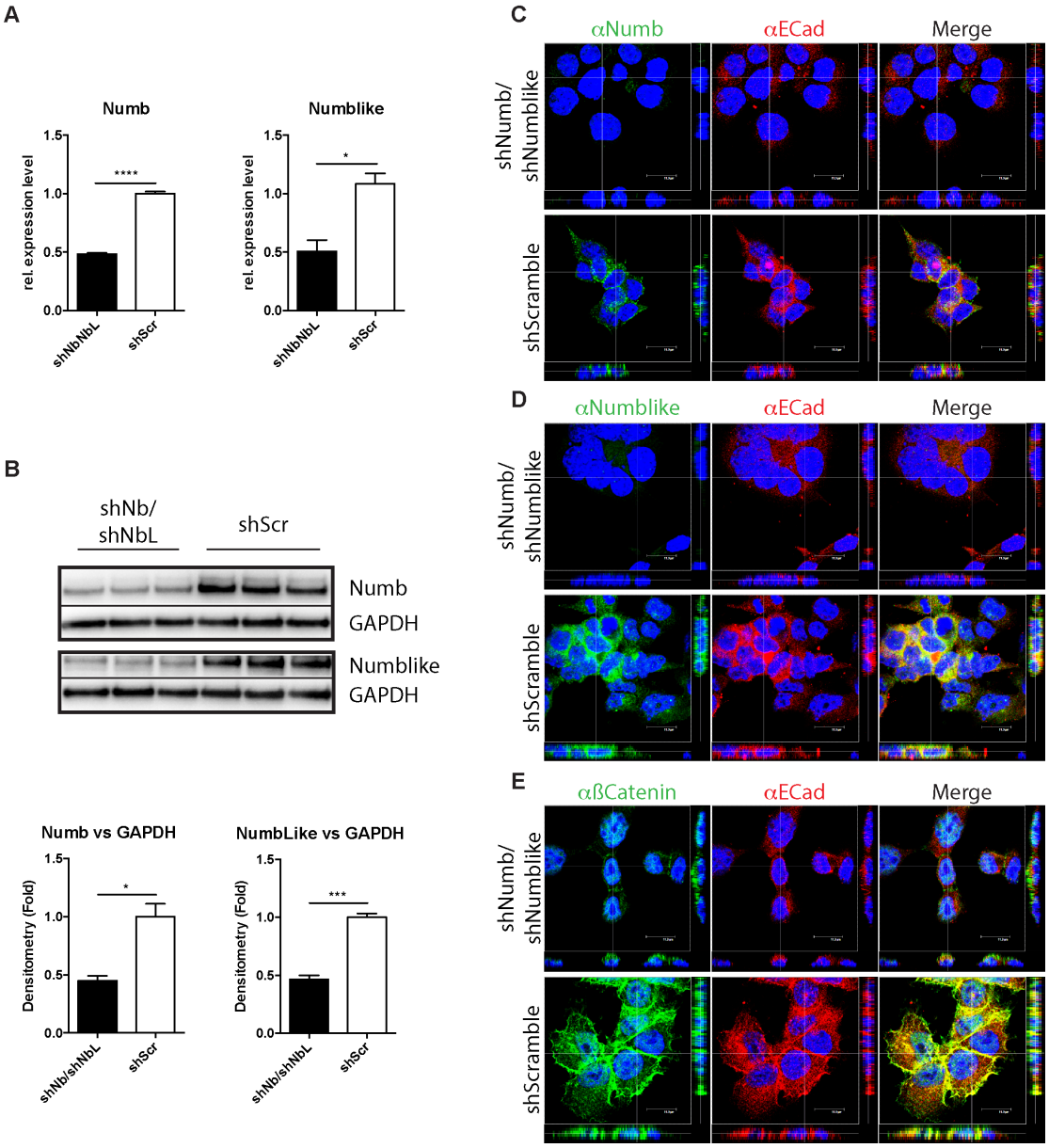

Figure 14: Mislocalization of E-Cadherin and ß-Catenin in shNumb/shNumblike double knockdown MLE12 cells.

A: Relative mRNA expression levels of Taq Man Assays for *Numb* and *Numblike* indicating *shNumb*/*shNumblike* KD efficiency in MLE12 cells. B: Western Blot analysis including quantitative densitometry (normalization vs. GAPDH) of the protein levels for Numb and Numblike confirming decreased Numb and Numblike in shNb/shNbL MLE12 cells. All graphs show mean ±SEM with $*p < 0.05$, $***p < 0.001$ and $****p < 0.0001$. C-E: Immunostaining of fixed shNb/shNbL vs. shScr MLE12 cells for Numb and E-Cadherin (C), Numblike and E-Cadherin (D) as well as ß-Catenin and E-Cadherin (E) displaying reduction of Numb and Numblike abundance in shNb/shNbL cells accompanied by mislocalization of E-Cadherin and ß-Catenin. Nuclear staining with DAPI (blue). Pictures were acquired by CLSM as z-stacks and depicted as cross-sections with x/y, x/z, y/z projection. Digital zoom of 63x magnification with scale bar at 12µm. Randomly chosen representative images of n=3 different cell vials for each condition that were fixed and stained on cover slips (24-well plate) are shown.

3.3.2 Disruption of WNT/ß-Catenin signaling in Numb/Numblike dKD MLE12 cells

The previous results demonstrated aberrant subcellular localization of the adherens junction proteins E-Cadherin and ß-Catenin in Numb and Numblike depleted lung epithelial cells *in vivo* and *in vitro*. Further protein analysis by Western blot was performed to quantify alterations of ß-Catenin and E-Cadherin abundance mediated by *Numb*/*Numblike* dKD. Densitometry analysis revealed that total (pan-) as well as non-phosphorylated active ß-Catenin was significantly reduced by one half (Figure 15A) in dKD cells, which reflected the diminished ß-Catenin staining observed in these cells (Figure 14E), whereas E-Cadherin abundance (data not shown) in dKD cells was not altered. It is important to note that ß-Catenin acts not only as a component of the adherence junction complex but also exerts its function directly in Wnt-signal transduction. The cytosolic protein level of ß-Catenin is thereby negatively regulated by GSK-3ß [43], which mediates ß-Catenin phosphorylation and its subsequent targeting to the proteosomal degradation pathway under normal conditions [43, 157, 158]. In this respect, inhibition of GSK-3ß by the chemical compounds LiCl and SB216763, which promote activation of WNT/ß-Catenin signaling [159, 160], was conducted in shScr and KD cells in order to elucidate a GSK-3ß dependent loss of ß-Catenin abundance in Numb and Numblike depleted epithelial cells (Figure 15B). MG132 treatment of the cells served as a positive control in order to block total proteasomal degradation [161, 162]. In general, Western blot and consequent densitometry analysis revealed that initial low ß-Catenin levels were restored in dKD cells by the treatment with GSK-3ß inhibitors after 4 hours (Figure 15B). Nevertheless, GSK-3ß inhibition displayed differences in the amounts of attenuated active and total (pan-) ß-Catenin protein. Total ß-Catenin level in *Numb*/*Numblike* dKD cells was increased by more than 2-fold, similar to the treated shScr controls after 4h of incubation with LiCl (20 mM) and SB216763 (30 µM). Expectedly, MG132 (10 µM) treatment displayed an effective block of proteasomal degradation in dKD and control cells reflected by increased total ß-Catenin protein levels. Furthermore, also active ß-Catenin protein abundance in GSK-3ß inhibitor and MG132 treated dKD cells was restored to normal levels. Moreover, all compound-treated control cells displayed a two-fold increased active ß-Catenin protein level.

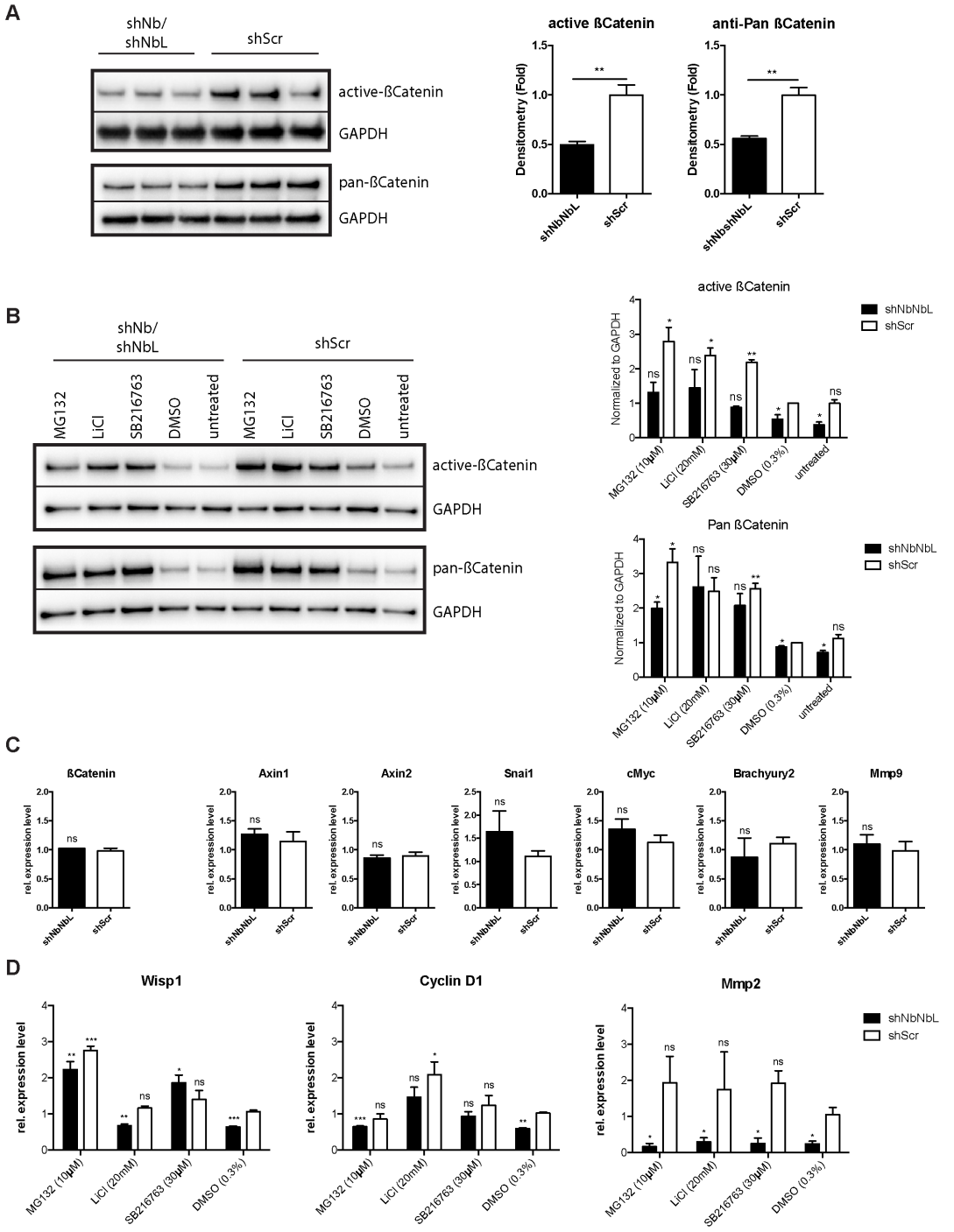

Figure 15: Disruption of WNT/ß-Catenin signaling in shNb/NbL KD MLE12 cells
A: Western blot analysis of non-phosphorylated (active) ß-Catenin and total (pan-) ß-Catenin. Relative quantification of protein by densitometry (n=3). Normalization to GAPDH. **B, D:** GSK-3ß inhibition experiment. shNb/shNbL and shScr MLE12 cells were cultured in D-MEM/F-12 (1:1) (1X)/10% FCS/ 1% PSG in a 6-well plate 24 h before they were treated with chemical compounds. 20 mM LiCl and 30 µM SB216763 were then supplemented to the culture medium and cells were incubated 4h at 37°C to inhibit GSK-3ß activity. In order to block proteasomal degradation, cells were cultured in medium containing 10µM MG132 serving as positiv control. As negative control cells were cultured in medium supplemented either with 0.3 % DMSO or without DMSO (untreated). To elucidate the effect of GSK-3ß inhibition, either protein levels of active and pan-ß-Catenin were analyzed by Western blot and quantified by densitometry normalized to GAPDH (n=2; B) or relative mRNA expression analysis was determined by TaqMan assays (n=3) vs. *Hprt* for ß-catenin, Axin1, Axin2, Snai1, cMyc, Brachyury2, Mmp9 (only untreated cells; **C**) as well as Wisp1, Cyclin-d1 and Mmp2 (treated cells; D). All graphs show mean ±SEM with *$p < 0.05$, ***$p < 0.001$ and ***$p < 0.001$.

Similar to the *in vivo* studies, relative mRNA expression levels of Wnt-downstream target genes were analyzed to pinpoint effects of reduced ß-Catenin protein in dKD cells (Figure 15C, D). Expression level of *ß-Catenin* mRNA remained unaffected in dKD cells compared to controls indicating that ß-Catenin is exclusively regulated on the protein level (Figure 15C). Surprisingly, no expression alterations were detected for the Wnt-target genes *Axin1*, *Axin2*, *Snai1*, *cMyc*, *Brachyury2* or *Mmp9* in dKD cells in comparison to controls. However, dKD cells revealed reduced mRNA expression levels for *Wisp1*, *Cyclin-d1* and *Mmp2* compared to shScr cells (vehicle treated cells Figure 15D). Moreover, expression of the target genes *Wisp1* and *Cyclin-d1* was rescued after 4h treatment with the GSK-3ß inhibitor SB216763 (30 µM) and displayed mRNA levels similar to controls. *Wisp1* expression in *Numb*/*Numblike* KD cells was approximately 2-fold higher compared to control shScr cultured in medium containing 0.3 % DMSO. Incubation with 20 mM LiCl did not restore low *Wisp1* expression levels in dKD cells, whereas *Cyclin d1* expression displayed amelioration similar to SB216763 treatment. MG132 control treatment (10 µM) had a strong effect elevating *Wisp1* expression level more than two-fold in dKD and shScr cells. In contrast, *Cyclin-d1* expression remained unaffected in MG132 treated dKD cells as well as shScr cells, resembling endogenous expression levels of DMSO treated controls. Surprisingly, dKD cells maintained significantly low *Mmp2* expression levels despite of their treatment with inhibitors. In summary these results clearly indicate that the previously observed mislocalization of ß-Catenin in cells lacking Numb and Numblike is accompanied by a GSK-3ß dependent decrease of total and active ß-Catenin protein levels, which finally results in the inhibition of a subset of Wnt/ß-Catenin downstream genes.

3.3.3 Screening for novel Numb/Numblike interacting proteins

Numb is an adaptor protein involved in multiple biological and cellular processes [163] like endocytosis [164, 165], endosomal trafficking [9], proteosomal degradation [8, 166] as well as inhibition of the Notch signaling pathway [2, 5, 167]. Thereby, Numb has been shown to interact with numerous proteins promoting their functions during these processes. Another important role of Numb is the establishment and stabilization of cell-cell contacts mediating polarity in epithelial cells [10]. In this respect, Numb has been previously described to directly associate with E-Cadherin facilitating the subcellular localization of the adherens junction protein to lateral parts

of epithelial cell membranes, which was also confirmed in this study *in vitro* and *in vivo* (Figure 8, Figure 14). In contrast, Numblike, the cytosolic Numb homolog, is only poorly characterized. In order to gain more detailed information about potential binding partners of both Numb and Numblike, epithelial MLE12 cells were lentivirally transduced, overexpressing human Numb isoforms 1 to 4 as well as human Numblike C-terminally fused to GFP, and thereafter utilized for co-immunoprecipitation (Co-IP) of interacting proteins. Hence, this cellular system provided an optimal tool to screen for isoform-specific co-enrichment of proteins. Anti-GFP-immunoprecipitation (IP) for each of the baits in triplicates, separation by SDS-PAGE, and gel extraction of the fractioned proteins was performed. Subsequently, proteins were digested into peptides and subjected to mass spectrometry (MS) analysis and label-free quantification by MaxQuant software. Bait proteins as well as potential interactors were characterized by quantitative co-enrichment given by their intensity profiles across the triplicates [168, 169]. In order to obtain quantitative protein ratios, normalized intensities of enriched proteins for Numb1-4:GFP and Numblike:GFP were compared to normalized intensities of proteins that were detected in lysates of GFP expressing control MLE12 cells (GFP Ctrl). Label-free IPs were validated according to the *p*-value resulting from a standard 'equal group variance' *t*-test of the observed protein intensity *fold changes* (FC) between IP fractions derived from bait overexpression and GFP-control cell lines [169]. Calculated *fold changes* were plotted against the negative logarithmic *p*-value of the *t*-test resulting in volcano plots (Figure 16A-E). Proteins with a high *fold change* and a high –log10 *p*-value were considered as significant interaction partners [169]. In order to set thresholds defining detected proteins as potential interaction partners, a significance line was calculated by Perseus software with $p < 0.05$ and FC > 2 (blue). Proteins below this threshold were either background binding proteins or false positives. Background binding proteins (grey) are characterized by a ratio of about 1:1 and located in vicinity to the y-axis and 0 in the volcano plots, whereas false positive candidates (red) display significant ratios with a *fold change* FC < 0.5 indicating an enrichment of proteins in IPs of GFP-control cells. The total numbers of proteins, which were detected in each IP with a *p*-value resulting from the t-test validation of the triplicates, are displayed in Figure 16F combined with the corresponding percentages and numbers of common specific interactions in contrast to the background and false positive proteins.

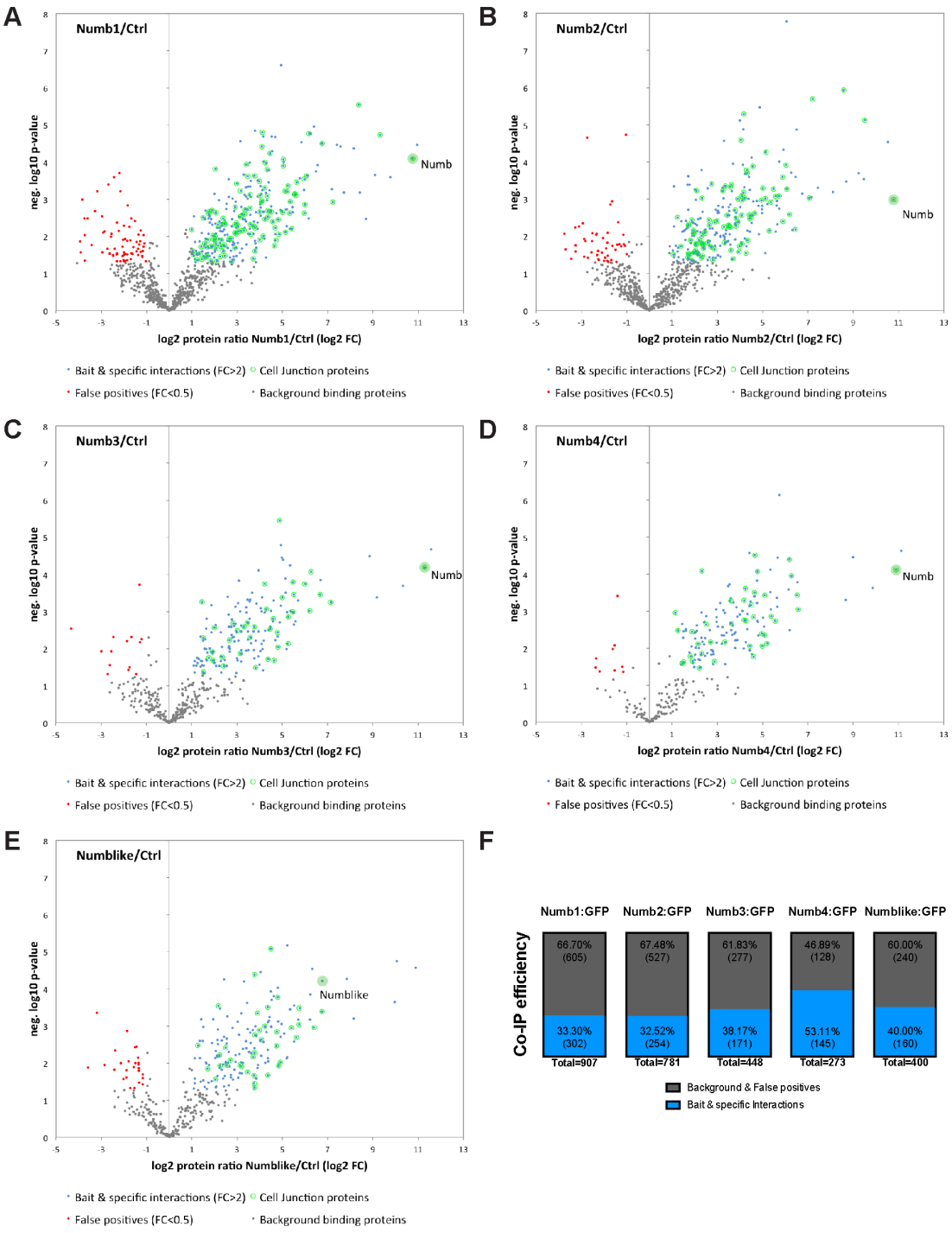

Figure 16: Mass spectrometric analysis and screening for novel Numb/Numblike interactors.
A-E: Determination of potential Numb and Numblike interacting proteins. Triplicates of label-free IPs from Numb1-4:GFP, Numblike:GFP and GFP control overexpressing MLE12 cells were validated based on a t-test of the ratios between the protein intensities in Numb-isoform respectively Numblike overexpression and GFP-control cells. *Fold changes* (log2 protein ratios) were plotted against -log10 *p*-values of the t-test and visualized as volcano plots. Proteins with high *fold change* and *p*-value (FC>2; $p<0.05$) were considered as true candidates including the baits (blue). Proteins below this threshold were considered as background binding proteins (FC<2; grey) and false positives (FC<0.5; red). Proteins highlighted in blue and green represented potential interaction candidates related to cellular components of cell junctions (GO-term analysis). **F:** Percentage of all potential interacting proteins for each of the baits in relation to overall IP detected proteins (total) with a p-value (Co-IP efficiency).

In general, the Co-IP efficiency calculated by the percentages of potential interaction partners for each individual IP varied in a range of about 30 to 50 percent of total detected proteins (Figure 16F). In order to better characterize and narrow down potential interaction candidates, GOrilla gene ontology enrichment analysis [170, 171] was performed for detected interacting proteins in relation to the corresponding background binding events. Interestingly, analysis of the interacting protein groups by cellular components, selected and compiled according to the *p*-values of their GO-term enrichment, revealed a broad cellular components diversity for Numb1:GFP and Numb2:GFP Co-IPs. In contrast, Numb3:GFP, Numb4:GFP and Numblike:GFP Co-IPs were related to lower amounts of significantly enriched cellular components with smaller cohorts of protein groups (Figure 17A-E). The results of this GO-term analysis revealed protein clusters related to cellular components of the cell junctions, ribonucleoprotein complexes and cytosolic parts (cytoplasmatic proteins) representing components with highly significant GO-term enrichment for all Numb isoforms and Numblike. Expectedly, a subset of previously reported Numb interaction partners was detected in all Numb isoform IP fractions with high and significant ratios (Table 40), e.g. proteins of the endocytic trafficking machinery like Clathrin (*Cltc*), AP-1 (i.e. subunit ß1; *Ap1b1*) and AP-2 complex subunits (i.e. alpha-adaptin; *Ap2a1*) [9, 164, 165]. Moreover, Numb is involved in cell migratory processes and has been previously described to interact with Integrin-ß1 (*Itgb1*) as well [110], which was significantly enriched in an isoform specific manner for Numb1:GFP, Numb2:GFP as well as Numblike:GFP Co-IPs (Table 40). The detection of these known Numb interacting proteins additionally underlines the efficiency and specificity of the performed IPs. The present study supported previous findings that Numb and Numblike concomitantly mediate lung epithelial integrity *in vivo* by controlling the subcellular localization of adherens junction proteins like E-Cadherin and ß-Catenin. Although the mechanism remains still unclear this phenotype was validated in lung epithelial cell lines. Hence, in order to elucidate the underlying mechanism promoting these processes, characterization of potential interacting proteins was focused on those protein groups that were annotated by GO-term analysis as cellular components of cell junctions. This cohort revealed as previously mentioned high *p*-values in the GO-term enrichment analysis (Figure 17A-E). The percentage of these cell junction proteins in relation to the total amounts of detected interacting candidates for each bait is displayed by the bar diagram in Figure 17F and corresponding proteins are

highlighted with blue and green dots on the volcano plots (Figure 16). The results demonstrated that the amounts of cell junction proteins in relation to total interactions were detected with lower abundance for Numb3 (39 proteins; 22.8%), Numb4 (40 proteins; 27.6%) and Numblike (37 proteins; 23.1%), compared to Numb1 (116 proteins; 38.1%) and Numb2 (96 proteins; 37.3%). For the latter two, cell junction related candidates were identified in cohorts of approximately 40 percent compared to all potential interacting proteins (Figure 16A-E, Figure 17).

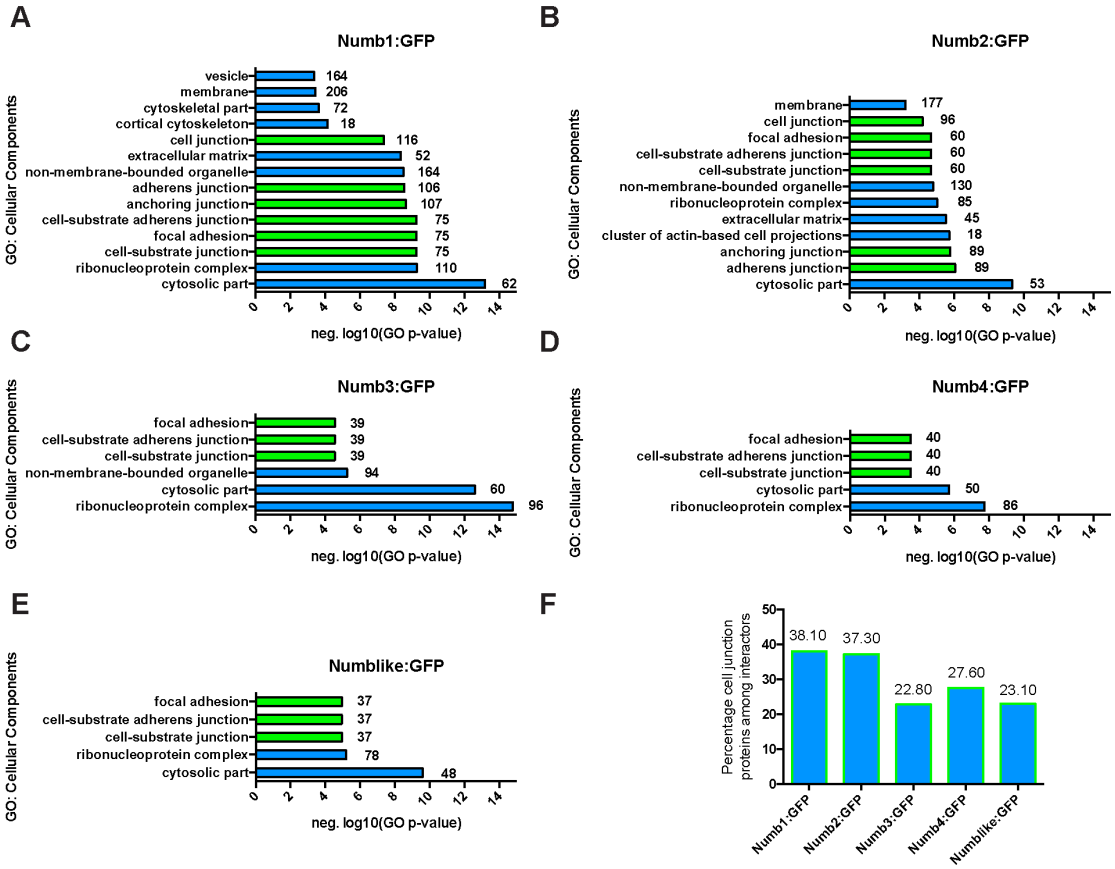

Figure 17: Analysis of GO-term enrichment for Numb/Numblike interacting proteins.
A-E: Compilation of protein subsets related to their cellular components determined by GO-term enrichment analysis. Cellular components were selected and presented according to their significances of enrichment ($p<10^{-3}$). Negative logarithmic *p*-values were plotted on the x-axis. Numbers at the right end of the bars represent the detected proteins in each cellular component. Components that were related to cell junctional components were highlighted in green. **F:** Percentage of proteins related to cell junctions relative to the total number of detected potential interaction candidates for each IP.

Proteins like Vinculin (*Vcl*) as well as some Arp2/3 complex subunits (*Arpc1b*, *Arpc4*, *Arpc5*) represent candidates belonging to the subset of cell junction proteins shared exclusively by Numb1 and Numb2 but not by Numb3, Numb4 and Numblike (Table 40). These proteins are involved in stabilization of adherens junctions linking cytoskeletal F-actin to proteins of the junction complex. Vinculin can thereby directly

interact with F-actin, ß-Catenin and Cortactin [172]. Strikingly, Cortactin (*Cttn*) was also significantly enriched in the Numb1:GFP IPs (Table 40). Moreover, MS analysis revealed a significant enrichment of serine/threonine kinase CK2 alpha and beta subunits (Casein kinase II, *Csnk2a1*/*a2*, *Csnk2b*), which was specifically enriched in Numb1:GFP, Numb2:GFP and also Numblike:GFP but not in Numb3:GFP and Numb4:GFP. CK2 has been shown to phosphorylate E-Cadherin and ß-Catenin stabilizing their interactions in the adherens junction complex [173, 174]. Additionally, CK2 can phosphorylate Histone deacetylase 6 (HDAC6), a known interaction partner of Cortactin [175], thereby promoting its deacetylase activity [176]. Furthermore, CK2 has been enrolled in the negative regulation of EMT processes by synergistically acting with GSK-3ß [177]. Taken together, these findings clearly demonstrated the abundance of novel potential interaction partners for Numb and Numblike including a certain subset of proteins with cell junction related functions. In order to validate the identified potential novel interaction partners in the context of the four different Numb isoforms and also their specificity, reciprocal co-immunoprecipitation in combination with Western blot analysis was conducted comparatively for Numb1-4:GFP and Numblike:GFP overexpressing cell lines. The corresponding results are described in the following part.

Gene names	p-value Numb1/Ctrl	Protein ratio Numb1/Ctrl (log2)	p-value Numb2/Ctrl	Protein ratio Numb2/Ctrl (log2)	p-value Numb3/Ctrl	Protein ratio Numb3/Ctrl (log2)	p-value Numb4/Ctrl	Protein ratio Numb4/Ctrl (log2)	p-value Numblike/Ctrl	Protein ratio Numblike/Ctrl (log2)
Ap2b1	33,8E-6	10,94	28,8E-6	10,54	20,9E-6	11,57	23,2E-6	11,12	26,9E-6	10,89
Ap2a2	252,6E-6	9,77	287,4E-6	9,47	206,0E-6	10,35	231,3E-6	9,86	224,9E-6	9,95
Ap2a1	656,5E-6	8,43	647,2E-6	8,10	420,5E-6	9,19	494,7E-6	8,67	628,5E-6	8,15
Ap1b1	232,7E-6	6,12	254,7E-6	6,46	138,7E-6	6,70	165,4E-6	6,54	142,4E-6	6,24
Ap2s1	2,3E-3	5,47	1,8E-3	5,72	6,0E-3	4,71	2,6E-3	5,06	2,7E-3	5,51
Cltc	1,2E-3	5,35	850,9E-6	5,57	-	-	-	-	-	-
Csnk2a1	15,3E-3	3,81	14,6E-3	4,05	-	-	-	-	-	-
Csnk2b	3,0E-3	3,08	2,1E-3	3,52	-	-	-	-	5,1E-3	2,63
Actr2	7,4E-3	3,04	2,7E-3	3,43	-	-	-	-	-	-
Arpc4	15,1E-3	3,04	2,3E-3	3,82	-	-	-	-	-	-
Arpc1b	3,3E-3	2,38	445,1E-6	3,35	-	-	-	-	-	-
Arpc3	15,8E-3	2,06	-	-	-	-	-	-	-	-
Arpc2	-	-	19,5E-3	2,72	-	-	-	-	-	-
Cttn	12,4E-3	1,71	-	-	-	-	-	-	-	-
Arpc5	33,9E-3	1,68	4,8E-3	1,73	-	-	-	-	-	-
Vcl	15,3E-3	1,57	7,0E-3	1,95	-	-	-	-	-	-
Itgb1	6,5E-3	1,00	3,1E-3	1,25	-	-	-	-	3,3E-3	1,27
Csnk2a2	26,2E-3	0,92	413,0E-6	1,68	-	-	-	-	7,5E-3	1,13

Table 40: Selected list of Numb and Numblike interacting proteins.
The list represents a selection of proteins that depicted high and significant protein ratios originating from the label-free MS analysis of the in triplicates performed GFP-IP experiments. The table indicates the differences in the abundance of potential interaction candidates for the four Numb isoforms and Numblike displayed by their gene names.

3.3.4 Cortactin and CK2, novel Numb/Numblike interaction partners

Mass spectrometry analysis of the GFP-IP experiments for Numb1-4:GFP and Numblike:GFP revealed bulks of potential interaction partners for all Numb isoforms and Numbilke. Two significantly enriched candidates, Cortactin and CK2, arose our interest because both proteins are involved in controlling adherens junction stability and cytoskeleton binding. In order to gather more detailed knowledge about novel potential cross talks of these candidates with Numb or Numblike and to validate the MS results, reciprocal Co-IP experiments were performed for all GFP fusion proteins and for Cortactin as well as CK2-alpha vice versa (Figure 18). GFP-IP of protein lysates from Numb1-4:GFP and Numblike:GFP overexpressing MLE12 cells and subsequent Western blot analysis strikingly revealed co-immunoprecipitation of endogenous Cortactin in all Numb isoforms and Numblike, whereas it was exclusively detected in Numb1:GFP IPs by MS analysis (Figure 18A).

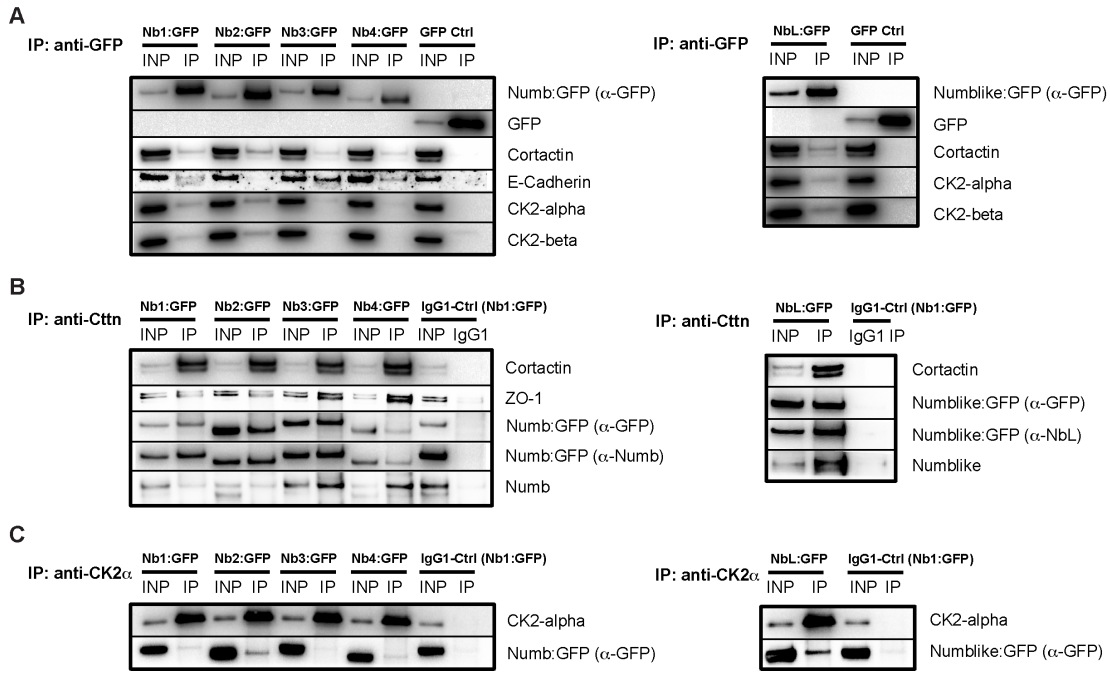

Figure 18: Cortactin and CK2 verified as novel interaction partners of Numb and Numblike.
A-C: Western blot analysis of Co-IP with anti-GFP (A) and vice versa with anti-Cortactin (anti-Cttn; B) as well as anti-CK2-alpha (anti-CK2α; C) for Numb1-4:GFP (Nb1-4:GFP), Numblike:GFP (NbL:GFP) and GFP control (GFP Ctrl) overexpression in MLE12 cells. **A:** Detection of immunoprecipitated GFP-fusion proteins with anti-GFP and co-precipitated proteins E-Cadherin, Cortactin, CK2-alpha and CK2-beta subunits with the corresponding endogenous antibodies. **B**: Detection of immunoprecipitated endogenous Cortactin and co-precipitated endogenous ZO-1, overexpressed Numb1-4:GFP and Numblike:GFP (by anti-GFP and anti-Numb or anti-Numblike) as well as endogenous Numb and Numblike. **C:** Detection of immunoprecipitated endogenous CK2-alpha and co-precipitated overexpressed Numb1-4:GFP and Numblike:GFP (by anti-GFP). Numb1:GFP cell lysates were used for control IPs with IgG1 mouse isotype antibody (IgG1-Ctrl; B and C).

Co-immunoprecipitation of the CK2-alpha and CK2-beta subunits was specifically detected for Numb1:GFP, Numb2:GFP as well as for Numblike:GFP but not for Numb3:GFP and Numb4:GFP, correlating with the MS results. Expectedly, GFP-control (GFP-Ctrl) IPs did not display any Cortactin or CK2 subunit co-enrichment. The GFP-IPs were efficient for all GFP-fusion proteins as well as for the GFP-Ctrl, indicated by GFP antibody detection. Additionally, detection of endogenous E-Cadherin was confirmed in IPs of Numb:GFP and Numblike:GFP expressing cells as a positive control for Co-IP conditions, since E-Cadherin-Numb interaction has been previously shown [10]. Reciprocally, IPs for Cortactin were performed from lysates of Numb1-4:GFP and Numblike:GFP overexpressing MLE12 cells, which clearly indicated an Co-IP of all the different overexpressed GFP-fusion proteins in the corresponding Cortactin-IP fractions as well as a co-enrichment of endogenous Numb and Numblike (Figure 18B). Moreover, the tight junction protein ZO-1, a known interaction partner of Cortactin, was detected in all Cortactin-IPs, serving as a positive control for the Co-IP efficiency. IP of endogenous CK2-alpha from Numb1-4:GFP and Numblike:GFP overexpressing MLE12 cells confirmed CK2-alpha interaction with Numb1:GFP, Numb2:GFP and Numblike:GFP reciprocally to the corresponding GFP-IPs (Figure 18C). Taken together, these results strongly suggest an interaction of both Numb and Numblike with Cortactin as well as the holoenzyme of CK2. Numb interactions with CK2 occur in this context specifically for Numb isoform 1 and isoform 2. In order to further strengthen the findings of Cortactin-Numb/Numblike interactions, subcellular co-localization of Cortactin, Numb and Numblike was investigated by co-immunofluorescence analysis. To approach this, immuno-fluorescence staining for Cortactin was performed on fixed MLE12 cells overexpressing GFP tagged Numb and Numblike versions. The z-stack projections acquired by confocal microscopy (Figure 19) clearly indicated overlapping areas of Cortactin with GFP signal for all different Numb isoforms and Numblike. Numb1:GFP and Numb2:GFP displayed clear membrane localization, whereas GFP positive signal derived from Numb3:GFP and Numb4:GFP revealed predominant cytosolic distribution in vesicle-like speckles, but also partial membrane localization. In contrast, Numblike displayed a clear homogenous cytoplasmatic GFP signal of the overexpressed GFP-fusion protein as expected from the endogenous Numblike localization.

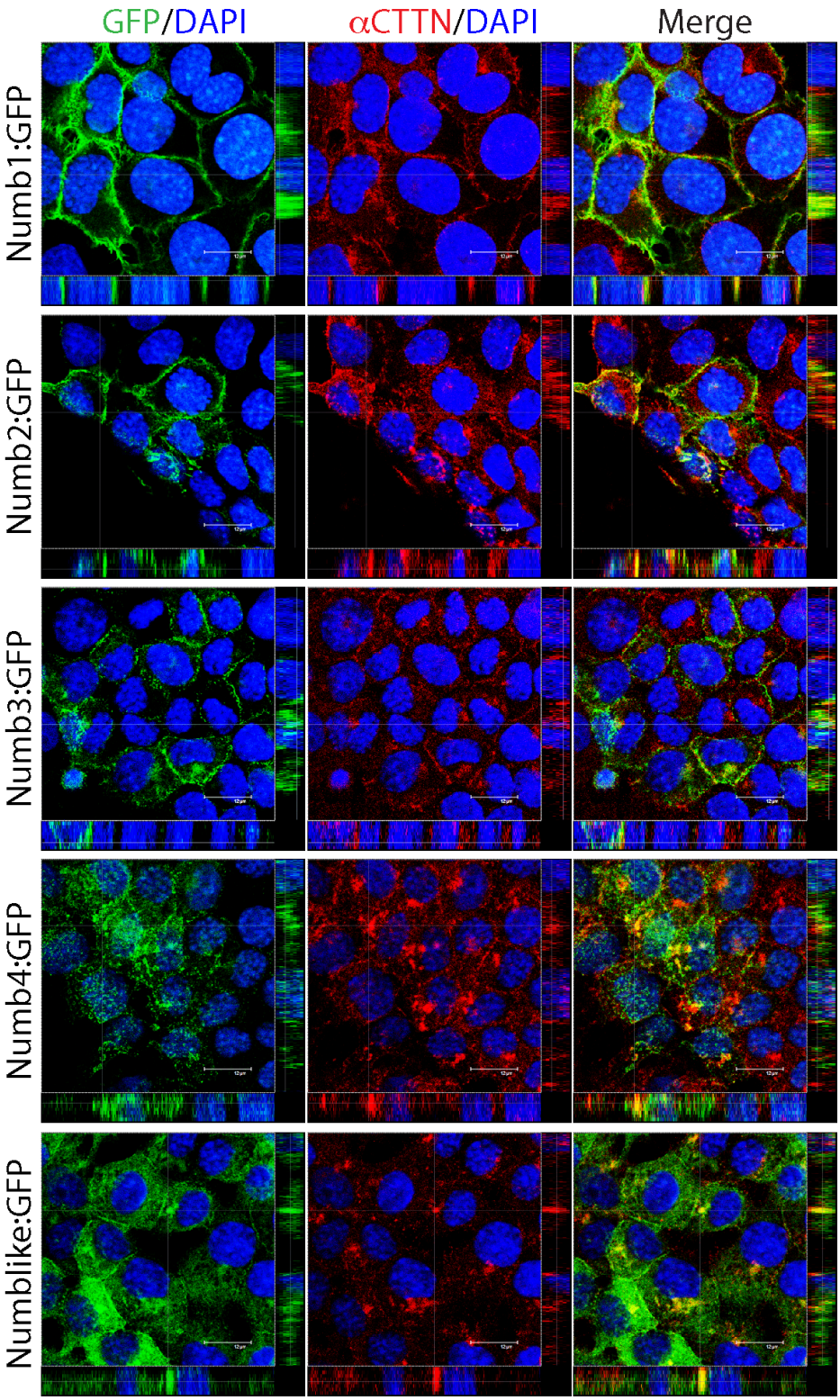

Figure 19: Subcellular localization studies for Cortactin in Numb:GFP and Numblike:GFP overexpressing MLE12 cells.
Randomly chosen representative pictures of fixed immunofluorescece stained Numb1-4:GFP and Numblike:GFP (green) overexpressing MLE12 cells with anti-Cortactin (red) to study subcellular co-localization of the proteins. Cells were seeded on glass cover slips in a 48-well plate for 24 h, fixed and stained indirectly with anti-Cortactin. Nuclei were visualized using DAPI. Pictures were acquired randomly by confocal microscopy as z-stacks at a magnification of 63x and digital zoom. Pictures are presented as cross sections concomitantly with x/z-view and y/z-view. Scale bars at 12 µm.

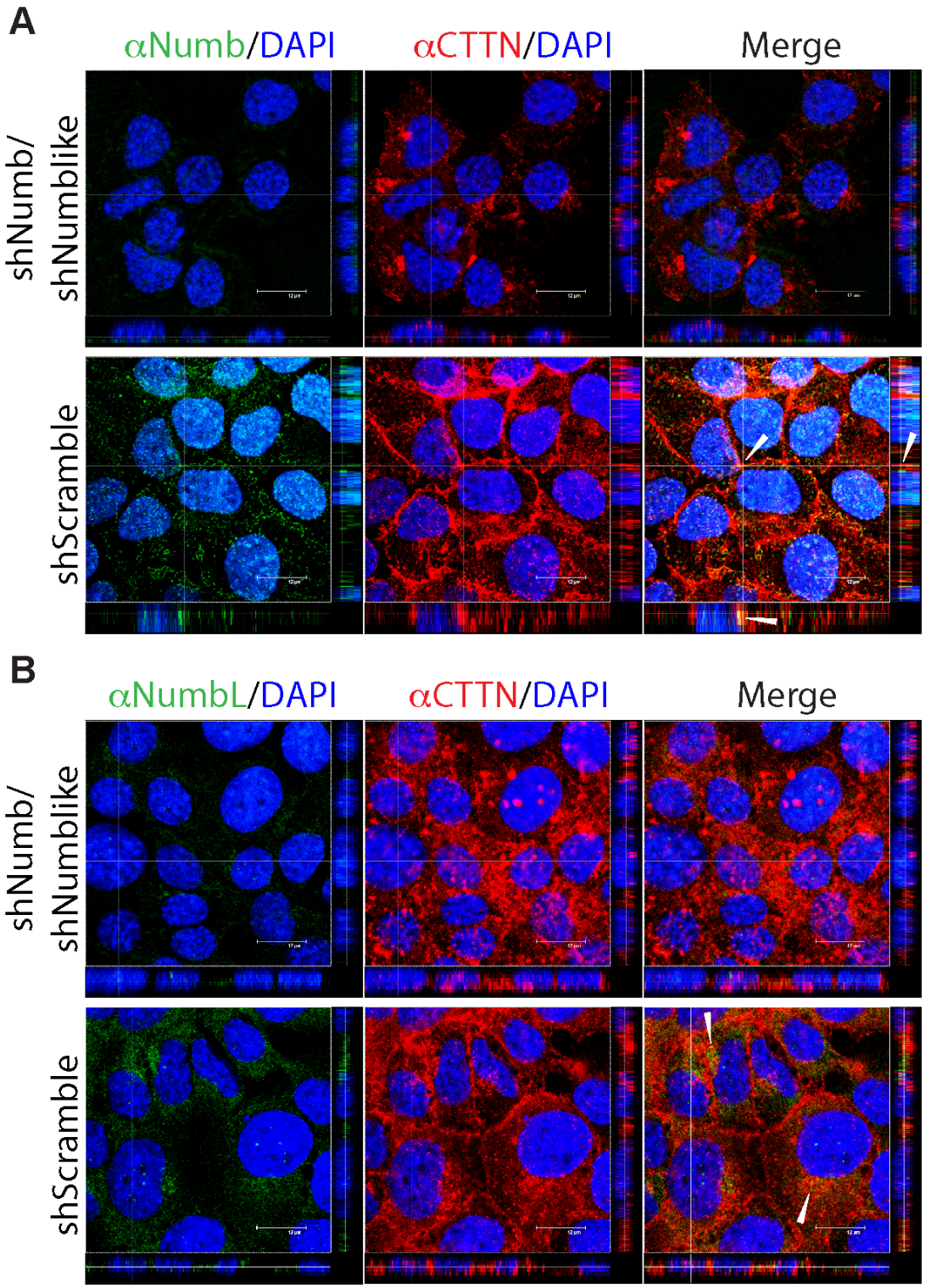

Figure 20: Subcellular localization of Cortactin in shNumb/shNumblike MLE12 cells.
A+B: Randomly chosen representative pictures of fixed immunofluorescece stained shNb/shNbL vs. shScr MLE12 cells with Cortactin (red) to study subcellular co-localization after Numb/Numblike knockdown. Cells were seeded on glass cover slips in a 48-well plate for 24 h, fixed and indirectly stained with anti-Cortactin together with anti-Numb (green, A) or anti-Numblike (NumbL; green, B). Nuclei were visualized using DAPI. Pictures were acquired randomly by confocal microscopy as z-stacks at a magnification of 63x and digital zoom. Pictures are presented as cross sections concomitantly with x/z-view and y/z-view. Scale bars at 12 µm.

Furthermore, all MLE12 overexpression conditions displayed partial and dot-like co-localization of Cortactin with the GFP-tagged Numb and Numblike underlining the Co-IP results. For Numb1:GFP and Numb2:GFP these Cortactin co-localization spots were predominantly detected in membrane regions of contacting neighboring cells. In contrast, Cortactin co-localized with Numb3:GFP and Numb4:GFP in prominent cytoplasmatic speckles as well as in perinuclear compartments of the cells. Similarly, also Numblike:GFP overexpressing MLE12 cells displayed Cortactin co-localization with the GFP-fusion protein predominantly in perinuclear areas. In line with previous subcellular localization studies of this work, subcellular distribution of Cortactin was also examined in shRNA-silenced Numb and Numblike deficient MLE12 cells. Therefore, co-immunofluorescence stainings for Numb or Numblike in combination with Cortactin were performed in dKD and *Scramble* control cells. The absence of Numb and Numblike (Figure 20A+B) resulted in a shift of subcellular Cortactin localization from the cell membrane, where it was predominantly detected in shScr cells, to the cytoplasma accumulating in perinuclear speckles. In previous studies, changes in subcellular distribution of Cortactin have been correlated with altered actin polymerization and stabilization of the cytoskeleton [178-180]. Furthermore, control cells displayed areas of Numb and Cortactin co-localization at the membrane as well as co-localization of Numblike and Cortactin in the cytoplasm (Figure 20A and B, arrows). Additionally, this subcellular co-localization of Numb/Numblike and Cortactin in shScr MLE12 cells clearly reflected the co-localization previously observed in Numb:GFP and Numblike:GFP overexpressing MLE12 cells (Figure 19). Taken together, the Co-IP experiments validated Cortactin and CK2 as two novel interaction partners for Numb and Numblike. Cortactin furthermore exhibited membrane co-localization with Numb isoform 1 and isoform 2 as well as cytosolic co-localization with Numb isoform 3, isoform 4 and Numblike. The underlying mechanisms promoted by these interactions, mediating formation and stabilization of the cell junctions, which is an essential for epithelial integrity, still need to be elucidated more detailed. Interactions of Numb and Numblike with CK2 might as well play an important role in this process of junctional complex formation and stabilization potentially modulated by CK2 kinase activity at the adherens junction level.

4 DISCUSSION

The adaptor proteins *Numb* and *Numblike* are widely expressed in different mouse tissues of the ectodermal, mesodermal and endodermal lineage during development and adulthood [115, 181], for instance in brain [98, 118, 119, 182], muscle [167], heart [2, 183] or lung [121]. In the developing, differentiating as well as adult lung, *Numb* and *Numblike* expression is detected in both epithelium and mesenchyme, which has been shown by previous investigations and also in this present study [99, 121]. During morphogenic and epithelial specification process, Numb has been involved in promoting cell polarity and asymmetric cell division [122, 123]. Furthermore, altered Numb protein expression in lung epithelial cells has been linked to *Non-small*-cell *lung* carcinoma (NSCLC), which resembles a predominant lung cancer type [127]. In order to pinpoint the lung epithelial specific enrolment of Numb and Numblike during lung development and regeneration, lung epithelial specific depletion of both genes was conducted in mice at early primordial stages of lung sprouting, which surprisingly did not exhibit any severe effects on lung development and maturation as well as on the vitality. Changes were unveiled in the composition of the distal airway epithelium and a disruption in cell-cell junctions along the entire proximo-distal axis of the lung epithelium resulting in a loss of polarity and integrity. Moreover, this study provided profound data suggesting an improvement after bleomycin induced lung fibrosis due to the absence of Numb and Numblike. In this respect, we propose an impairment and inhibition of WNT/ß-Catenin signaling underlying the improved pathological phenotype. This was further supported by mechanistic *in vitro* studies using *Numb*/*Numblike* double knockdown as well as *Numb* and *Numblike* overexpressing MLE12 cells. Besides mislocalization of the adherens junctional proteins E-Cadherin and ß-Catenin, loss of Numb and Numblike resulted in reduced WNT/ß-Catenin signaling, which was reflected by low levels of active ß-Catenin accompanied by decreased expression of several WNT/ß-Catenin downstream targets. Strikingly, we identified Cortactin and CK2 as novel interaction partners of Numb and Numblike. *Numb* and *Numblike* silencing additionally displayed mislocalization of Cortactin, ß-Catenin and E-Cadherin, which is supposed to cause destabilization of the cell junction complex. Based on our findings we propose a potential mechanism for the maintenance of epithelial cell polarity and integrity, which is discussed in the third section.

4.1 Lung epithelial specific Numb/Numblike knockout mice show loss of epithelial polarity and integrity

Previous studies showed, that the evolutionary conserved membrane-associated adaptor protein Numb plays an important role in asymmetric cell division and cell fate determination of sensory neurons in Drosophila by antagonizing Notch signaling [184, 185]. Similarly, there is evidence that both Numb and its homolog Numblike in mice exhibit redundant functions in maintenance and differentiation of neural progenitor cells by eliminating Notch signaling [118, 119, 186]. As both paralogs are widely expressed in various cell types, tissue specific conditional knockout approaches were used to decipher their functions in neuronal [118, 119] and epicardial development [112]. Interestingly, epicardial specific depletion of *Numb* and *Numblike* results in disruption of adherens junctions and cell polarity [112], while concomitant inactivation of both genes in the myocardium has been related to regulation of myocardial trabeculation and compaction by repressing Notch2 and BMP10 signaling as well as ERBB2/STAT5 signaling [2, 187]. In fact, these observations provided evidence for tissue specific involvement of Numb and Numblike in controlling cell polarity and cell-cell contact. Moreover, studies in a subset of human lung cancer, so called non-small-cell lung carcinomas (NSCLCs), revealed an activation of Notch signaling accompanied by a loss of Numb abundance [127]. These findings suggested tumor suppressive functions for Numb, which has also been previously proposed in breast cancer [109, 126]. However, the role of Numb and Numblike during lung development and adult stages remained rarely investigated so far.

In this study we approach this issue by investigating a targeted deletion of $Numb^{fl/fl}$ specifically in mouse lung epithelium on a Numblike deficient background since it had been reported that a total knockout of *Numb* and *Numblike* in mice results in early embryonic lethality [118, 129]. Lung epithelial specific *Numb*/*Numblike* dKO was generated by utilizing the doxycycline inducible *SP-CrtTA*/*tetOCre* system (Figure 6A) [130]. Efficient inactivation of *Numb* expression was confirmed exclusively in lung epithelium (Figure 6B, C, D), while *Numblike* was constitutively depleted in the entire mouse. Meanwhile, *Numb* expression in non-targeted mesenchymal cells of dKO lungs remained unaffected. Specific activation of the combined *Rosa26YFP* Cre-reporter additionally revealed YFP^{+} lineage tracing of cells along the entire proximo-

distal axis of the mature respiratory epithelium, indicating an onset of Cre activity driven by *SP-CrtTA* expression at early lung developmental stages (Figure 6E) and underlining the tissue specificity of the system since we could not find YFP^+ cells in other tissues (data not shown). Surprisingly, induced dKO mice exhibit normal lifespan and indicate no severe phenotypic alterations of the mature lung. Analysis of the different cell types, residing along the entire mature lung epithelium, revealed reduced ATII cell abundance in dKO animals. Quantification of SP-C positive ATII cells compared to total DAPI positive cells of adult lung tissue sections, displayed a 30 % decrease in ATII cell numbers of dKO lungs compared to Ctrls (Figure 7B). This result was supported by decreased mRNA expression of the ATII cell marker *Sftpc* in total lung homogenates of dKOs. By which mechanism this ATII cell reduction is promoted remains still unclear and requires further investigations. There are studies correlating a targeted ablation of ATII cells with a higher susceptibility for pulmonary fibrosis and enhanced risk of respiratory failure [188, 189]. In contrast, conditional lung epithelial specific deletion of Integrin α3ß1 has been linked to increased ATII cell abundance accompanied by an ameliorated fibrotic response to bleomycin treatment. In this particular case, reduced fibrosis was closely correlated with impaired ß-Catenin/Smad2 signaling rather than the higher ATII cell abundance [190]. Together, these observations argue for altered ATII cell self-renewal and differentiation to ATI cells [191] in our lung epithelial depleted *Numb*/*Numblike* animals, since dKOs neither display lethality by respiratory failure nor exhibit an enhanced susceptibility for pulmonary fibrosis under non-injured conditions despite the decreased ATII cell numbers. Indeed, Numb and Numblike have been implicated in regulating maintenance and differentiation of progenitor cells during neurogenesis [118, 119]. Hence, a loss of Numb and Numblike might impair the maintenance of ATII cells or even proliferation and differentiation of lung epithelial progenitor cells at earlier developmental stages. The latter may lead to an imbalance in the epithelial progenitor determination towards distinct epithelial cell fates. In order to clarify this hypothesis, differential expression analysis of different lung epithelial markers was performed to identify potential alterations in epithelial cell abundance. However, analysis of ATI cell (*Pdpn*), Clara cell (*Scgb1a1*), Ciliated cell (*Foxj1*) or Neuroendocrinal cell (*Ascl2*) marker expression did not reveal any changes indicating altered numbers of the corresponding epithelial cell types. Furthermore, there is

evidence that Numb exerts its function as a key determinant of asymmetric *versus* symmetric cell division [192, 193]. Importantly, proper balance between self-renewal and differentiation of lung specific stem or progenitor cells is indispensable and critical for normal lung morphogenesis [194-196]. In particular, Numb has been involved in asymmetric cell division of distal embryonic lung epithelial progenitor cells [121], which supports the idea of an imbalanced early epithelial progenitor or ATII cell proliferation and differentiation. Hence, profound proliferation analysis at different developmental stages might clarify this issue; however the cause of ATII cell reduction, which surprisingly has no severe effects on viability of the dKO animals, still remains unclear.

On the subcellular level, lung epithelial specific *Numb*/*Numblike* double knockout animals displayed mislocalization of the adherens junction proteins E-Cadherin and ß-Catenin in primordial epithelium of E16.5 lungs as well as in the mature lung epithelium (Figure 8, Figure 9, Figure 10). This observation perfectly correlated with the results of previous studies revealing that Numb regulates cell-cell adhesion and epithelial polarity in polarized cells [10, 197]. *Numb* depleted MDCKII epithelial kidney cells display a mislocalization of E-Cadherin and ß-Catenin from basolateral to apicolateral. In addition, the authors demonstrate a direct interaction between the PTB domain of Numb with the conserved DNYYY motif of E-Cadherin. This interaction can be suppressed by Src kinase mediated tyrosine phosphorylation of the DNYYY motif, which is promoting the internalization of E-Cadherin [10, 198, 199]. E-Cadherin is known to associate directly with ß-Catenin [200, 201] as well as other adherens junction proteins like p120-Catenin, α-Catenin or the Src substrate Cortactin, which links the adherens junction complex to F-Actin [172, 202]. In this respect, we conclude that a loss of the physical interaction between Numb and E-Cadherin, due to the absence of Numb, might result in a destabilization of the adherens junction complex in the respiratory epithelium of dKO animals. In addition, Numb has also been identified as a mediator of endocytosis [102], for example controlling internalization of E-Cadherin [203]. In this respect, studies revealed that the endocytosis of E-Cadherin, and thereby its trafficking to the lateral membrane of epithelial cells, can be negatively regulated by aPKC mediated phosphorylation of Numb. Consequently, Numb depletion has been shown to result in marked defects in E-Cadherin redistribution and trafficking to the plasma membrane by affecting

endocytosis [197, 203]. In the present study, we observed similar membrane mislocalization of E-Cadherin and ß-Catenin upon loss of Numb and Numblike. According to our findings in lung epithelium of dKO mice and previously in MDCKII cells, we here provided additional evidence for *Numb*/*Numblike* double knockdown mediated mislocalization of E-Cadherin and ß-Catenin in MLE12 cells. Alteration of E-Cadherin localization in E16.5 dKOs is accompanied by a significant increase in its protein level, whereas E-Cadherin protein level was unaffected in adult lungs though subcellular E-Cadherin localization remained perturbed. In contrast, the epithelium of adult dKOs revealed a ß-Catenin mislocalization concomitant with downregulated ß-Catenin protein level in distal airway cells (Figure 10A). Interestingly, no significant alteration of ß-Catenin protein level was detected in E16.5 dKOs, whereas reduced Serin 33/37 - Threonin 41 phosphorylation of ß-Catenin in total adult dKO lung homogenates provided evidence for an altered GSK-3ß regulated ß-Catenin stability [204], which was underlined by decreased active non-phosphorylated ß-Catenin level. Activated Wnt/ß-Catenin signaling is marked by nuclear accumulation of active ß-Catenin, which transactivates expression of WNT/ß-Catenin downstream targets in the nucleus [205]. However, total ß-Catenin level in whole dKO lung remained unchanged although distal airway cells in our animal model displayed decreased or complete lack of ß-Catenin. Since ß-Catenin is also expressed in lung mesenchyme [44, 155, 206], slight changes in lung epithelial ß-Catenin protein level are probably undetectable in total lung homogenates. In conclusion, lung epithelial loss of Numb and Numblike mediates mislocalization and an altered phosphorylation state of ß-Catenin. Numerous studies provide evidence that WNT/ß-Catenin signaling promotes cell proliferation and differentiation in different cell types [207-209]. Investigations of canonical WNT/ß-Catenin signaling in lung revealed that an activation of this pathway mediates enhanced epithelial cell proliferation, especially of distal ATII cells under disease conditions like pulmonary fibrosis or lung cancer [62, 72, 210, 211]. Based on these findings, decreased epithelial ß-Catenin protein level, in particular that of active ß-Catenin, in *Numb*/*Numblike* mutants might provide an additional explanation for the observed ATII cell reduction in adult dKO lungs. This further supports the hypothesized imbalance in lung epithelial progenitor proliferation and differentiation during development of our *Numb*/*Numblike* mutants.

The observation of reduced tight junctional protein ZO-1 in distal airway cells of adult dKO lungs (Figure 10B, C) suggests further consequence of the perturbed

adherens junctions, which are linked to tight junction proteins via the F-actin cytoskeleton [212]. Besides the fact that the adhesive force of adherens junctions is necessary to maintain the structural integrity of tight junctions [213-216], studies also suggest Numb as an important factor dynamically linking adherens and tight junctions by associating with the Par3-aPKC-Par6 polarity complex [10]. However, despite the epithelial mislocalization of E-Cadherin and ß-Catenin from basolateral to apicolateral ultrastructural analysis of adult proximal and distal epithelium did not reveal any abnormalities in dKOs correlating with the weak phenotype in our *Numb*/*Numblike* mutants. Overall, the adherence and tight junction structures in proximal and distal epithelial cells of dKO lungs were detectable and unaffected at the membrane of neighboring cells. Nevertheless, subtle changes in the quality and establishment of cell-cell contacts could not be ruled out yet, since we found no adequate method for a robust quantification of parameters, like length or opening of the cell junctional zones formed by tight and adherens junctions, at the ultrastructural level. The quantification of a potential phenotype proved to be difficult due to the fact that the planes and angles of cell junction cross sections are not consistent. Concomitant with the disruption of adherens junctions, loss of tight junction contacts, induced by the ablation of *Numb* and *Numblike* in the lung epithelium of dKO mice, was underlined by an increased epithelial barrier leakage observed in dKO mutants (Figure 10D). To further validate this physiological phenotype of a disrupted epithelial barrier, lung injury experiments utilizing influenza virus infection, representing a commonly used model to investigate epithelial barrier function, are planned for the future [217-219]. With this injury model, we attempt to prove an increased susceptibility of our dKO mutants to the influenza injury due to their loss of epithelial integrity. Taken together, these results clearly suggest an essential role for Numb and likely for Numblike in the maintenance of lung epithelial polarity as well as integrity preserving a physiological epithelial barrier.

4.2 Loss of Numb/Numblike suppresses bleomycin-induced lung fibrosis

Our results so far demonstrated moderate alterations in *Numb*/*Numblike* depleted lung epithelium under basal conditions. Moreover, we found that dKO mice exhibit a significantly increased permeability of the physiological epithelial barrier caused by

the disruption of tight and adherens junctional cell-cell contacts. Hence, we reasoned a higher susceptibility of the *Numb*/*Numblike* depleted lung epithelium to bleomycin induced lung injury, a well-characterized model to study pulmonary fibrosis [62, 143-145]. Bleomycin treatment causes alveolar cell damage and provokes a pulmonary inflammatory response accompanied by apoptotic as well as hyperplastic ATII cells [220-223]. Concomitantly, activated fibroblasts or myofibroblasts form fibrotic foci exhibiting an enhanced expression of *Acta2* and deposition of extracellular matrix proteins, like Connective tissue growth factor (*Ctgf*), Collagen I (*Col1a1*), Fibronectin (*Fn1*) and the matrix metalloproteinases *Mmp2* or *Mmp9* [62, 224-226]. The abnormal accumulation of extracellular matrix proteins within these fibrotic foci causes stiffness and damage of lung architecture resulting in respiratory failure and lethality [55, 227]. Unexpectedly, we found that bleomycin injured *Numb*/*Numblike* dKOs displayed a significantly improved survival rate compared to Ctrls, which started to die after 10 days upon injury (Figure 11B). This was surprising since we expected a dramatic effect for *Numb*/*Numblike* ablated animals given by the fact that lung epithelial integrity of mutants is disrupted in the steady state. Improved survival of *Numb*/*Numblike* dKOs was further reflected by the significantly attenuated compliance parameters, which were observed for injured mutants at both time points (14 and 21 days). The increased lung volume as well as the enhanced tissue elastance of NaCl treated dKOs might result from the compromised epithelial integrity (Figure 11C). Together, the improved survival and compliance of the challenged dKO animals suggest that a lack of Numb and Numblike in lung epithelium might restrict progression of fibrosis. Further histological trichrome stainings strengthened this hypothesis (Figure 12A). I could clearly confirm reduced fibrotic foci numbers in bleomycin treated dKO animals, reflected by the fibrotic score (Figure 12C). This was additionally indicated by the ultrastructural analysis of alveolar septae that revealed a smaller size of collagen fibers in bleomycin treated dKO lungs (Figure 12B). The histological evidences clearly show a milder and attenuated fibrotic phenotype in injured *Numb*/*Numblike* dKOs. Protein analysis of collagen contents as well as relative mRNA expression analysis for profibrotic markers, like *Col1a1*, *Ctgf*, *Tnf-alpha* or *Acta2*, validated reduced fibrosis at the molecular level in injured lungs (Figure 12D, E). In bleomycin-induced lung fibrosis of wild type mice, *Ctgf* level is strongly upregulated [228] promoted by enhanced TGF-ß cytokine release from damaged alveolar epithelial cells, which stimulates fibroblast to myofibroblasts

differentiation [71]. Moreover, TGF-ß signaling drives Tnf-alpha expression and secretion, which plays a crucial role in the recruitment of fibroblasts and their differentiation to pro-fibrotic, alpha-smooth muscle actin (*Acta2*) expressing myofibroblasts as well [62, 75]. Both, *Tnf-alpha* and *Acta2*, show an attenuated expression response in bleomycin treated dKO mice. In particular, *Acta2* mRNA levels remained completely unchanged suggesting a block of excessive fibroblast proliferation and their differentiation to myofibroblasts after lung injury in mutants. Therefore, disruption of profibrotic TGF-ß signaling as a consequence of lung epithelial *Numb* and *Numblike* depletion might be one explanation for reduced fibrosis in *Numb*/*Numblike* dKO mice. Additionally, substantial evidence for an impaired Wnt/ß-Catenin signaling in dKOs was provided by the observation of altered Wnt-target gene expression. Decreased ß-Catenin protein levels in dKO animals under basal conditions are most likely the cause of post-translational protein modifications, indicated by the unchanged relative *ß-Catenin* mRNA expression in mutant lungs (Figure 13B). Meanwhile, dKO lungs strikingly displayed lower Wnt-target gene expression in response to bleomycin treatment, whereas the expression of all tested targets remained unaffected under non-pathologic conditions, except the EMT markers *Snai1* and *Twist1*, which can be alternatively activated by TGF-ß signaling [77-79] (Figure 13A). Thus, the reduction of *Snai1* and *Twist1* further supports potential impairment of the TGF-ß pathway, which is a well known mediator of fibrosis [227, 229]. Moreover, studies revealed a *Dickkopf-1* (*Dkk1*) regulated crosstalk between both signaling pathways, TGF-ß and Wnt/ß-Catenin, particularly in the pathogenesis of fibrotic disease, indicating that canonical Wnt-signaling is a requirement for TGF-ß-mediated fibrosis [230]. However, it currently remains unclear, whether the loss of Numb/Numblike also directly affects TGF-ß pathway or if the observations only reflect indirect effects promoted by impaired Wnt/ß-Catenin signaling. Furthermore, *Wisp1* (*CCN4*), a well-established Wnt-signaling downstream target, displayed ameliorated expression upon bleomycin treatment in our *Numb*/*Numblike* mutants. *Wisp1* belongs to the large *Ctgf* (*CCN2*) containing CCN family of secreted matricellular proteins [231] and is strongly upregulated in bleomycin-induced pulmonary fibrosis of wild type mice as well as in IPF patients [62]. In further consequence, this is accompanied by an increased lung epithelial expression of Wnt/ß-Catenin signaling components like ß-Catenin, Gsk3-ß, Wnt molecules as well as Frizzled receptors during the early regeneration phase providing

broad evidence for activated Wnt-signaling during experimental fibrosis [62]. Under these conditions, *Wisp1* expression is exclusively elevated in ATII cells, whereas fibroblasts are not affected. Based on this, it is suggested that Wisp1 secreted by ATII cells exerts autocrine effects by inducing proliferation as well as the expression of pro-fibrotic mediators like Mmp9 [62]. In addition, secreted Wisp1 induces the expression of pro-fibrotic genes like *Col1a1*, *Fn1* in fibroblasts and enhances extracellular matrix deposition. However, neutralization of elevated Wisp1 secretion has been demonstrated to revert previously mentioned effects [62]. In conclusion, I suggest reduced fibrosis in bleomycin treated *Numb*/*Numblike* dKO animals by attenuated expression of *Wisp1*, *Fn1*, *Col1a1* and *Ctgf*, while *Mmp9* and *Acta2* expression even remain at unchanged levels.

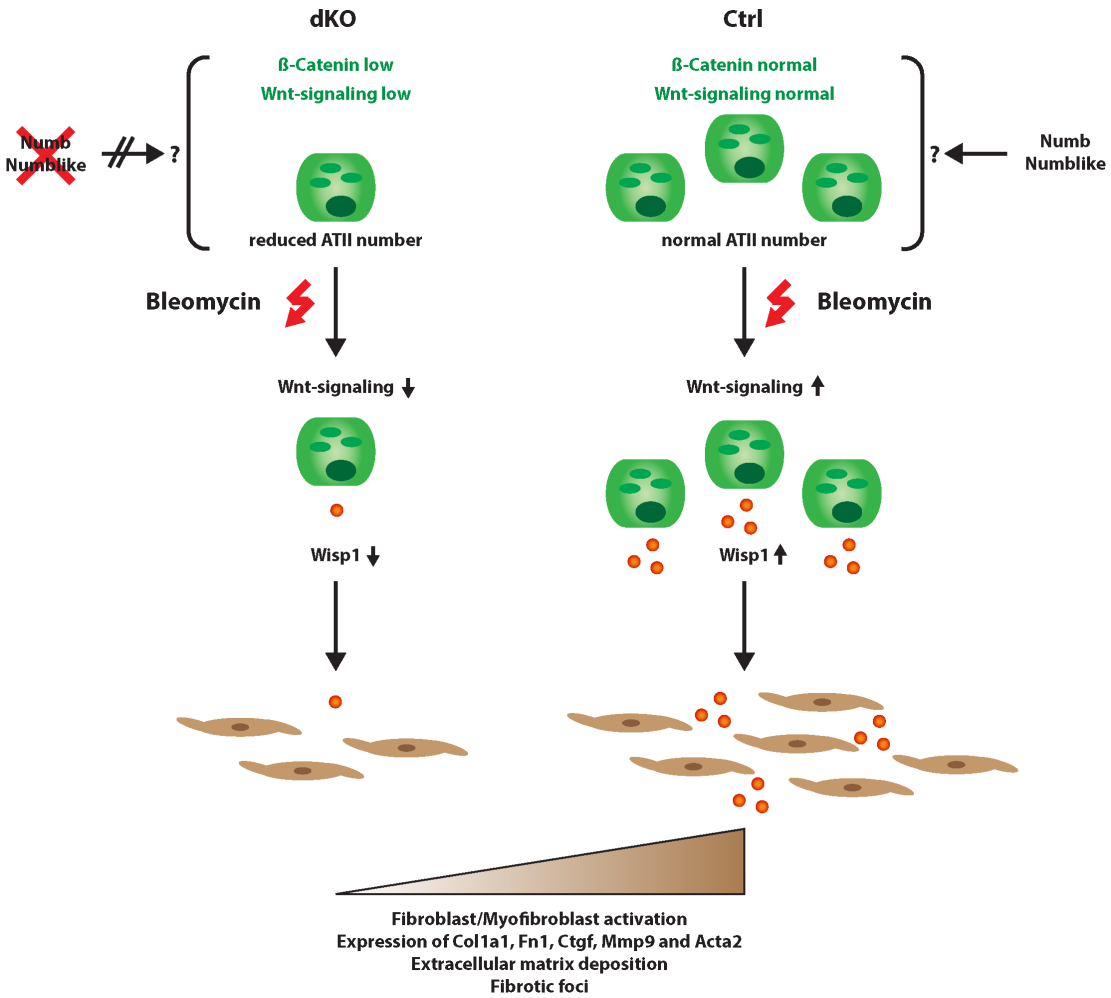

Figure 21: Decreased Wisp1 level in Numb/Numblike dKOs results in reduced lung fibrosis. Reduced numbers of ATII cells (green) as well as reduced ß-Catenin protein level in *Numb*/*Numblike* dKOs decreases Wnt-signaling activated Wisp1 secretion (red) upon bleomycin induced lung fibrosis. This results in reduction of fibroblast/myofibroblast (brown) activation, profibrotic marker expression, extracellular matrix deposition and fibrotic foci.

Considering elevated *Wisp1* expression in ATII cells as a major trigger of fibrosis progression, I conclude that the reduction of ATII cells observed in *Numb*/*Numblike* dKOs accompanied by reduced *Wisp1* expression in the remaining ATII cells upon bleomycin injury results in reduced global Wisp1 secretion, which correlates with decreased activation of profibrotic markers and hence less pronounced fibrosis (Figure 21). Even though this ameliorated phenotype we observe after respiratory injury seems to reflect secondary effects mediated by lung epithelial specific *Numb* and *Numblike* depletion, we propose that the epithelial loss of Numb and Numblike initiates these advantageous changes by impairment of canonical Wnt-signaling.

4.3 Numb/Numblike interaction with Cortactin and CK2 regulates cell junction complex stability in lung epithelial cells

In order to investigate the impact of Numb and Numblike on cell junction components, double knockdown (dKD) experiments were performed in mouse lung epithelial MLE12 cells. Concomitant loss of Numb and Numblike protein revealed altered subcellular membrane distribution of E-Cadherin from predominantly basolateral to apicolateral. This observation reflects previous studies in polarized MDCKII cells showing that E-Cadherin and Numb physically interact, as previously mentioned, and that a loss of Numb results in an equivalent E-Cadherin mislocalization [10]. Besides that, altered E-Cadherin localization in *Numb/Numblike* dKD MLE12 cells matched perfectly with the *in vivo* findings revealing apicolateral shift of E-Cadherin in *Numb/Numblike* dKO lung epithelium. Since E-Cadherin is known to directly interact with ß-Catenin within an adherens junction protein complex during maintenance of cell-cell contacts, we addressed the question if E-Cadherin mislocalization simultaneously affects subcellular localization of ß-Catenin as previously shown in MDCKII cells [10]. Furthermore, translocation of ß-Catenin in *Numb*/*Numblike* dKD MLE12 cells from basolateral to apicolateral (Figure 14E) additionally confirmed our *in vivo* observations displaying apicolateral accumulation of ß-Catenin in dKO lung epithelium. Moreover, *Numb/Numblike* dKD MLE12 cells displayed profound reduction of both total (pan) and “activated”, non-phosphorylated ß-Catenin suggesting a disruption of ß-Catenin transactivation potential in the nucleus and thereby an inhibition of Wnt-signaling (Figure 15A, B) [232]. Unaltered relative

mRNA expression of *ß-Catenin* in both double knockdown MLE12 cells as well as dKO lungs strongly argued for a reduction of ß-Catenin protein levels by post-translational regulation. This hypothesis was corroborated by GSK3-ß inhibitors (SB-216763 [160] and lithium chloride (LiCl) [159]) treated MLE12 cells mimicking Wnt-signaling activation. GSK3-ß inhibition restored the reduced active and pan-ß-Catenin protein levels in *Numb/Numblike* dKD cells to the level of untreated controls (Figure 15B). However, decreased ß-Catenin levels in untreated dKD cells affected only a subset of Wnt-downstream target genes on the transcriptional level. Well-established targets like *Wisp1*, *CyclinD1* and *Mmp2* revealed significantly reduced levels in untreated *Numb/Numblike* dKD cells, whereas *Axin1/2*, *Snai1*, *cMyc*, *Brachyury2* and *Mmp9* expression remained unexpectedly unchanged (Figure 15C). Hence, these divergent alterations argued either for compensational crosstalk with other signaling pathways or for residual ß-Catenin activity in dKD cells, which might be sufficient to promote efficient target gene expression. Taken together, I conclude that ß-Catenin mediated transcriptional activation is partially disrupted upon concomitant loss of *Numb* and *Numblike*. LiCl as well as SB-216763 treatment demonstrated reactivation of *Wisp1* and *CyclinD1* expression in double knockdown cells, whereas *Mmp2* expression remained unaffected indicating that additional signaling pathways might compensate for altered Wnt-signaling. Unaltered *Snai1* and *Mmp9* expression in dKD cells might be explained by compensatory activation of TGF-ß-signaling restoring the expression of these genes. Further evidence supporting the hypothesis of impaired Wnt/ß-Catenin signaling was provided by reduced *Wisp1* expression levels in both the dKD and dKO system. As previously mentioned, secreted Wisp1 stimulates enhanced EMT-marker expression in ATII cells promoting transition to (myo-) fibroblasts, a crucial step during pulmonary fibrosis onset [62]. The decreased EMT marker expression in *Numb/Numblike* deficient cells suggests reduced susceptibility for EMT supporting ameliorated pulmonary fibrosis in bleomycin treated dKO animals.

In order to gain deeper insights into functional mechanisms mediated by Numb and Numblike, a quantitative MS based interactome screen was performed to identify novel isoform-specific Numb as well as Numblike interaction partners in lung epithelial cells. A substantial number of enriched proteins for Numb1-4:GFP co-immunoprecipitation included several previously reported Numb interaction partners, e.g. Clathrin, AP-1 complex subunits or alpha-adaptin, which are members of the endosomal trafficking machinery [102]. Remarkably, a small subset of these proteins,

e.g. AP-1 or AP-2 subunits, were additionally identified in Numblike:GFP Co-IPs as well.

GO-term analysis of enriched Numb/Numblike interactors revealed a large subset of proteins involved in cell junction and cortical cytoskeleton maintenance, e.g. Vinculin, Arp2/3 as well as additional Actin-related proteins like Cortactin. The majority of cortical and junctional proteins, including Cortactin, Vinculin and Arp2/3 complex units, was exclusively co-immunoprecipitated with the membrane associated isoforms (Numb1 or 2), whereas a small subset of Actin-related proteins was identified for both cytoplasmic Numb isoforms (Numb3, 4) and for Numblike as well. Besides the previously described Numb interaction partner E-Cadherin [10], we could validate Cortactin as a novel interaction partner of Numb and also Numblike by reciprocal co-immunoprecipitation analysis. Cortactin serves as scaffold protein in actin cytoskeleton organization by binding to F-actin and Arp2/3 [179]. In epithelial cells, Cortactin provides a platform for ß-Catenin, E-Cadherin and Vinculin interactions linking F-actin to the adherens junction complex [172, 178]. Based on these findings, we imply a potential involvement of Cortactin in Numb/Numblike mediated cell-cell contact organization.

It's well established that the SH3-domain of *Drosophila* and mouse Cortactin facilitates a direct interaction with the tight junction protein ZO-1 [233]. Based on our previously reported ZO-1 mislocalization and protein reduction in *Numb*/*Numblike* dKO lung epithelium as well as Cortactin/ZO-1 interaction in MLE12 cells, we assign Numb/Numblike as mediators of adherens and tight junctional cell-cell contacts. This hypothesis is further supported by subcellular co-localization of Numb/Numblike and Cortactin in MLE12 cells (Figure 19). Thereby, we demonstrated that overexpressed Numb1:GFP and Numb2:GFP exclusively co-localized with Cortactin in membrane-associated speckles, whereas overexpressed Numb3:GFP, Numb4:GFP and Numblike:GFP overlapped with Cortactin predominantly in perinuclear speckles. Expectedly, shRNA mediated loss of *Numb* and *Numblike* in MLE12 cells displayed disruption of subcellular Cortactin localization, further suggesting Numb/Numblike function as adaptor proteins of Cortactin (Figure 20), which might regulate the stabilization of the membrane-tethered cell junction complexes. Post-translational modifications of Cortactin have been linked to regulate adherens junctional anchoring to the cytoskeleton and therefore facilitate the formation of a stable E-Cadherin-ß-Catenin-Cortactin-Vinculin complex, which in turn is essential to link this complex to

the actin cytoskeleton [172]. In general, post-translational modifications of Cortactin play important roles in multiple actin dependent cellular processes, like the formation of podosomes in fibroblasts [234], of invadopodia in breast cancer cells [235], of Clathrin-coated pits during endosomal trafficking [236, 237] or, as previously mentioned, the establishment and stabilization of adhesive contact zones in epithelial cells [178]. Additional indication for the involvement of Numb and Numblike as adaptor proteins in actin mediated stabilization of epithelial cell-cell contacts was provided by the identification of multiple actin related proteins for all Numb isoforms as well as Numblike in our MS based interaction screen (Table 40). The modulation of Cortactin activity is mainly regulated by serine-threonine/tyrosine phosphorylation [172, 238] and deacetylation through Histone-deacetylase HDAC6 [175], in the latter case promoting Cortactin/F-actin interaction. Therefore, I suggest an enrolment of Numb/Numblike in orchestrating post-translational modifications of Cortactin as well as an indirect impact in cell-cell contact stabilization. Intriguingly, Casein-kinase II (CK2), a serine/threonine-kinase, which has been shown to increase HDAC6 deacetylase activity [176], is highly enriched in the Numb/Numblike MS based screen. Additional validation of CK2 alpha and beta subunits by reciprocal Co-IP revealed physical interaction with Numb isoform 1 and 2 as well as Numblike (Figure 18A). In conclusion, I propose here a potential mechanism for Numb and Numblike in the regulation of tight and adherens junction stability in lung epithelium involving Cortactin and CK2 (Figure 22).

In our model we assign adaptor function to Numb isoforms 1 and 2 linking CK2 to the adherens junction complex (Figure 22). CK2 has been shown to phosphorylate E-Cadherin and E-Cadherin-tethered ß-Catenin at adherens junctions facilitating a strong interaction of both adherens junction proteins in the complex [173, 174]. In particular, CK2 phosphorylation of ß-Catenin additionally supports stable interaction of ß-Catenin and α-Catenin, a further F-Actin linking protein in the adhesion complex [174]. Moreover, Numb-Cortactin interaction might substantially contribute to the stabilization of the actin cytoskeleton linked complex, which includes E-Cadherin, ß-Catenin, Vinculin and α-Catenin. In such a scenario, Numb associated CK2 may facilitate HDAC6 mediated deacetylation of Cortactin [175], which in turn becomes more susceptible to associate with F-actin filaments [176]. Direct Cortactin/ZO-1 binding may in part contribute to the organization and assembly of membrane

networks within tight junctions [179, 233]. Hence, due to Numb/Cortactin interaction I suggest that Numb might additionally facilitate ZO-1/Cortactin mediated organization and stabilization of tight junctions involving Cortactin deacetylation by HDAC6 and F-actin coupling.

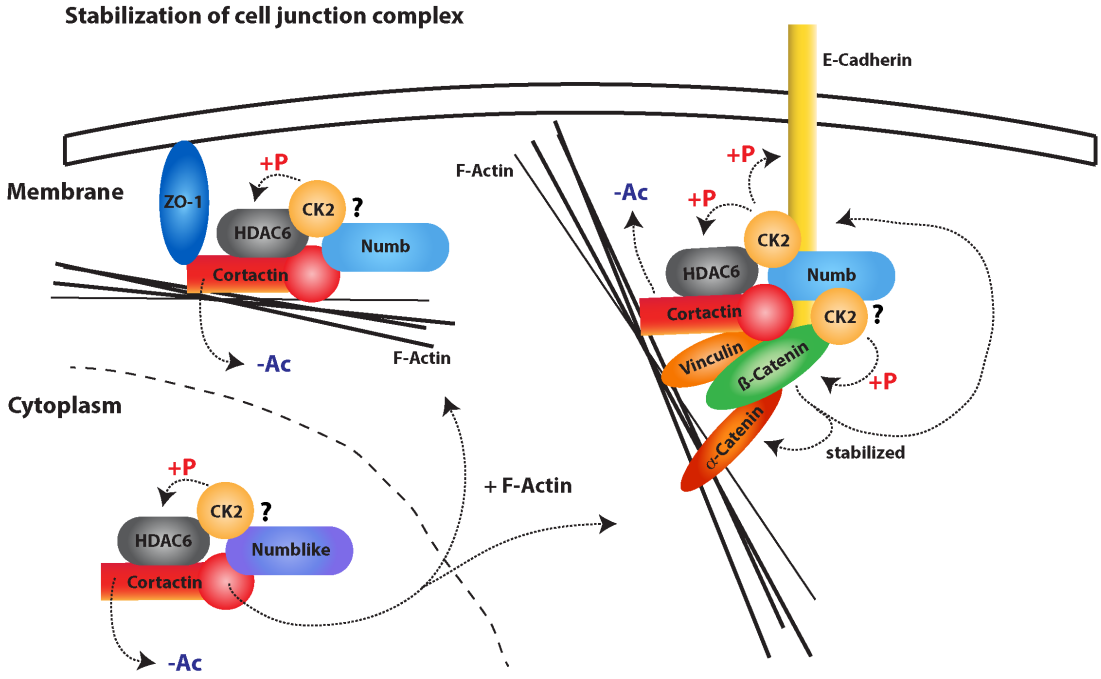

Figure 22: Potential mechanism for Numb and Numblike in regulation of cell-contact zones.
A: In the presence of Numb and Numblike adaptor proteins, Numb interacts with E-Cadherin and Cortactin at adherens junctions potentially involving complexation with CK2, which promotes HDAC6 activation and thus deacetylation of Cortactin. Consequently, F-actin binding activity of Cortactin increases. CK2 phosphorylation additionally strengthens interactions of E-Cadherin, ß-Catenin and α-Catenin in the junction complex including Vinculin representing a further crucial F-actin linking component. Cortactin/ZO-1 association mediated by Numb and Numblike as well links tight junctions to the cytoskeleton supporting cell-cell contact stability. Numblike/CK2 interaction in the cytoplasm may as well contribute to increased Cortactin affinity for F-actin.

However, Cortactin has also been identified as a component of Clathrin-coated pits in the process of endosomal trafficking [236, 237]. Although the involvement of Numb in Clathrin-mediated endosomal trafficking has been well characterized so far [164, 165, 239], to my knowledge there has been no clear evidence directly linking Numblike to endocytosis. Thus, the observed Numblike/Cortactin interaction proposes novel regulatory functions of Numblike as a cytoplasmic adaptor protein for Cortactin endorsing protein shuttling to tight and adherens junctions. This hypothesized cytoplasmic adaptor function is further supported by multiple indications, like cytosolic co-localization of Numblike/Cortactin, high structural similarity of Numblike/Numb isoform 1 [98] and the substantial enrichment of AP-1

and AP-2 complex subunits in both of the MS based screens for Numb and Numblike. In line with suggested Numb1/2 adaptor functions of CK2 binding, we propose similar functions for Numblike. Numblike associated CK2 may recruit Cortactin for subsequent CK2 activated HDAC6 deacetylation, which consequently enhances the F-actin binding affinity of Cortactin [175, 176], a requirement for stabilized tight and adherens junctions [172, 178].

Based on this model, I conclude that the concomitant loss of both adaptor proteins Numb and Numblike in lung epithelial cells primarily compromises the establishment of proper cell-cell contacts by perturbing tight and adherens junctional protein complexes. In consequence, the disruption of these protein complexes exhibited by mislocalization of E-Cadherin, ß-Catenin and Cortactin, affects the maintenance of epithelial cell polarity and barrier function [10, 111, 240]. To date we have no explanation for the decline of total and active ß-Catenin protein *in vivo* and *in vitro*, which was accompanied by reduced Wnt/ß-Catenin target gene expression including *Wisp1*, *CyclinD1*, *Snai1* and *Twist1*. Intriguingly, CK2 and GSK-3ß synergistically diminish the cytoplasmic ß-Catenin level in a multi-protein complex that controls ß-Catenin degradation [174]. CK2 thereby mediates initial ß-Catenin phosphorylation, which subsequently facilitates ß-Catenin/GSK-3ß binding. In consequence, GSK-3ß phosphorylated ß-Catenin is subjected to proteasomal degradation [174]. Chemical GSK-3ß inhibition clearly demonstrated a restoration of the reduced total and active ß-Catenin protein as well as *Wisp1* and *CyclinD1* expression levels indicating enhanced GSK-3ß dependent degradation of ß-Catenin in *Numb*/*Numblike* deficient epithelial cells.

Therefore, we hypothesize that Numb/Numblike interaction with CK2 might either influence CK2 substrate specificity or general CK2 kinase activity consequently regulating cytosolic ß-Catenin stability. This hypothesis is further supported by studies, which revealed that a down regulation of CK2-subunits (i.e. CK2-ß) in tumor cells correlates with an induced expression of EMT marker genes like *Snai1* [177]. CK2-ß inactivated epithelial cells display EMT-like changes in morphology, increased migration, as well as anchorage-independent growth, alterations that depend on *Snai1* induction [177]. *Snai1* expression in epithelial cells is negatively regulated concomitantly by CK2 and GSK-3ß, which suppresses EMT and thereby maintains epithelial integrity [177].

In order to investigate potential activity changes of CK2 in *Numb*/*Numblike* deficient cells, I will apply a CK2 specific kinase assay in the future, which might pinpoint potential impairment of CK2 substrate specificity. Phospho-proteome analysis of *Numb*/*Numblike* dKD MLE12 cells will be utilized to elucidate alterations in the phosphorylation state of adherens junctional proteins. Moreover, for better characterization of Numb/Numblike dependent tight and adherens junction complex stabilization, I plan to decipher interactions between different complex components in more detail using quantitative Co-IP approaches in dKD MLE12 cells.

In summary, our results demonstrated decreased epithelial integrity combined with altered cell polarity in *Numb*/*Numblike* deficient lung epithelium. Moreover, I corroborated these findings in a polarized *Numb* and *Numblike* silenced lung epithelial cell line and in addition to this revealed novel interaction partners of both Numb and Numblike, which unveiled a new potential regulatory mechanism of intracellular ß-Catenin stability. Tight and adherens junctional organization and stabilization mediated by Numb, Numblike, Cortactin and CK2 interactions might involve control of ß-Catenin promoted signal transduction proposing a novel mechanism in cell junction dependent regulation of Wnt/ß-Catenin signaling. I further demonstrated reduced bleomycin induced fibrosis in *Numb*/*Numblike* depleted lung epithelium as a result of the perturbed ß-Catenin transactivation assuming canonical Wnt/ß-Catenin signaling as crucial trigger of pulmonary fibrosis [62, 72, 241]. Thus, interference with Numb/Numblike mediated ß-Catenin signaling offers a way to treat IPF in humans. This conclusion is also supported by studies correlating inhibition of the ATII cell secreted Wnt target Wisp1 with reduced lung fibrosis [62, 210, 242]. In order to better understand the underlying molecular mechanisms in our model, future work will require a more detailed characterization of Numb/Numblike mediated regulation of ß-Catenin stability.

V. LIST OF FIGURES

VI. LIST OF TABLES

VII. ACKNOWLEDGEMENTS

I would like to express my sincere gratitude to a large number of people that supported me during all these years of my dissertation.

First of all, I would like to address my deep recognition to Professor Dr. Dr. Thomas Braun for offering me the great opportunity to perform my PhD thesis in his department of the Max Planck Institute for Heart and Lung Research Bad Nauheim, for the genius scientific input and the constant encouragement. Special appreciations are directed as well towards my group leader Dr. André Schneider for his thorough supervision, his beneficial ideas, critics and patience, always helping me to advance my work.

I would like to thank my committee members Professor Dr. Ralf Galuske and Professor Dr. Ralf Kaldenhoff from the University of Darmstadt for the eagerness to support my doctoral graduation.

Furthermore, I thank our collaboration partners Prof. Dr. Wolfgang Kummer and Dr. Ulrich Gärtner from the Institute for Anatomy and Cell Biology of the Justus-Liebig University Gießen for the electron microscopy analysis, Dr. Bernd Giebel and Dr. André Görgens from the University Hospital Essen for generating the Numb and Numblike overexpressing MLE12 cell line and our collaborators in Buenos Aires for the animal husbandry and help with the injury experiments.

Moreover, I appreciated the help of Dr. Sawa Kostin from the EM service group of the MPI Bad Nauheim with the EM analysis and also the group of Dr. Soni Pullamsetti, especially Hamza and Uta for helping me with some animal experiments and data analysis. I also address many thanks to all lab technicians for their unlimited and dedicated support, in particular Marion, for her competent assistance with a lot of animal experiments as well as Birgit, Marianne, Katja and Alice for the genotyping. Additionally, I would like to acknowledge the work of our animal caretakers who provided an excellent animal husbandry.

Many thanks are also dedicated to my group, especially my ‘’Dönerstag Buddy’’ Florian and Polina, as well as the other lab mates, my entertainment fellow Megan, my protein specialist Alessandro, my second group ‘’the Böttgers’’, my crazy lunch jamming group Dani, Ana and Krishna, my after work beer homes Jorge, Giovanni and Justin, my buddy Piera and of course all those I did not mention here. You always supported me and helped me to carry on in different ways.

My special appreciation is directed towards two people that ‘’prolonged’’ my PhD in a sweet way, namely Malle, who never showed up for our band rehearsals and Daniel the D, alias Sir SILAC II, who taught me to use ‘’the pick of destiny’’.

Last but not least, I would like to express my deepest gratitude to my parents, my sister and to my ‘’love bird’’ Diana. You always pushed me, supported me and gave me fresh energy during all that time of my study.

VIII. REFERENCES

1. Uemura, T., et al., *numb, a gene required in determination of cell fate during sensory organ formation in Drosophila embryos.* Cell, 1989. **58**(2): p. 349-60.
2. Yang, J., et al., *Inhibition of Notch2 by Numb/Numblike controls myocardial compaction in the heart.* Cardiovasc Res, 2012. **96**(2): p. 276-85.
3. Cayouette, M. and M. Raff, *Asymmetric segregation of Numb: a mechanism for neural specification from Drosophila to mammals.* Nat Neurosci, 2002. **5**(12): p. 1265-9.
4. Li, P.S., et al., *The clathrin adaptor Numb regulates intestinal cholesterol absorption through dynamic interaction with NPC1L1.* Nat Med, 2014. **20**(1): p. 80-6.
5. McGill, M.A., et al., *Numb regulates post-endocytic trafficking and degradation of Notch1.* J Biol Chem, 2009. **284**(39): p. 26427-38.
6. McGill, M.A. and C.J. McGlade, *Mammalian numb proteins promote Notch1 receptor ubiquitination and degradation of the Notch1 intracellular domain.* J Biol Chem, 2003. **278**(25): p. 23196-203.
7. Qiu, L., et al., *Recognition and ubiquitination of Notch by Itch, a hect-type E3 ubiquitin ligase.* J Biol Chem, 2000. **275**(46): p. 35734-7.
8. Sczaniecka, M., et al., *MDM2 protein-mediated ubiquitination of numb protein: identification of a second physiological substrate of MDM2 that employs a dual-site docking mechanism.* J Biol Chem, 2012. **287**(17): p. 14052-68.
9. Song, Y. and B. Lu, *Interaction of Notch signaling modulator Numb with alpha-Adaptin regulates endocytosis of Notch pathway components and cell fate determination of neural stem cells.* J Biol Chem, 2012. **287**(21): p. 17716-28.
10. Wang, Z., et al., *Numb regulates cell-cell adhesion and polarity in response to tyrosine kinase signalling.* EMBO J, 2009. **28**(16): p. 2360-73.
11. Treuting, P.M., et al., *Comparative anatomy and histology : a mouse and human atlas*. 1st ed. 2012, Amsterdam ; Boston: Elsevier/Academic Press. xii, 461 p.
12. Herriges, M. and E.E. Morrisey, *Lung development: orchestrating the generation and regeneration of a complex organ.* Development, 2014. **141**(3): p. 502-13.
13. Goss, A.M., et al., *Wnt2/2b and beta-catenin signaling are necessary and sufficient to specify lung progenitors in the foregut.* Dev Cell, 2009. **17**(2): p. 290-8.
14. Domyan, E.T., et al., *Signaling through BMP receptors promotes respiratory identity in the foregut via repression of Sox2.* Development, 2011. **138**(5): p. 971-81.
15. Sekine, K., et al., *Fgf10 is essential for limb and lung formation.* Nat Genet, 1999. **21**(1): p. 138-41.
16. Bellusci, S., et al., *Fibroblast growth factor 10 (FGF10) and branching morphogenesis in the embryonic mouse lung.* Development, 1997. **124**(23): p. 4867-78.
17. Bellusci, S., et al., *Involvement of Sonic hedgehog (Shh) in mouse embryonic lung growth and morphogenesis.* Development, 1997. **124**(1): p. 53-63.

18. Weaver, M., N.R. Dunn, and B.L. Hogan, *Bmp4 and Fgf10 play opposing roles during lung bud morphogenesis.* Development, 2000. **127**(12): p. 2695-704.
19. Tang, N., et al., *Control of mitotic spindle angle by the RAS-regulated ERK1/2 pathway determines lung tube shape.* Science, 2011. **333**(6040): p. 342-5.
20. Chen, J. and M.A. Krasnow, *Integrin Beta 1 suppresses multilayering of a simple epithelium.* PLoS One, 2012. **7**(12): p. e52886.
21. Warburton, D., et al., *Lung organogenesis.* Curr Top Dev Biol, 2010. **90**: p. 73-158.
22. Que, J., et al., *Multiple roles for Sox2 in the developing and adult mouse trachea.* Development, 2009. **136**(11): p. 1899-907.
23. Perl, A.K., et al., *Normal lung development and function after Sox9 inactivation in the respiratory epithelium.* Genesis, 2005. **41**(1): p. 23-32.
24. Liu, Y. and B.L. Hogan, *Differential gene expression in the distal tip endoderm of the embryonic mouse lung.* Gene Expr Patterns, 2002. **2**(3-4): p. 229-33.
25. Rawlins, E.L., et al., *The Id2+ distal tip lung epithelium contains individual multipotent embryonic progenitor cells.* Development, 2009. **136**(22): p. 3741-5.
26. Zhang, Y., et al., *A Gata6-Wnt pathway required for epithelial stem cell development and airway regeneration.* Nat Genet, 2008. **40**(7): p. 862-70.
27. Zhang, Y., et al., *GATA and Nkx factors synergistically regulate tissue-specific gene expression and development in vivo.* Development, 2007. **134**(1): p. 189-98.
28. Zhou, L., et al., *Thyroid transcription factor-1, hepatocyte nuclear factor-3beta, surfactant protein B, C, and Clara cell secretory protein in developing mouse lung.* J Histochem Cytochem, 1996. **44**(10): p. 1183-93.
29. Zhou, L., et al., *Hepatocyte nuclear factor-3beta limits cellular diversity in the developing respiratory epithelium and alters lung morphogenesis in vivo.* Dev Dyn, 1997. **210**(3): p. 305-14.
30. Bove, P.F., et al., *Human alveolar type II cells secrete and absorb liquid in response to local nucleotide signaling.* J Biol Chem, 2010. **285**(45): p. 34939-49.
31. Uhal, B.D., *Cell cycle kinetics in the alveolar epithelium.* Am J Physiol, 1997. **272**(6 Pt 1): p. L1031-45.
32. Adamson, I.Y. and D.H. Bowden, *Derivation of type 1 epithelium from type 2 cells in the developing rat lung.* Lab Invest, 1975. **32**(6): p. 736-45.
33. Evans, M.J., et al., *Renewal of alveolar epithelium in the rat following exposure to NO2.* Am J Pathol, 1973. **70**(2): p. 175-98.
34. Kim, C.F., et al., *Identification of bronchioalveolar stem cells in normal lung and lung cancer.* Cell, 2005. **121**(6): p. 823-35.
35. Rawlins, E.L., et al., *The role of Scgb1a1+ Clara cells in the long-term maintenance and repair of lung airway, but not alveolar, epithelium.* Cell Stem Cell, 2009. **4**(6): p. 525-34.
36. Rock, J.R. and B.L. Hogan, *Epithelial progenitor cells in lung development, maintenance, repair, and disease.* Annu Rev Cell Dev Biol, 2011. **27**: p. 493-512.
37. Evans, M.J., et al., *Cellular and molecular characteristics of basal cells in airway epithelium.* Exp Lung Res, 2001. **27**(5): p. 401-15.

38. Hong, K.U., et al., *In vivo differentiation potential of tracheal basal cells: evidence for multipotent and unipotent subpopulations.* Am J Physiol Lung Cell Mol Physiol, 2004. **286**(4): p. L643-9.
39. Rock, J.R., et al., *Basal cells as stem cells of the mouse trachea and human airway epithelium.* Proc Natl Acad Sci U S A, 2009. **106**(31): p. 12771-5.
40. Williams, O.W., et al., *Airway mucus: From production to secretion.* Am J Respir Cell Mol Biol, 2006. **34**(5): p. 527-36.
41. Van Lommel, A., *Pulmonary neuroendocrine cells (PNEC) and neuroepithelial bodies (NEB): chemoreceptors and regulators of lung development.* Paediatr Respir Rev, 2001. **2**(2): p. 171-6.
42. Wodarz, A. and R. Nusse, *Mechanisms of Wnt signaling in development.* Annu Rev Cell Dev Biol, 1998. **14**: p. 59-88.
43. Heuberger, J. and W. Birchmeier, *Interplay of cadherin-mediated cell adhesion and canonical Wnt signaling.* Cold Spring Harb Perspect Biol, 2010. **2**(2): p. a002915.
44. Okubo, T. and B.L. Hogan, *Hyperactive Wnt signaling changes the developmental potential of embryonic lung endoderm.* J Biol, 2004. **3**(3): p. 11.
45. Dean, C.H., et al., *Canonical Wnt signaling negatively regulates branching morphogenesis of the lung and lacrimal gland.* Dev Biol, 2005. **286**(1): p. 270-86.
46. Shu, W., et al., *Wnt/beta-catenin signaling acts upstream of N-myc, BMP4, and FGF signaling to regulate proximal-distal patterning in the lung.* Dev Biol, 2005. **283**(1): p. 226-39.
47. Mucenski, M.L., et al., *beta-Catenin is required for specification of proximal/distal cell fate during lung morphogenesis.* J Biol Chem, 2003. **278**(41): p. 40231-8.
48. Kumar, P.A., et al., *Distal airway stem cells yield alveoli in vitro and during lung regeneration following H1N1 influenza infection.* Cell, 2011. **147**(3): p. 525-38.
49. Giangreco, A., S.D. Reynolds, and B.R. Stripp, *Terminal bronchioles harbor a unique airway stem cell population that localizes to the bronchoalveolar duct junction.* Am J Pathol, 2002. **161**(1): p. 173-82.
50. Hong, K.U., et al., *Basal cells are a multipotent progenitor capable of renewing the bronchial epithelium.* Am J Pathol, 2004. **164**(2): p. 577-88.
51. Rock, J.R., S.H. Randell, and B.L. Hogan, *Airway basal stem cells: a perspective on their roles in epithelial homeostasis and remodeling.* Dis Model Mech, 2010. **3**(9-10): p. 545-56.
52. Gribbin, J., et al., *Incidence and mortality of idiopathic pulmonary fibrosis and sarcoidosis in the UK.* Thorax, 2006. **61**(11): p. 980-5.
53. Kim, D.S., H.R. Collard, and T.E. King, Jr., *Classification and natural history of the idiopathic interstitial pneumonias.* Proc Am Thorac Soc, 2006. **3**(4): p. 285-92.
54. Raghu, G., et al., *An official ATS/ERS/JRS/ALAT statement: idiopathic pulmonary fibrosis: evidence-based guidelines for diagnosis and management.* Am J Respir Crit Care Med, 2011. **183**(6): p. 788-824.
55. King, T.E., Jr., A. Pardo, and M. Selman, *Idiopathic pulmonary fibrosis.* Lancet, 2011. **378**(9807): p. 1949-61.

56. van Moorsel, C.H., et al., *Surfactant protein C mutations are the basis of a significant portion of adult familial pulmonary fibrosis in a dutch cohort.* Am J Respir Crit Care Med, 2010. **182**(11): p. 1419-25.
57. Willis, B.C., R.M. duBois, and Z. Borok, *Epithelial origin of myofibroblasts during fibrosis in the lung.* Proc Am Thorac Soc, 2006. **3**(4): p. 377-82.
58. Denburg, J.A. and S.F. van Eeden, *Bone marrow progenitors in inflammation and repair: new vistas in respiratory biology and pathophysiology.* Eur Respir J, 2006. **27**(3): p. 441-5.
59. Abe, S., et al., *Cells derived from the circulation contribute to the repair of lung injury.* Am J Respir Crit Care Med, 2004. **170**(11): p. 1158-63.
60. Willis, B.C., et al., *Induction of epithelial-mesenchymal transition in alveolar epithelial cells by transforming growth factor-beta1: potential role in idiopathic pulmonary fibrosis.* Am J Pathol, 2005. **166**(5): p. 1321-32.
61. Kim, K.K., et al., *Alveolar epithelial cell mesenchymal transition develops in vivo during pulmonary fibrosis and is regulated by the extracellular matrix.* Proc Natl Acad Sci U S A, 2006. **103**(35): p. 13180-5.
62. Konigshoff, M., et al., *WNT1-inducible signaling protein-1 mediates pulmonary fibrosis in mice and is upregulated in humans with idiopathic pulmonary fibrosis.* J Clin Invest, 2009. **119**(4): p. 772-87.
63. Davis, G.S., K.O. Leslie, and D.R. Hemenway, *Silicosis in mice: effects of dose, time, and genetic strain.* J Environ Pathol Toxicol Oncol, 1998. **17**(2): p. 81-97.
64. Roberts, S.N., et al., *A novel model for human interstitial lung disease: hapten-driven lung fibrosis in rodents.* J Pathol, 1995. **176**(3): p. 309-18.
65. Finkelstein, J.N., et al., *Early alterations in extracellular matrix and transforming growth factor beta gene expression in mouse lung indicative of late radiation fibrosis.* Int J Radiat Oncol Biol Phys, 1994. **28**(3): p. 621-31.
66. Bonniaud, P., et al., *Smad3 null mice develop airspace enlargement and are resistant to TGF-beta-mediated pulmonary fibrosis.* J Immunol, 2004. **173**(3): p. 2099-108.
67. Sime, P.J., et al., *Adenovector-mediated gene transfer of active transforming growth factor-beta1 induces prolonged severe fibrosis in rat lung.* J Clin Invest, 1997. **100**(4): p. 768-76.
68. Gharaee-Kermani, M., M. Ullenbruch, and S.H. Phan, *Animal models of pulmonary fibrosis.* Methods Mol Med, 2005. **117**: p. 251-9.
69. Kaminski, N., et al., *Global analysis of gene expression in pulmonary fibrosis reveals distinct programs regulating lung inflammation and fibrosis.* Proc Natl Acad Sci U S A, 2000. **97**(4): p. 1778-83.
70. Chua, F., J. Gauldie, and G.J. Laurent, *Pulmonary fibrosis: searching for model answers.* Am J Respir Cell Mol Biol, 2005. **33**(1): p. 9-13.
71. Kolb, M., et al., *Transient transgene expression of decorin in the lung reduces the fibrotic response to bleomycin.* Am J Respir Crit Care Med, 2001. **163**(3 Pt 1): p. 770-7.
72. Konigshoff, M., et al., *Functional Wnt signaling is increased in idiopathic pulmonary fibrosis.* PLoS One, 2008. **3**(5): p. e2142.
73. Vuga, L.J., et al., *WNT5A is a regulator of fibroblast proliferation and resistance to apoptosis.* Am J Respir Cell Mol Biol, 2009. **41**(5): p. 583-9.
74. Chilosi, M., et al., *Aberrant Wnt/beta-catenin pathway activation in idiopathic pulmonary fibrosis.* Am J Pathol, 2003. **162**(5): p. 1495-502.

75. Selman, M. and A. Pardo, *Role of epithelial cells in idiopathic pulmonary fibrosis: from innocent targets to serial killers.* Proc Am Thorac Soc, 2006. **3**(4): p. 364-72.
76. Thiery, J.P., et al., *Epithelial-mesenchymal transitions in development and disease.* Cell, 2009. **139**(5): p. 871-90.
77. Willis, B.C. and Z. Borok, *TGF-beta-induced EMT: mechanisms and implications for fibrotic lung disease.* Am J Physiol Lung Cell Mol Physiol, 2007. **293**(3): p. L525-34.
78. Pozharskaya, V., et al., *Twist: a regulator of epithelial-mesenchymal transition in lung fibrosis.* PLoS One, 2009. **4**(10): p. e7559.
79. Jayachandran, A., et al., *SNAI transcription factors mediate epithelial-mesenchymal transition in lung fibrosis.* Thorax, 2009. **64**(12): p. 1053-61.
80. Stewart, G.A., et al., *Expression of the developmental Sonic hedgehog (Shh) signalling pathway is up-regulated in chronic lung fibrosis and the Shh receptor patched 1 is present in circulating T lymphocytes.* J Pathol, 2003. **199**(4): p. 488-95.
81. Keniry, M. and R. Parsons, *The role of PTEN signaling perturbations in cancer and in targeted therapy.* Oncogene, 2008. **27**(41): p. 5477-85.
82. White, E.S., et al., *Negative regulation of myofibroblast differentiation by PTEN (Phosphatase and Tensin Homolog Deleted on chromosome 10).* Am J Respir Crit Care Med, 2006. **173**(1): p. 112-21.
83. Sternberg, N. and D. Hamilton, *Bacteriophage P1 site-specific recombination. I. Recombination between loxP sites.* J Mol Biol, 1981. **150**(4): p. 467-86.
84. Sternberg, N., D. Hamilton, and R. Hoess, *Bacteriophage P1 site-specific recombination. II. Recombination between loxP and the bacterial chromosome.* J Mol Biol, 1981. **150**(4): p. 487-507.
85. Sternberg, N., *Bacteriophage P1 site-specific recombination. III. Strand exchange during recombination at lox sites.* J Mol Biol, 1981. **150**(4): p. 603-8.
86. Tovar, K. and W. Hillen, *Tet Repressor Binding Induced Curvature of Tet Operator DNA.* Nucleic Acids Research, 1989. **17**(16): p. 6515-6522.
87. Sigler, A., et al., *Permeation of tetracyclines through membranes of liposomes and Escherichia coli.* Eur J Biochem, 2000. **267**(2): p. 527-34.
88. Triezenberg, S.J., R.C. Kingsbury, and S.L. McKnight, *Functional dissection of VP16, the trans-activator of herpes simplex virus immediate early gene expression.* Genes Dev, 1988. **2**(6): p. 718-29.
89. Takahashi, M., L. Altschmied, and W. Hillen, *Kinetic and equilibrium characterization of the Tet repressor-tetracycline complex by fluorescence measurements. Evidence for divalent metal ion requirement and energy transfer.* J Mol Biol, 1986. **187**(3): p. 341-8.
90. Gossen, M., et al., *Transcriptional activation by tetracyclines in mammalian cells.* Science, 1995. **268**(5218): p. 1766-9.
91. Schlake, T. and J. Bode, *Use of mutated FLP recognition target (FRT) sites for the exchange of expression cassettes at defined chromosomal loci.* Biochemistry, 1994. **33**(43): p. 12746-51.
92. Friedrich, G. and P. Soriano, *Promoter traps in embryonic stem cells: a genetic screen to identify and mutate developmental genes in mice.* Genes Dev, 1991. **5**(9): p. 1513-23.

93. Perl, A.K., et al., *Conditional recombination reveals distinct subsets of epithelial cells in trachea, bronchi, and alveoli.* Am J Respir Cell Mol Biol, 2005. **33**(5): p. 455-62.
94. Rhyu, M.S., L.Y. Jan, and Y.N. Jan, *Asymmetric distribution of numb protein during division of the sensory organ precursor cell confers distinct fates to daughter cells.* Cell, 1994. **76**(3): p. 477-91.
95. Knoblich, J.A., L.Y. Jan, and Y.N. Jan, *Asymmetric segregation of Numb and Prospero during cell division.* Nature, 1995. **377**(6550): p. 624-7.
96. Frise, E., et al., *The Drosophila Numb protein inhibits signaling of the Notch receptor during cell-cell interaction in sensory organ lineage.* Proc Natl Acad Sci U S A, 1996. **93**(21): p. 11925-32.
97. Zhong, W., et al., *Asymmetric localization of a mammalian numb homolog during mouse cortical neurogenesis.* Neuron, 1996. **17**(1): p. 43-53.
98. Zhong, W., et al., *Differential expression of mammalian Numb, Numblike and Notch1 suggests distinct roles during mouse cortical neurogenesis.* Development, 1997. **124**(10): p. 1887-97.
99. Dho, S.E., et al., *Characterization of four mammalian numb protein isoforms. Identification of cytoplasmic and membrane-associated variants of the phosphotyrosine binding domain.* J Biol Chem, 1999. **274**(46): p. 33097-104.
100. Verdi, J.M., et al., *Distinct human NUMB isoforms regulate differentiation vs. proliferation in the neuronal lineage.* Proc Natl Acad Sci U S A, 1999. **96**(18): p. 10472-6.
101. Salcini, A.E., et al., *Binding specificity and in vivo targets of the EH domain, a novel protein-protein interaction module.* Genes Dev, 1997. **11**(17): p. 2239-49.
102. Santolini, E., et al., *Numb is an endocytic protein.* J Cell Biol, 2000. **151**(6): p. 1345-52.
103. Diederich, R.J., et al., *Cytosolic interaction between deltex and Notch ankyrin repeats implicates deltex in the Notch signaling pathway.* Development, 1994. **120**(3): p. 473-81.
104. Kopan, R. and M.X. Ilagan, *The canonical Notch signaling pathway: unfolding the activation mechanism.* Cell, 2009. **137**(2): p. 216-33.
105. Ruiz i Altaba, A., *Gli proteins encode context-dependent positive and negative functions: implications for development and disease.* Development, 1999. **126**(14): p. 3205-16.
106. Di Marcotullio, L., et al., *Numb is a suppressor of Hedgehog signalling and targets Gli1 for Itch-dependent ubiquitination.* Nat Cell Biol, 2006. **8**(12): p. 1415-23.
107. Nie, J., et al., *LNX functions as a RING type E3 ubiquitin ligase that targets the cell fate determinant Numb for ubiquitin-dependent degradation.* EMBO J, 2002. **21**(1-2): p. 93-102.
108. Susini, L., et al., *Siah-1 binds and regulates the function of Numb.* Proc Natl Acad Sci U S A, 2001. **98**(26): p. 15067-72.
109. Colaluca, I.N., et al., *NUMB controls p53 tumour suppressor activity.* Nature, 2008. **451**(7174): p. 76-80.
110. Nishimura, T. and K. Kaibuchi, *Numb controls integrin endocytosis for directional cell migration with aPKC and PAR-3.* Dev Cell, 2007. **13**(1): p. 15-28.

111. Rasin, M.R., et al., *Numb and Numbl are required for maintenance of cadherin-based adhesion and polarity of neural progenitors.* Nat Neurosci, 2007. **10**(7): p. 819-27.
112. Wu, M., et al., *Epicardial spindle orientation controls cell entry into the myocardium.* Dev Cell, 2010. **19**(1): p. 114-25.
113. Liu, L., et al., *Numblike and Numb differentially affect p53 and Sonic Hedgehog signaling.* Biochem Biophys Res Commun, 2011. **413**(3): p. 426-31.
114. Vaira, V., et al., *Regulation of lung cancer metastasis by Klf4-Numb-like signaling.* Cancer Res, 2013. **73**(8): p. 2695-705.
115. Verdi, J.M., et al., *Mammalian NUMB is an evolutionarily conserved signaling adapter protein that specifies cell fate.* Curr Biol, 1996. **6**(9): p. 1134-45.
116. Bani-Yaghoub, M., et al., *A switch in numb isoforms is a critical step in cortical development.* Dev Dyn, 2007. **236**(3): p. 696-705.
117. Zhong, W., et al., *Mouse numb is an essential gene involved in cortical neurogenesis.* Proc Natl Acad Sci U S A, 2000. **97**(12): p. 6844-9.
118. Petersen, P.H., et al., *Progenitor cell maintenance requires numb and numblike during mouse neurogenesis.* Nature, 2002. **419**(6910): p. 929-34.
119. Petersen, P.H., et al., *Continuing role for mouse Numb and Numbl in maintaining progenitor cells during cortical neurogenesis.* Nat Neurosci, 2004. **7**(8): p. 803-11.
120. Cayouette, M., et al., *Asymmetric segregation of Numb in retinal development and the influence of the pigmented epithelium.* J Neurosci, 2001. **21**(15): p. 5643-51.
121. El-Hashash, A.H. and D. Warburton, *Numb expression and asymmetric versus symmetric cell division in distal embryonic lung epithelium.* J Histochem Cytochem, 2012. **60**(9): p. 675-82.
122. El-Hashash, A.H., et al., *Eya1 controls cell polarity, spindle orientation, cell fate and Notch signaling in distal embryonic lung epithelium.* Development, 2011. **138**(7): p. 1395-407.
123. El-Hashash, A.H. and D. Warburton, *Cell polarity and spindle orientation in the distal epithelium of embryonic lung.* Dev Dyn, 2011. **240**(2): p. 441-5.
124. Siller, K.H. and C.Q. Doe, *Spindle orientation during asymmetric cell division.* Nat Cell Biol, 2009. **11**(4): p. 365-74.
125. Zheng, Z., et al., *LGN regulates mitotic spindle orientation during epithelial morphogenesis.* J Cell Biol, 2010. **189**(2): p. 275-88.
126. Pece, S., et al., *Loss of negative regulation by Numb over Notch is relevant to human breast carcinogenesis.* J Cell Biol, 2004. **167**(2): p. 215-21.
127. Westhoff, B., et al., *Alterations of the Notch pathway in lung cancer.* Proc Natl Acad Sci U S A, 2009. **106**(52): p. 22293-8.
128. Talora, C., et al., *Notch signaling and diseases: an evolutionary journey from a simple beginning to complex outcomes.* Biochim Biophys Acta, 2008. **1782**(9): p. 489-97.
129. Zilian, O., et al., *Multiple roles of mouse Numb in tuning developmental cell fates.* Curr Biol, 2001. **11**(7): p. 494-501.
130. Perl, A.K., J.W. Tichelaar, and J.A. Whitsett, *Conditional gene expression in the respiratory epithelium of the mouse.* Transgenic Res, 2002. **11**(1): p. 21-9.

131. Wert, S.E., et al., *Transcriptional elements from the human SP-C gene direct expression in the primordial respiratory epithelium of transgenic mice.* Dev Biol, 1993. **156**(2): p. 426-43.
132. Perl, A.K., et al., *Early restriction of peripheral and proximal cell lineages during formation of the lung.* Proc Natl Acad Sci U S A, 2002. **99**(16): p. 10482-7.
133. Driscoll, B., et al., *Isolation and characterization of distal lung progenitor cells.* Methods Mol Biol, 2012. **879**: p. 109-22.
134. Shevchenko, A., et al., *In-gel digestion for mass spectrometric characterization of proteins and proteomes.* Nat Protoc, 2006. **1**(6): p. 2856-60.
135. Rappsilber, J., Y. Ishihama, and M. Mann, *Stop and go extraction tips for matrix-assisted laser desorption/ionization, nanoelectrospray, and LC/MS sample pretreatment in proteomics.* Anal Chem, 2003. **75**(3): p. 663-70.
136. Vaughan, A.E., et al., *Lineage-negative progenitors mobilize to regenerate lung epithelium after major injury.* Nature, 2015. **517**(7536): p. 621-5.
137. Zhao, J., et al., *Smad3 deficiency attenuates bleomycin-induced pulmonary fibrosis in mice.* Am J Physiol Lung Cell Mol Physiol, 2002. **282**(3): p. L585-93.
138. Lovgren, A.K., et al., *COX-2-derived prostacyclin protects against bleomycin-induced pulmonary fibrosis.* Am J Physiol Lung Cell Mol Physiol, 2006. **291**(2): p. L144-56.
139. Tanaka, K., et al., *Effects of lecithinized superoxide dismutase and/or pirfenidone against bleomycin-induced pulmonary fibrosis.* Chest, 2012. **142**(4): p. 1011-9.
140. Gumbiner, B.M., *Regulation of cadherin-mediated adhesion in morphogenesis.* Nat Rev Mol Cell Biol, 2005. **6**(8): p. 622-34.
141. Bullions, L.C. and A.J. Levine, *The role of beta-catenin in cell adhesion, signal transduction, and cancer.* Curr Opin Oncol, 1998. **10**(1): p. 81-7.
142. Nelson, W.J. and R. Nusse, *Convergence of Wnt, beta-catenin, and cadherin pathways.* Science, 2004. **303**(5663): p. 1483-7.
143. Adamson, I.Y. and D.H. Bowden, *The pathogenesis of bleomycin-induced pulmonary fibrosis in mice.* Am J Pathol, 1974. **77**(2): p. 185-97.
144. Moeller, A., et al., *The bleomycin animal model: a useful tool to investigate treatment options for idiopathic pulmonary fibrosis?* Int J Biochem Cell Biol, 2008. **40**(3): p. 362-82.
145. Moore, B.B. and C.M. Hogaboam, *Murine models of pulmonary fibrosis.* Am J Physiol Lung Cell Mol Physiol, 2008. **294**(2): p. L152-60.
146. Pilewski, J.M., et al., *Insulin-like growth factor binding proteins 3 and 5 are overexpressed in idiopathic pulmonary fibrosis and contribute to extracellular matrix deposition.* Am J Pathol, 2005. **166**(2): p. 399-407.
147. Hoyt, D.G. and J.S. Lazo, *Early increases in pulmonary mRNA encoding procollagens and transforming growth factor-beta in mice sensitive to cyclophosphamide-induced pulmonary fibrosis.* J Pharmacol Exp Ther, 1989. **249**(1): p. 38-43.
148. Fredberg, J.J. and D. Stamenovic, *On the Imperfect Elasticity of Lung-Tissue.* Journal of Applied Physiology, 1989. **67**(6): p. 2408-2419.
149. Hantos, Z., et al., *Input Impedance and Peripheral Inhomogeneity of Dog Lungs.* Journal of Applied Physiology, 1992. **72**(1): p. 168-178.

150. Sansores, R.H., et al., *Correlation between pulmonary fibrosis and the lung pressure-volume curve.* Lung, 1996. **174**(5): p. 315-323.
151. Pullamsetti, S.S., et al., *The Role of Dimethylarginine Dimethylaminohydrolase in Idiopathic Pulmonary Fibrosis.* Science Translational Medicine, 2011. **3**(87).
152. Arakawa, H. and K. Honma, *Honeycomb Lung: History and Current Concepts.* American Journal of Roentgenology, 2011. **196**(4): p. 773-782.
153. Altintas, N., et al., *Protective Effect of Infliximab, a Tumor Necrosis Factor-Alfa Inhibitor, on Bleomycin-Induced Lung Fibrosis in Rats.* Inflammation, 2016. **39**(1): p. 65-78.
154. Pardo, A., et al., *Role of matrix metalloproteinases in the pathogenesis of idiopathic pulmonary fibrosis.* Respir Res, 2016. **17**: p. 23.
155. De Langhe, S.P., et al., *Dickkopf-1 (DKK1) reveals that fibronectin is a major target of Wnt signaling in branching morphogenesis of the mouse embryonic lung.* Dev Biol, 2005. **277**(2): p. 316-31.
156. Jho, E.H., et al., *Wnt/beta-catenin/Tcf signaling induces the transcription of Axin2, a negative regulator of the signaling pathway.* Mol Cell Biol, 2002. **22**(4): p. 1172-83.
157. Cadigan, K.M. and M. Peifer, *Wnt signaling from development to disease: insights from model systems.* Cold Spring Harb Perspect Biol, 2009. **1**(2): p. a002881.
158. Doble, B.W., et al., *Functional redundancy of GSK-3alpha and GSK-3beta in Wnt/beta-catenin signaling shown by using an allelic series of embryonic stem cell lines.* Dev Cell, 2007. **12**(6): p. 957-71.
159. Klein, P.S. and D.A. Melton, *A molecular mechanism for the effect of lithium on development.* Proc Natl Acad Sci U S A, 1996. **93**(16): p. 8455-9.
160. Coghlan, M.P., et al., *Selective small molecule inhibitors of glycogen synthase kinase-3 modulate glycogen metabolism and gene transcription.* Chem Biol, 2000. **7**(10): p. 793-803.
161. Rock, K.L., et al., *Inhibitors of the proteasome block the degradation of most cell proteins and the generation of peptides presented on MHC class I molecules.* Cell, 1994. **78**(5): p. 761-71.
162. Li, Z.W., et al., *[MG-132 enhances MSCs survival and IL-10 secretion under hypoxia and serum deprivation condition].* Sheng Li Xue Bao, 2011. **63**(6): p. 525-32.
163. Gulino, A., L. Di Marcotullio, and I. Screpanti, *The multiple functions of Numb.* Exp Cell Res, 2010. **316**(6): p. 900-6.
164. Sorensen, E.B. and S.D. Conner, *AAK1 regulates Numb function at an early step in clathrin-mediated endocytosis.* Traffic, 2008. **9**(10): p. 1791-800.
165. Tokumitsu, H., et al., *Phosphorylation of Numb regulates its interaction with the clathrin-associated adaptor AP-2.* FEBS Lett, 2006. **580**(24): p. 5797-801.
166. Di Marcotullio, L., et al., *Numb activates the E3 ligase Itch to control Gli1 function through a novel degradation signal.* Oncogene, 2011. **30**(1): p. 65-76.
167. Beres, B.J., et al., *Numb regulates Notch1, but not Notch3, during myogenesis.* Mech Dev, 2011. **128**(5-6): p. 247-57.
168. Hein, M.Y., et al., *A human interactome in three quantitative dimensions organized by stoichiometries and abundances.* Cell, 2015. **163**(3): p. 712-23.
169. Hubner, N.C. and M. Mann, *Extracting gene function from protein-protein interactions using Quantitative BAC InteraCtomics (QUBIC).* Methods, 2011. **53**(4): p. 453-9.

170. Eden, E., et al., *GOrilla: a tool for discovery and visualization of enriched GO terms in ranked gene lists.* BMC Bioinformatics, 2009. **10**: p. 48.
171. Eden, E., et al., *Discovering motifs in ranked lists of DNA sequences.* PLoS Comput Biol, 2007. **3**(3): p. e39.
172. Sroka, R., et al., *Cortactin is a scaffolding platform for the E-cadherin adhesion complex and is regulated by protein kinase D1 phosphorylation.* J Cell Sci, 2016. **129**(12): p. 2416-29.
173. Lickert, H., et al., *Casein kinase II phosphorylation of E-cadherin increases E-cadherin/beta-catenin interaction and strengthens cell-cell adhesion.* J Biol Chem, 2000. **275**(7): p. 5090-5.
174. Bek, S. and R. Kemler, *Protein kinase CKII regulates the interaction of beta-catenin with alpha-catenin and its protein stability.* J Cell Sci, 2002. **115**(Pt 24): p. 4743-53.
175. Zhang, X., et al., *HDAC6 modulates cell motility by altering the acetylation level of cortactin.* Mol Cell, 2007. **27**(2): p. 197-213.
176. Watabe, M. and T. Nakaki, *Protein kinase CK2 regulates the formation and clearance of aggresomes in response to stress.* J Cell Sci, 2011. **124**(Pt 9): p. 1519-32.
177. Deshiere, A., et al., *Unbalanced expression of CK2 kinase subunits is sufficient to drive epithelial-to-mesenchymal transition by Snail1 induction.* Oncogene, 2013. **32**(11): p. 1373-83.
178. Helwani, F.M., et al., *Cortactin is necessary for E-cadherin-mediated contact formation and actin reorganization.* J Cell Biol, 2004. **164**(6): p. 899-910.
179. Weed, S.A., et al., *Cortactin localization to sites of actin assembly in lamellipodia requires interactions with F-actin and the Arp2/3 complex.* J Cell Biol, 2000. **151**(1): p. 29-40.
180. Higgs, H.N., *Actin nucleation: cortactin caught in the act.* Curr Biol, 2002. **12**(17): p. R593-5.
181. Kuo, C.T., et al., *Postnatal deletion of Numb/Numblike reveals repair and remodeling capacity in the subventricular neurogenic niche.* Cell, 2006. **127**(6): p. 1253-64.
182. Shen, Q., et al., *Asymmetric Numb distribution is critical for asymmetric cell division of mouse cerebral cortical stem cells and neuroblasts.* Development, 2002. **129**(20): p. 4843-53.
183. Shenje, L.T., et al., *Precardiac deletion of Numb and Numblike reveals renewal of cardiac progenitors.* Elife, 2014. **3**: p. e02164.
184. Spana, E.P. and C.Q. Doe, *Numb antagonizes Notch signaling to specify sibling neuron cell fates.* Neuron, 1996. **17**(1): p. 21-6.
185. Guo, M., L.Y. Jan, and Y.N. Jan, *Control of daughter cell fates during asymmetric division: interaction of Numb and Notch.* Neuron, 1996. **17**(1): p. 27-41.
186. Petersen, P.H., et al., *The enigma of the numb-Notch relationship during mammalian embryogenesis.* Dev Neurosci, 2006. **28**(1-2): p. 156-68.
187. Hirai, M., et al., *Adaptor proteins NUMB and NUMBL promote cell cycle withdrawal by targeting ERBB2 for degradation.* J Clin Invest, 2017. **127**(2): p. 569-582.
188. Sisson, T.H., et al., *Targeted injury of type II alveolar epithelial cells induces pulmonary fibrosis.* Am J Respir Crit Care Med, 2010. **181**(3): p. 254-63.

189. Miyake, Y., et al., *Protective role of macrophages in noninflammatory lung injury caused by selective ablation of alveolar epithelial type II Cells.* J Immunol, 2007. **178**(8): p. 5001-9.
190. Kim, K.K., et al., *Epithelial cell alpha3beta1 integrin links beta-catenin and Smad signaling to promote myofibroblast formation and pulmonary fibrosis.* J Clin Invest, 2009. **119**(1): p. 213-24.
191. Barkauskas, C.E., et al., *Type 2 alveolar cells are stem cells in adult lung.* J Clin Invest, 2013. **123**(7): p. 3025-36.
192. Knoblich, J.A., *Asymmetric cell division during animal development.* Nat Rev Mol Cell Biol, 2001. **2**(1): p. 11-20.
193. Knoblich, J.A., *Asymmetric cell division: recent developments and their implications for tumour biology.* Nat Rev Mol Cell Biol, 2010. **11**(12): p. 849-60.
194. Warburton, D., et al., *Stem/progenitor cells in lung development, injury repair, and regeneration.* Proc Am Thorac Soc, 2008. **5**(6): p. 703-6.
195. Warburton, D., et al., *The molecular basis of lung morphogenesis.* Mech Dev, 2000. **92**(1): p. 55-81.
196. Shi, W., J. Xu, and D. Warburton, *Development, repair and fibrosis: what is common and why it matters.* Respirology, 2009. **14**(5): p. 656-65.
197. Wang, Z. and S.S. Li, *Numb: A new player in EMT.* Cell Adh Migr, 2010. **4**(2): p. 176-9.
198. Fujita, Y., et al., *Hakai, a c-Cbl-like protein, ubiquitinates and induces endocytosis of the E-cadherin complex.* Nat Cell Biol, 2002. **4**(3): p. 222-31.
199. Palovuori, R., R. Sormunen, and S. Eskelinen, *SRC-induced disintegration of adherens junctions of madin-darby canine kidney cells is dependent on endocytosis of cadherin and antagonized by Tiam-1.* Lab Invest, 2003. **83**(12): p. 1901-15.
200. Shibamoto, S., et al., *Tyrosine phosphorylation of beta-catenin and plakoglobin enhanced by hepatocyte growth factor and epidermal growth factor in human carcinoma cells.* Cell Adhes Commun, 1994. **1**(4): p. 295-305.
201. Takeichi, M., et al., *Cadherin-dependent organization and disorganization of epithelial architecture.* Princess Takamatsu Symp, 1994. **24**: p. 28-37.
202. Provost, E. and D.L. Rimm, *Controversies at the cytoplasmic face of the cadherin-based adhesion complex.* Curr Opin Cell Biol, 1999. **11**(5): p. 567-72.
203. Sato, K., et al., *Numb controls E-cadherin endocytosis through p120 catenin with aPKC.* Mol Biol Cell, 2011. **22**(17): p. 3103-19.
204. Yost, C., et al., *The axis-inducing activity, stability, and subcellular distribution of beta-catenin is regulated in Xenopus embryos by glycogen synthase kinase 3.* Genes Dev, 1996. **10**(12): p. 1443-54.
205. Staal, F.J., et al., *Wnt signals are transmitted through N-terminally dephosphorylated beta-catenin.* EMBO Rep, 2002. **3**(1): p. 63-8.
206. De Langhe, S.P., et al., *Formation and differentiation of multiple mesenchymal lineages during lung development is regulated by beta-catenin signaling.* PLoS One, 2008. **3**(1): p. e1516.
207. Hirsch, C., et al., *Canonical Wnt signaling transiently stimulates proliferation and enhances neurogenesis in neonatal neural progenitor cultures.* Exp Cell Res, 2007. **313**(3): p. 572-87.

208. Rulifson, I.C., et al., *Wnt signaling regulates pancreatic beta cell proliferation.* Proc Natl Acad Sci U S A, 2007. **104**(15): p. 6247-52.
209. Rodda, S.J. and A.P. McMahon, *Distinct roles for Hedgehog and canonical Wnt signaling in specification, differentiation and maintenance of osteoblast progenitors.* Development, 2006. **133**(16): p. 3231-44.
210. Konigshoff, M. and O. Eickelberg, *WNT signaling in lung disease: a failure or a regeneration signal?* Am J Respir Cell Mol Biol, 2010. **42**(1): p. 21-31.
211. Henderson, W.R., Jr., et al., *Inhibition of Wnt/beta-catenin/CREB binding protein (CBP) signaling reverses pulmonary fibrosis.* Proc Natl Acad Sci U S A, 2010. **107**(32): p. 14309-14.
212. Itoh, M., et al., *Involvement of ZO-1 in cadherin-based cell adhesion through its direct binding to alpha catenin and actin filaments.* J Cell Biol, 1997. **138**(1): p. 181-92.
213. Gumbiner, B. and K. Simons, *A functional assay for proteins involved in establishing an epithelial occluding barrier: identification of a uvomorulin-like polypeptide.* J Cell Biol, 1986. **102**(2): p. 457-68.
214. Gumbiner, B., B. Stevenson, and A. Grimaldi, *The role of the cell adhesion molecule uvomorulin in the formation and maintenance of the epithelial junctional complex.* J Cell Biol, 1988. **107**(4): p. 1575-87.
215. Siliciano, J.D. and D.A. Goodenough, *Localization of the tight junction protein, ZO-1, is modulated by extracellular calcium and cell-cell contact in Madin-Darby canine kidney epithelial cells.* J Cell Biol, 1988. **107**(6 Pt 1): p. 2389-99.
216. Ando-Akatsuka, Y., et al., *Differential behavior of E-cadherin and occludin in their colocalization with ZO-1 during the establishment of epithelial cell polarity.* J Cell Physiol, 1999. **179**(2): p. 115-25.
217. Herold, S., N.M. Gabrielli, and I. Vadasz, *Novel concepts of acute lung injury and alveolar-capillary barrier dysfunction.* Am J Physiol Lung Cell Mol Physiol, 2013. **305**(10): p. L665-81.
218. Short, K.R., et al., *Pathogenesis of influenza-induced acute respiratory distress syndrome.* Lancet Infect Dis, 2014. **14**(1): p. 57-69.
219. Herold, S., et al., *Lung epithelial apoptosis in influenza virus pneumonia: the role of macrophage-expressed TNF-related apoptosis-inducing ligand.* J Exp Med, 2008. **205**(13): p. 3065-77.
220. Lee, C.G., et al., *Early growth response gene 1-mediated apoptosis is essential for transforming growth factor beta1-induced pulmonary fibrosis.* J Exp Med, 2004. **200**(3): p. 377-89.
221. Lee, C.G., et al., *Transgenic modeling of transforming growth factor-beta(1): role of apoptosis in fibrosis and alveolar remodeling.* Proc Am Thorac Soc, 2006. **3**(5): p. 418-23.
222. Adamson, I.Y., L. Young, and D.H. Bowden, *Relationship of alveolar epithelial injury and repair to the induction of pulmonary fibrosis.* Am J Pathol, 1988. **130**(2): p. 377-83.
223. Fukuda, Y., et al., *Patterns of pulmonary structural remodeling after experimental paraquat toxicity. The morphogenesis of intraalveolar fibrosis.* Am J Pathol, 1985. **118**(3): p. 452-75.
224. Parks, W.C. and S.D. Shapiro, *Matrix metalloproteinases in lung biology.* Respir Res, 2001. **2**(1): p. 10-9.

225. Kuhn, C., 3rd, et al., *An immunohistochemical study of architectural remodeling and connective tissue synthesis in pulmonary fibrosis.* Am Rev Respir Dis, 1989. **140**(6): p. 1693-703.
226. Zhang, K., et al., *Myofibroblasts and their role in lung collagen gene expression during pulmonary fibrosis. A combined immunohistochemical and in situ hybridization study.* Am J Pathol, 1994. **145**(1): p. 114-25.
227. Yue, X., B. Shan, and J.A. Lasky, *TGF-beta: Titan of Lung Fibrogenesis.* Curr Enzym Inhib, 2010. **6**(2).
228. Lasky, J.A., et al., *Connective tissue growth factor mRNA expression is upregulated in bleomycin-induced lung fibrosis.* Am J Physiol, 1998. **275**(2 Pt 1): p. L365-71.
229. Spanjer, A.I., et al., *TGF-beta-induced profibrotic signaling is regulated in part by the WNT receptor Frizzled-8.* FASEB J, 2016. **30**(5): p. 1823-35.
230. Akhmetshina, A., et al., *Activation of canonical Wnt signalling is required for TGF-beta-mediated fibrosis.* Nat Commun, 2012. **3**: p. 735.
231. Chen, C.C. and L.F. Lau, *Functions and mechanisms of action of CCN matricellular proteins.* Int J Biochem Cell Biol, 2009. **41**(4): p. 771-83.
232. van Noort, M., et al., *Wnt signaling controls the phosphorylation status of beta-catenin.* J Biol Chem, 2002. **277**(20): p. 17901-5.
233. Katsube, T., et al., *Cortactin associates with the cell-cell junction protein ZO-1 in both Drosophila and mouse.* J Biol Chem, 1998. **273**(45): p. 29672-7.
234. Mizutani, K., et al., *Essential role of neural Wiskott-Aldrich syndrome protein in podosome formation and degradation of extracellular matrix in src-transformed fibroblasts.* Cancer Res, 2002. **62**(3): p. 669-74.
235. Bowden, E.T., et al., *Co-localization of cortactin and phosphotyrosine identifies active invadopodia in human breast cancer cells.* Exp Cell Res, 2006. **312**(8): p. 1240-53.
236. McNiven, M.A., et al., *Regulated interactions between dynamin and the actin-binding protein cortactin modulate cell shape.* J Cell Biol, 2000. **151**(1): p. 187-98.
237. Kaksonen, M., H.B. Peng, and H. Rauvala, *Association of cortactin with dynamic actin in lamellipodia and on endosomal vesicles.* J Cell Sci, 2000. **113 Pt 24**: p. 4421-6.
238. Wu, H. and J.T. Parsons, *Cortactin, an 80/85-kilodalton pp60src substrate, is a filamentous actin-binding protein enriched in the cell cortex.* J Cell Biol, 1993. **120**(6): p. 1417-26.
239. Aguado, R., et al., *The endocytic adaptor Numb regulates thymus size by modulating pre-TCR signaling during asymmetric division.* Blood, 2010. **116**(10): p. 1705-14.
240. Tian, Y., et al., *IQGAP1 regulates endothelial barrier function via EB1-cortactin cross talk.* Mol Cell Biol, 2014. **34**(18): p. 3546-58.
241. Aumiller, V., et al., *WNT/beta-catenin signaling induces IL-1beta expression by alveolar epithelial cells in pulmonary fibrosis.* Am J Respir Cell Mol Biol, 2013. **49**(1): p. 96-104.
242. Klee, S., et al., *WISP1 mediates IL-6-dependent proliferation in primary human lung fibroblasts.* Sci Rep, 2016. **6**: p. 20547.

MICHAEL HOFMANN

Research Scientist (Dipl.-Biol.), PhD Candidate

CV

CONTACT

Phone:
(+49)17624018126

Email:
m.hof202@gmail.com

Home:
Frankfurter Str. 115a
61231 Bad Nauheim
Germany (Hesse)

http://linkedin.com/in/
michael-hofmann-441ba2135

Michael Hofmann
m.hof202@gmail.com

WORK EXPERIENCE

Research Scientist (Dipl.-Biol.), PhD Candidate 11/2009 - Present
Max Planck Institute for Heart and Lung Research
Ludwigstr. 43 - 61231 Bad Nauheim - Germany (Hesse)

Project:
"Lung epithelial specific depletion of Numb and Numblike impairs epithelial polarity and integrity"

Diploma Thesis (Dipl.-Biol.) 02/2009 - 10/2009
Max Planck Institute for Heart and Lung Research
Ludwigstr. 43 - 61231 Bad Nauheim - Germany (Hesse)

Project:
''Identification and characterization of the DEAD-box RNA-helicase DDX41'' - Grade: 1,0

EDUCATION

International Max Planck Research School for Heart and Lung Research (graduate program) 10/2009 - 10/2012
Max Planck Institute for Heart and Lung Research
Ludwigstr. 43 - 61231 Bad Nauheim - Germany (Hesse)

Diploma of Bioscience (Dipl.-Biol.) 10/2003 - 10/2009
Technical University of Darmstadt (TUD)
64289 Darmstadt - Germany (Hesse)

Graduated in (Grade): Final grade: Sehr gut
Cell and Developmental Biology (1,0), Zoology and Animal Physiology (1,3), Biochemistry (2,0)